Chulalongkorn University

Chula Digital Collections

Chulalongkorn University Theses and Dissertations (Chula ETD)

2019

Wind load analysis of a high-rise building by computational fluid dynamics

Canh Thiet Phung
Faculty of Engineering

Follow this and additional works at: https://digital.car.chula.ac.th/chulaetd

Part of the Civil Engineering Commons, and the Construction Engineering and Management Commons

Wind Load Analysis of a High-rise Building by Computational Fluid Dynamics

Mr. Canh Thiet Phung

จุฬาลงกรณ์มหาวิทยาลัย
CHULALONGKORN UNIVERSITY

A Thesis Submitted in Partial Fulfillment of the Requirements

for the Degree of Master of Engineering in Civil Engineering

Department of Civil Engineering

FACULTY OF ENGINEERING

Chulalongkorn University

Academic Year 2019

การวิเคราะห์แรงลมที่กระทำต่ออาคารสูงด้วยวิธีพลศาสตร์ของไหลเชิงคำนวณ

นายแคน เทียต ฟุง

วิทยานิพนธ์นี้เป็นส่วนหนึ่งของการศึกษาตามหลักสูตรปริญญาวิศวกรรมศาสตรมหาบัณฑิต
สาขาวิชาวิศวกรรมโยธา ภาควิชาวิศวกรรมโยธา
คณะวิศวกรรมศาสตร์ จุฬาลงกรณ์มหาวิทยาลัย
ปีการศึกษา 2562
ลิขสิทธิ์ของจุฬาลงกรณ์มหาวิทยาลัย

Thesis Title	Wind Load Analysis of a High-rise Building by Computational Fluid Dynamics
By	Mr. Canh Thiet Phung
Field of Study	Civil Engineering
Thesis Advisor	Assistant Professor CHATPAN CHINTANAPAKDEE, Ph.D.

Accepted by the FACULTY OF ENGINEERING, Chulalongkorn University in Partial Fulfillment of the Requirement for the Master of Engineering

.... Dean of the FACULTY OF
ENGINEERING
(Professor SUPOT TEACHAVORASINSKUN, D.Eng.)

THESIS COMMITTEE

.... Chairman
(Associate Professor Anat Ruangrassamee, Ph.D.)

.... Thesis Advisor
(Assistant Professor CHATPAN CHINTANAPAKDEE, Ph.D.)

.... External Examiner
(Associate Professor Virote Boonyapinyo, Ph.D.)

แคน เทียต ฟุง : การวิเคราะห์แรงลมที่กระทำต่ออาคารสูงด้วยวิธีพลศาสตร์ของไหลเชิงคำนวณ. (Wind Load Analysis of a High-rise Building by Computational Fluid Dynamics) อ.ที่ปรึกษาหลัก : ผศ. ดร.ฉัตรพันธ์ จินตนาภักดี

อาคารสมัยใหม่ถูกสร้างให้สูงขึ้นเนื่องจากมีพื้นที่ในการสร้างที่จำกัด มักจะเป็นอาคารที่มีรูปทรงโครงสร้างไม่สม่ำเสมอและมีข้อจำกัดบางอย่าง การออกแบบจึงไม่สามารถใช้สมการแรงลมได้เนื่องจากเป็นอาคารซึ่งอยู่นอกเหนือขอบเขตที่ระบุไว้ในมาตรฐานการคำนวณแรงลม มีการแนะนำให้ใช้การทดสอบในอุโมงค์ลม (Wind tunnel test, WTT) เพื่อคำนวณแรงลมที่เหมาะสมสำหรับการออกแบบอาคารดังกล่าว อย่างไรก็ตามการทดสอบในอุโมงค์ลมนั้นมีค่าใช้จ่ายสูงและใช้เวลามากเนื่องจากต้องเตรียมแบบจำลองอาคารขนาดเล็กโดยย่อส่วนจากอาคารเป้าหมายที่ได้รับการพิจารณาด้วยเครื่องมือวัดและแบบจำลองบล็อกที่รูปร่างเหมือนจริงจำนวนมากของสิ่งปลูกสร้างโดยรอบ (Surrounding buildings, SBs) การศึกษานี้เป็นการประเมินความถูกต้องของแรงลมในอาคารสูง 150 เมตร ตั้งอยู่ในจังหวัดกรุงเทพฯ โดยการเปรียบเทียบผลจากการคำนวณพลศาสตร์ของไหล (Computational fluid dynamics, CFD) กับการทดสอบในอุโมงค์ลมของอาคารเดียวกันที่มาตราส่วน 1: 400 และพื้นที่ใกล้เคียงในรัศมี 400 เมตร การคำนวณพลศาสตร์ของไหลนำมาใช้ในโปรแกรม ANSYS Fluent เพื่อให้ได้เงื่อนไขที่ใกล้เคียงที่สุดในการตั้งค่าการทดสอบในอุโมงค์ลม วิธีการคำนวณพลศาสตร์ของไหลที่มีประสิทธิภาพมากที่สุดมีสองวิธี (1) แบบจำลองความปั่นป่วนชนิด k-ω-SST (shear stress transport) และ (2) การจำลองลาร์จเอ็ดดี้ (Large-eddy simulation, LES) นำมาใช้ในการจำลองและประเมินหาวิธีที่มีประสิทธิภาพมากกว่า ผลการศึกษาพบว่าการจำลองลาร์จเอ็ดดี้ให้ความแม่นยำที่ดีขึ้นเล็กน้อย แต่แบบจำลองความปั่นป่วนชนิด k-ω-SST ยังคงให้ความแม่นยำที่ยอมรับได้เมื่อเทียบกับการทดสอบในอุโมงค์ลม อย่างไรก็ตามแบบจำลองความปั่นป่วนชนิด k-ω-SST ใช้เวลาในการคำนวณน้อยกว่าอีกวิธีมาก นอกจากนี้การเปรียบเทียบผลการคำนวณพลศาสตร์ของไหลกรณีมีและไม่มีสิ่งปลูกสร้างโดยรอบพบว่าสิ่งปลูกสร้างโดยรอบมีบทบาทสำคัญในการแปรเปลี่ยนของลมปั่นป่วนที่ความสูงระดับต่ำและมีอิทธิพลอย่างมากต่อหน่วยแรงลมในอาคารเป้าหมายท้ายที่สุด มีการสรุปการใช้งานสื่ออย่างเพื่อแสดงความสอดคล้องระหว่างการคำนวณพลศาสตร์ของไหลและมาตรฐานการคำนวณแรงลม

สาขาวิชา	วิศวกรรมโยธา	ลายมือชื่อนิสิต	....
ปีการศึกษา	2562	ลายมือชื่อ อ.ที่ปรึกษาหลัก	....

6170119321 : MAJOR CIVIL ENGINEERING

KEYWORD: Computational Fluid Dynamics (CFD); Wind loads; Tall buildings; Turbulence models; Large-eddy simulation (LES)

Canh Thiet Phung : Wind Load Analysis of a High-rise Building by Computational Fluid Dynamics . Advisor: Asst. Prof. CHATPAN CHINTANAPAKDEE, Ph.D.

As new buildings become taller due to limited land area, often irregular in shapes for esthetics and some design constraints, wind load formula provided in design codes/standards cannot be applied because of the limitations. Wind tunnel test (WTT) is thus the suggested approach to obtain appropriate wind load for the design of such buildings. However, WTT is costly and time-consuming as it often requires much preparation of the small-scale model of the target building, instrumentation, and numerous realistic blocks of surrounding buildings (SBs). In this study, the CFD's accuracy will be evaluated by comparing its results to WTT by a wind loads analysis of a 150m-tall irregular-shaped building in Bangkok with consideration of the influence of 400 m radius of the neighboring area. CFD was implemented in ANSYS Fluent for the conditions as close as possible to the WTT setup. Two most effective CFD approaches: (1) k-ω-SST (shear stress transport) turbulence model (TB) and (2) Large Eddy Simulation (LES) were used in the simulation as two alternatives and evaluated to identify the more promising method. Results showed that LES provides slightly better accuracy, but the k-ω-SST TB still provides reasonably acceptable accuracy compared to WTT. However, k-ω-SST TB requires significantly less computational time. Besides, the comparison of CFD results from the case without and with SBs reveals that SBs play an essential role in turbulence development at low elevation and significantly influence the target building's wind pressure. Finally, CFD's wind load analysis applications were summarized to show the connection between CFD and building codes/standards in the wind load evaluation.

Field of Study:	Civil Engineering	Student's Signature	
Academic Year:	2019	Advisor's Signature	

ACKNOWLEDGEMENTS

TABLE OF CONTENTS

จุฬาลงกรณ์มหาวิทยาลัย

CHULALONGKORN UNIVERSITY

LIST OF TABLES

LIST OF FIGURES

CHAPTER 1

INTRODUCTION

1.1 Background

Wind is a movement of air from a high-pressure area to a lower one, effecting directly on a building's cladding. Depending on where the structure is located, wind can be a threat or natural ventilation.

Wind analysis is an essential part of building design, especially for tall buildings. The taller the structure, the more significance of wind load acting on it. Moreover, wind loads significantly influence the building shape design and the size of constructional components (such as beams, columns, window glass, and thickness). Nowadays, understanding how wind flows affects a building helps us save a large portion of construction costs for modern architecture. Such as making wind flow become natural ventilation in green building design. Using the open windows on the structure and organizing walls with interiors to receive directly natural wind flow to cool down the room temperature without an artificial cooling system.

There are many tools for wind load analysis, which have been developed and improved for many decades. Building codes (or civil engineering standards) and Wind tunnel tests (WTTs) are well-known wind action measurement methods. WTTs have been applied a long time ago and proved themselves useful in most applications (such as aerospace, cars industry, and fluid dynamic). In civil engineering, they provide wind characteristics affecting the target building based on base forces, torque moments, surface pressure, pressure coefficients, and streamlines with high accuracy. However, the price of a WTT is not affordable for all types of constructions. In reality, most buildings tend to be designed by using wind loads from formulas in building codes or design standards. Although they are free, legal, and simple, those formulas cannot be applied to irregularly shaped or slender buildings. Some design engineers tried to apply those formulas anyhow, which might result in under-estimation of

wind load. Computational Fluid Dynamics (CFD) has been considered a promising tool due to many advantages to overcome the limitations of building codes and avoid costly wind tunnel tests.

Computational Fluid Dynamics (CFD) is a branch of fluid mechanics that uses numerical analysis and data structures to analyze and solve fluid flows problems. The CFD application in wind analysis on a building aims to predict the wind loads on this building, and wind flows around it if needed.

CFD's development in wind loads analysis became feasible thirty years ago with the rapid increase of computer performance and memory storage. However, in many years, computer resources had not allowed complicated calculations, and CFD has been restricted by Reynolds Averaged Navier-Stokes (RANS) approach. Recently, the transient simulation, which is the Large Eddy Simulation (LES), performed that CFD can reach an excellent accurate level and potentially compete with WTTs. There are several reasons why it would be consistent in developing furtherly this numerical tool. The first reason is that wind-tunnel studies are limited in the early stage of design: a significant change of design building shape cannot require an equal number of WTTs to verify which plan will be better. The second one is that WTTs are hard to provide a full-scale model test, and hence they will face scale effect, where CFD can offer the advantage of full-scale simulation. Finally, the CFD solution is not limited in output data provide: it can provide analytical data everywhere within the computational domain, where WTTs provide the data where the sensors placed.

Figure 1-1 Benefits of CFD simulation (www.simscale.com)

Various research of CFD applications on high-rise building has been studied recently such as Selvam (1997), Murakami and Mochida (1988), Wright and Easom (2003), Camarri et al. (2005), Tamura (2006), El-Okda et al. (2008), Tominaga et al. (2008), Dagnew et al. (2009) and Luo et al. (2019). Some of the highlights will be covered below to indicate the development of CFD in many decades.

Murakami (1998) has provided turbulence models' historical review to that time and mentioned the difficulties that limited the CFD's practical applicability during that period. Few of the challenges were:

(1) High turbulent flow (high Re number flow) simulation makes the accuracy of simulation depending on the grid resolution.

(2) Wind flow is complex and unsteady, affecting buildings with the three-dimension (3D) turbulent flow field, such as the generation and dissipation of vortexes (eddies). Those phenomena require 3D computation with an advanced simulation-approach such as LES. However, with the limitation in computational resources, 2D RANS simulations were mainly used in that period.

(3) Sharp edges at building corners bring difficultly to investigate the wind flow field.

(4) "Bluff body wake" effects to inflow and outflow boundaries in LES.

Based on these existing problems, several revisions have been made on RANS turbulence models. The alterations on RANS models, especially the modifications made on standard $k-\varepsilon$ models, successfully correct the overestimation of kinetic energy production at the impinging regions and reproduce flow separation and reattachment around building roofs (Murakami et al., 1999). The Shear Stress Transport $k-\omega$ model ($k-\omega-SST$) (Menter) is a well-known hybrid turbulence models in CFD, which connects two turbulence models' advantages ($k-\omega$ and $k-\varepsilon$). The use of $k-\omega$ turbulence model in low Reynolds (Re) number

turbulence is suitable without any extra damping functions. However, this $k-\omega$ model is sensitive to free-stream in the far-fields. Hence, the SST formulation switches to $k-\varepsilon$ model in those regions and thereby prevents the shortcomings of $k-\omega$ model.

Additionally, computational resources' evolution provides CFD with a new simulation approach, which is the Large Eddy Simulation (LES). LES is the mathematic model for turbulence flow, which is only second best to the Direct Numerical Simulation (DNS) regarding precision level. While DNS solves the Navier–Stokes (N-S) equations in an extensive range of time and length scales, LES principally ignores the smallest length scales (smaller than the minimum grid size). Those small eddies take the most computationally expensive to solve; hence they are filtered (by a filter function) and then modeled to reduce the total computational cost in LES (Dagnew and Bitsuamlak, 2013) (this will be discussed in detail in the next chapter). Thereby, LES is a promising tool for wind load evaluation (Tamura et al., 2008).

Some countries have already built working groups to research the CFD's practical applicability and have developed recommendations (or guidelines) for practical building design. The Architectural Institute of Japan (AIJ) developed a CFD application guideline on high-rise buildings (Tamura et al., 2008). Then, they published the first CFD guideline for structural purposes in 2015. They adopted CFD simulations for wind load investigation, provided that knowledgeable handling the software and critical examination to be performed by an experienced wind engineer (AIJ, 2017). This publication's language was Japanese, but luckily some researchers have presented it in a few articles by English.

Meanwhile, European Cooperation in Science and Technology (COST) published a practice guideline for CFD simulation of flows in an urban environment by steady-state RANS approaches (Jorg Franke et al., 2011). American Society of Civil Engineering (ASCE) contributed a task committee that aims to provide civil and

environmental engineers guidance on using computational fluid dynamics in handling fluid-related problems. However, it was still restricted in water and wastewater treatment fields.

Figure 1-2 AIJ guide book for numerical simulation of wind environment in urban areas (left); COST Action 732 (right)

CFD simulation has caught a trending because of the participation of many commercial CFD software. The well-known ANSYS Fluent and ANSYS CFX from ANSYS, Inc. have provided users many fluid mechanic applications, which were listed in ANSYS Fluent Tutorial Guide (published and updated by ANSYS, Inc. when releasing the new ANSYS Fluent version). Another popular CFD software from Autodesk, Inc. is AUTODESK CFD. OpenFOAM is a C++ toolbox for the development of customized numerical solvers, and post-processing utilities for the solution of continuum mechanics problems, including computational fluid dynamics. SIMSCALES is a computer-aided engineering software product based on cloud computing (overcoming the limitation of computer hardware), which was developed by SimScale GmbH and allowed the combination of Computational Fluid Dynamics, Finite Element Analysis and Thermal simulations. All the above showed that many commercial organizations had put their effort into creating, improving, and updating the CFD codes, which also provide users a friendly user interface.

Figure 1-3 Some of CFD software now on the market (www.resolvedanalytics.com)

Based on the background and history reviews, CFD has development prospects to be an excellent numerical method in wind loads analysis. However, the popularity is still limited in some countries. Therefore, it requires more studies to provide implementation guidelines, accuracy level, algorithms, investment costs, and practical cases; hence, this study would present one more wind analysis case on a high-rise building by CFD.

1.2 Objectives

To determine the applicability of CFD in wind loads analysis on a high-rise building, this study considers these objectives below:

(1) To evaluate CFD's accuracy and reliability in the prediction of pressure coefficient distribution on cladding surfaces of target building by comparisons with wind tunnel test data.

(2) To evaluate the influence of the surrounding buildings (SBs) on the target building in CFD simulations.

(3) To indicate the simulation time of different mathematical approaches in CFD simulations, hence recommending the suitable method in wind load analysis.

(4) To indicate a connection between CFD simulation and building codes in practical building design.

1.3 Scope of research

This research scope of this study is following

(1) CFD is applied to a 150 meters tall irregular-shaped building in Bangkok, Thailand. Additionally, 400 meters radius of surrounding buildings will be considered in the simulation of target building with surrounding buildings.

(2) This study would focus on two efficient methods: steady-state $k-\omega-SST$ models and transient LES in simulation.

(3) The software used to conduct the simulation was ANSYS Fluent from Ansys, Inc.

Also, these assumptions were made in this studying:

(1) The wind flow in this research is considered an impressible flow (the air density is constant (ρ = 1.2 kg/m^3), and the wind flow characteristics do not depend on the environment temperature. (*)

(2) The change of heat (heat transferring) in the domain was neglected.

(*) In reality, none of the flow is incompressible. The density of a specific flow always changes depending on environmental conditions such as temperature, pressure, and elevation. In fluid mechanics flows is usually considered as incompressible when the Mach number (the ratio of the speed of the flow to the speed of sound) is less than 0.3 (since the density change due to velocity is about 5% in that case) for computational resource reduction (Anderson and Wendt, 1995). At the Mach number of 0.3, the airflow speed is approximately 100m/s (speed of sound in the air is 343 m/s). In this study, the wind flow speed reaches the maximum at 10.984 m/s (at the domain inlet), and the simulating-generated speed in the whole computational domain is also less than 100 m/s. Thus, the wind flow is treated as an incompressible flow in this study.

Mach Number Flow Regimes

Incompressible Flow	Sub-Sonic Flow	Tran-Sonic Flow	Super-Sonic Flow	Hyper-Sonic Flow	Hyper-Velocity Flow
0.1	0.3	1	5	10	20
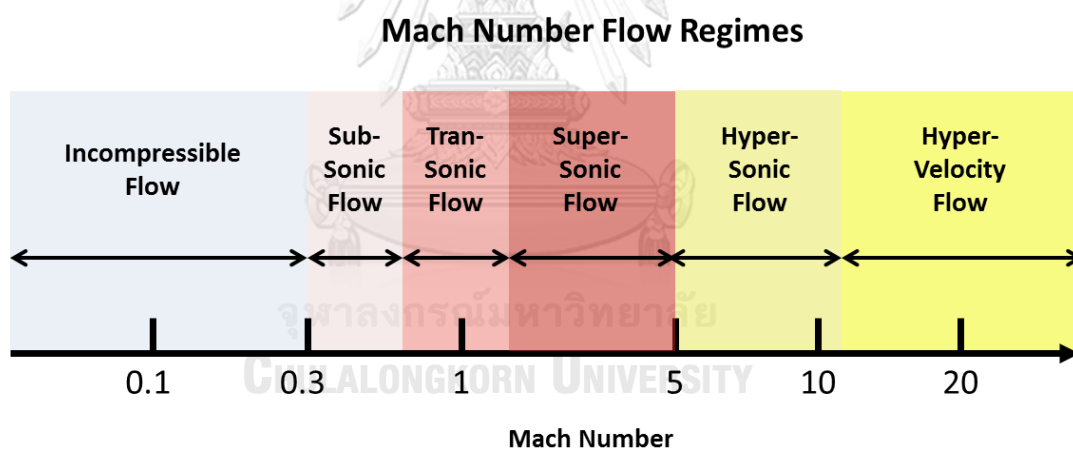
Mach Number

Figure 1-4 The relation of Mach number and flow regimes (Wikipedia)

1.4 Research methodology

The procedure adopted in this study is outlined as the followings:

(1) Review the mathematical model for computational fluid dynamics for airflow (Navier-Stokes equations) and the numerical technique for solving this governing equation - Finite Volume Method (FVM).

(2) Perform CFD simulation with incoming wind flow with the same condition as that in the wind tunnel test to simulate flow in the wind tunnel test.

(3) Compare the pressure coefficients of the target building from CFD simulation to the wind tunnel test's reference data.

(4) Add surrounding buildings in the CFD models to study the effects of surrounding buildings.

(5) Review the building standards/codes to indicate the connection with the wind load analysis by thereof. Moreover, provide the four applications, which CFD simulations can show their advantages.

1.5 Thesis outline

This thesis includes six parts which are briefly described below:

- Chapter 1 Introduction gives an overview of CFD in wind load analysis, objectives of the study, research scope, and provides the research schedule.

- Chapter 2 Literature reviews presents the derivation of the governing equations of the wind flow, introduces what the CFD and its methodology are. The turbulence models and LES will also be explained in this chapter.

- Chapter 3 Wind Tunnel Test description describes the WTT properties: the building geometry, wind flow characteristic, applying civil codes.

- Chapter 4 CFD simulation by ANSYS Fluent presents in detail of the simulation process.

- Chapter 5 Influences of surrounding buildings on wind loads of the primary structure.

- Chapter 6 Accuracy of CFD presents the results in the simulation comparing with WTT data.

- Chapter 7 Computation time provide information about simulation time and recommend the suitable approach method.

- Chapter 8 Connection to building codes review the building codes/standards and discuss the roles of CFD in wind load analysis.

- Chapter 9 Conclusions.

- Appendix A ANSYS Fluent validation cases describes two examples of CFD simulation to validate the software's accuracy.
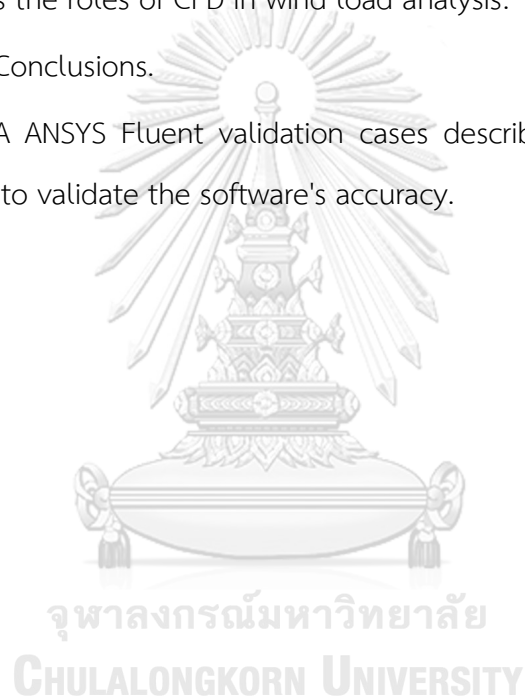
CHAPTER 2

LITERATURE REVIEWS

2.1 Introduction to Computational Fluid Dynamics

Computational Fluid Dynamics (CFD) is a computer-aided-engineering (CAE) field that simulates fluid motion and heat transfer by using numerical analysis and data structures. CFD is a process which starts from the applying the Navier-Stokes equations (governing equations) on any cell in the computational fluid domain (CD), to solve the whole set of those equations on over CD under the aid of computers, then process the variables to the expected results. This chapter will indicate the primary stages in the CFD process, which will apply to simulate the wind flow.

2.1.1 Governing equations of wind flow

The governing equations of fluid flow (Navier-Stoke equations) were based on physics and conservations laws, which are:

    (1) The conservation of mass.

    (2) The conservation of momentum.

    (3) The conservation of energy.

The conservation of energy in the airflow domain is defined that "the change rate of energy is equal to the total heat change rate, and the rate of work done on a fluid particle," which is also the first law of thermodynamics. In this study, the heat change in the airflow domain was neglected. In other words, the conservation of energy will be ignored. Thereby, the conservation of mass and the conservation of momentum will be presented in 2.1.1 to derivate the set of governing equations for wind flow.

Let us consider an infinitesimal cubic volume of fluid with dimension δx, δy and δz as shown in Figure 2-1.
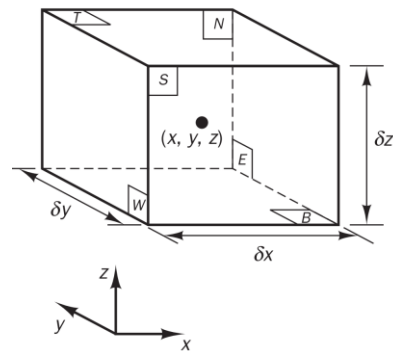
Figure 2-1 Infinitesimal fluid particle in the computational domain

Those labels: N, S, E, W, T, and B stand for North, South, East, West, Top, and Bottom, respectively. The positive directions along the coordinate axes. The element center is at coordinate *(x, y, z)*. We would consider the change of mass, the momentum of the fluid element due to fluid flow across its boundaries. Due to the action of sources inside this element, the governing equations would be generated.

Note that Taylor's series expansion would be used many times in the derivation process of governing equations. The element is considered extremely small; hence, there is only the first two-term of this series will be considered, while high-order terms of series (h.o.t) will be neglected to simplify the equations.

2.1.1.1 Conservation of mass

Consider one infinitesimal element in Figure 2-1, after a short time δt; this element size would change on the 3-dimensions directions from δx, δy, δz to $\delta x + \delta u \delta t$, $\delta y + \delta v \delta t$, $\delta z + \delta w \delta t$, respectively; where δu, δv, δw are expressed the small change of velocity in x, y, and z-direction.
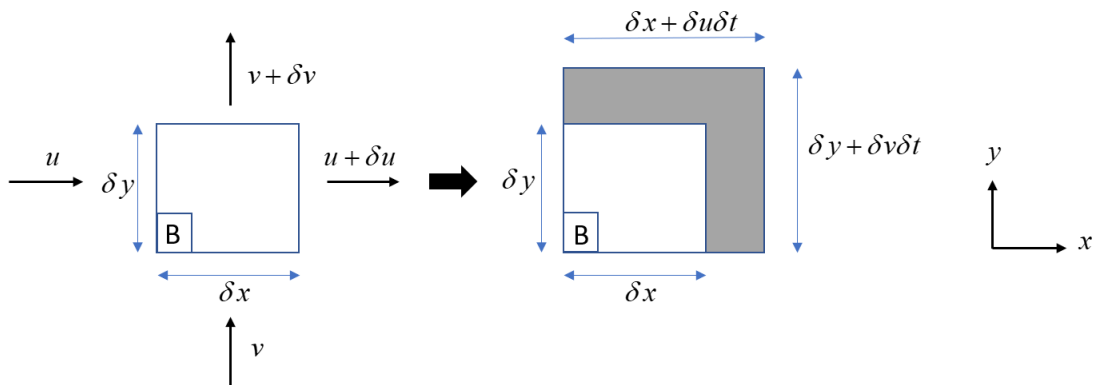
Figure 2-2 The change of velocity and size of infinitesimal elements after a short time δt

The velocity in the x-direction of this particle is $u + \delta u$ (Figure 2-2) at the time $t + \delta t$; Using the Taylor series expansion, we have $u + \delta u = u + \frac{\partial u}{\partial x}\delta x + h.o.t$ so that $\delta u = \frac{\partial u}{\partial x}\delta x$. For y-axis and z-axis, the same idea is applied, we obtain:

$$\delta u = \frac{\partial u}{\partial x}\delta x \tag{2-1}$$

$$\delta v = \frac{\partial v}{\partial y}\delta y \tag{2-2}$$

$$\delta w = \frac{\partial w}{\partial z}\delta z \tag{2-3}$$

The change of volume is

$$(\delta x + \delta u\delta t)(\delta y + \delta v\delta t)(\delta z + \delta w\delta t) - \delta x\delta y\delta z \tag{2-4}$$

Using the Taylor series expansion, we obtain:

$$\delta u\delta y\delta z\delta t + \delta v\delta x\delta z\delta t + \delta w\delta x\delta y\delta t + h.o.t =$$

$$= \frac{\partial u}{\partial x}\delta x\delta y\delta z\delta t + \frac{\partial v}{\partial y}\delta y\delta x\delta z\delta t + \frac{\partial w}{\partial z}\delta z\delta x\delta y\delta t \tag{2-5}$$

Besides, the wind flow is considered as incompressible fluid flow, so the volume change of the element in Figure 2-1 was nothing. In other words, the volume change will be equal to zero. From Eq. (2-6) we obtain:

$$\frac{\partial u}{\partial x}\delta x\delta y\delta z\delta t + \frac{\partial v}{\partial y}\delta y\delta x\delta z\delta t + \frac{\partial w}{\partial z}\delta z\delta x\delta y\delta t = 0 \tag{2-6}$$

Also, the expression is divided by the element volume $\delta x \delta y \delta z$ and δt. This yields to the integral form:

$$\frac{\partial u}{\partial x} + \frac{\partial v}{\partial y} + \frac{\partial w}{\partial z} = 0 \qquad (2\text{-}7)$$

However, mass (m) of this element is $m = \rho V$, when air density (ρ) is constant (incompressible flow), and its volume (V) does not change, the mass is conservative totally. Eq. (2-8) is three-dimensional mass conservation (the continuity equation) at a point in an incompressible wind flow.

Additionally, the continuity equation is also commonly formed as an **integral form**. Now to derive the integral form of this equation, we consider an arbitrary control volume (V) in fluid domain bellow.
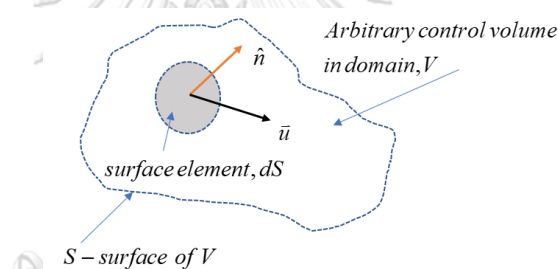
Figure 2-3 An arbitrary control volume in the fluid domain

Assuming $\bar{u}$ is the velocity of the fluid at the surface area dS, the flow rate of mass leaving out volume V through that elemental area is

$$\rho u dS = (\hat{n}.\bar{u})\rho dS \qquad (2\text{-}8)$$

where $\hat{n}$ is the normal vector.

Then integrating over the entire surface, the net rate of mass leaving V is:

$$\int_S \rho u dS = \int_S (\hat{n}.\bar{u})\rho dS \qquad (2\text{-}9)$$

For the conservation of mass, this amount must be equal to the negative rate of mass increasing in V, which is

$$-\int_V \frac{\delta \rho}{\delta t} dV \qquad (2\text{-}10)$$

so that this integral version of the continuity equation becomes

$$\int_S (\hat{n}\bar{u})\rho dS + \int_V \frac{\delta\rho}{\delta t}dV = 0 \qquad (2\text{-}11)$$

For the incompressible flow, density is constant. Continuity equation becomes

$$\int_S \hat{n}\bar{u}dS = 0 \qquad (2\text{-}12)$$

for any arbitrary areas within the computational fluid domain.

2.1.1.2 Conservation of momentum

The rate of change of momentum ($\frac{\Delta p}{\Delta t}$) equals the total forces acting on a fluid particle (Newton's second law), described as

$$\begin{cases} p = mv \\ F = ma \end{cases} F = ma = \frac{m\Delta v}{\Delta t} = \frac{\Delta p}{\Delta t} \qquad (2\text{-}13)$$

where

- p, Δp are momentum and the change of momentum, respectively.

- v, Δv are velocity and the change of particle velocity, respectively.

- F, a, Δt are a total force acting on a fluid particle, particle's acceleration, and force's acting time, respectively.

In the fluid, the forces acting on a fluid particle consist of pressure force and viscous forces.

First, the pressure force on the infinitesimal fluid particle in x-direction will be presented in Figure 2-4.
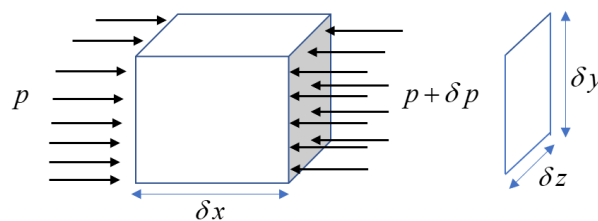
Figure 2-4 Pressure force on the infinitesimal element in the x-direction

Using the Taylor series expansion, we obtain

$$p + \delta p = p + \frac{\partial p}{\partial x} \delta x + h.o.t$$

$$\Rightarrow \delta p = \frac{\partial p}{\partial x} \delta x$$

The net pressure force in x-direction is

$$[p - (p + \delta p)](\delta y \delta z) = -\delta p (\delta y \delta z) = -\frac{\partial p}{\partial x} \underbrace{\delta x \delta y \delta z}_{volume} \tag{2-14}$$

Taking the same process for y-direction and z-direction, the net pressure force on over fluid particle is:

$$-\left(\frac{\partial p}{\partial x} \underbrace{\delta x \delta y \delta z}_{volume} + \frac{\partial p}{\partial y} \underbrace{\delta x \delta y \delta z}_{volume} + \frac{\partial p}{\partial z} \underbrace{\delta x \delta y \delta z}_{volume} \right) \tag{2-15}$$

Alternatively, the net pressure force on the unit volume is

$$-\left(\frac{\partial p}{\partial x} \hat{i} + \frac{\partial p}{\partial y} \hat{j} + \frac{\partial p}{\partial z} \hat{k} \right) = -\nabla p \tag{2-16}$$

Second, the viscous force on the infinitesimal fluid particle will be expressed in Figure 2-5.
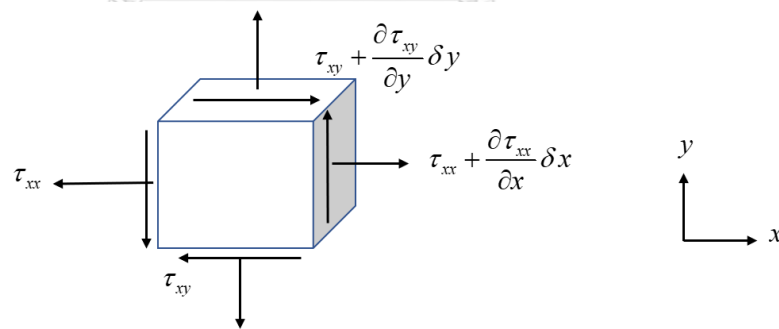
Figure 2-5 Viscous force on the infinitesimal element in x-direction and y-direction

The net shear force in x-direction is:

$$[(\tau_{xy} + \frac{\partial \tau_{xy}}{\partial y} \delta y) - \tau_{xy}](\delta x \delta z) + [(\tau_{zx} + \frac{\partial \tau_{zx}}{\partial z} \delta z) - \tau_{zx}](\delta x \delta y) = \tag{2-17}$$

$$= \frac{\partial \tau_{xy}}{\partial y} \underbrace{\delta x \delta y \delta z}_{volume} + \frac{\partial \tau_{zx}}{\partial z} \underbrace{\delta x \delta y \delta z}_{volume}$$

Also, the net normal stress in the x-direction is

$$[(\tau_{xx} + \frac{\partial \tau_{xx}}{\partial x}\delta x) - \tau_{xx}](\delta y \delta z) = \frac{\partial \tau_{xx}}{\partial x}\underbrace{\delta x \delta y \delta z}_{\text{volume}}$$

(2-18)

From Eq. 2-17 and Eq. 2-18, the net viscous force in x-direction is

$$\frac{\partial \tau_{xx}}{\partial x}\underbrace{\delta x \delta y \delta z}_{\text{volume}} + \frac{\partial \tau_{xy}}{\partial y}\underbrace{\delta x \delta y \delta z}_{\text{volume}} + \frac{\partial \tau_{zx}}{\partial z}\underbrace{\delta x \delta y \delta z}_{\text{volume}}$$

(2-19)

or

$$\frac{\partial \tau_{xx}}{\partial x} + \frac{\partial \tau_{xy}}{\partial y} + \frac{\partial \tau_{xz}}{\partial z}$$

(2-20)

per unit volume in the x-direction.

If the fluid is incompressible and viscosity is constant (Newtonian fluid), this stress equation can be written in terms of an arbitrary coordinate system as

$$\tau_{ij} = \mu\left(\frac{\partial U_i}{\partial X_j} + \frac{\partial U_j}{\partial X_i}\right)$$

(2-21)

where

a. X_i is the ith spatial coordinate

b. U_i is the fluid's velocity in the direction of the axis i

c. τ_{ij} is the jth component of the stress acting on the faces of the fluid element perpendicular to axis i.

From Eq. 2-21, we obtain:

$$\begin{cases} \tau_{xx} = \mu\left(\frac{\partial u}{\partial x} + \frac{\partial u}{\partial x}\right) = 2\mu\left(\frac{\partial u}{\partial x}\right) \\ \tau_{xy} = \mu\left(\frac{\partial u}{\partial y} + \frac{\partial v}{\partial x}\right) \\ \tau_{xz} = \mu\left(\frac{\partial u}{\partial z} + \frac{\partial w}{\partial x}\right) \end{cases}$$

(2-22)

Then, submitting the Eq. 2-22 into Eq. 2-20, we obtain

$$\frac{\partial \tau_{xx}}{\partial x} + \frac{\partial \tau_{xy}}{\partial y} + \frac{\partial \tau_{xz}}{\partial z} = 2\mu\frac{\partial^2 u}{\partial x^2} + \mu\frac{\partial^2 u}{\partial y^2} + \mu\frac{\partial^2 v}{\partial x \partial y} + \mu\frac{\partial^2 u}{\partial z^2} + \mu\frac{\partial^2 w}{\partial x \partial z}$$

$$= \mu\left(\frac{\partial^2 u}{\partial x^2}+\frac{\partial^2 u}{\partial y^2}+\frac{\partial^2 u}{\partial z^2}\right)+\mu\frac{\partial^2 u}{\partial x^2}+\mu\frac{\partial^2 v}{\partial x \partial y}+\mu\frac{\partial^2 w}{\partial x \partial z}$$

$$= \mu\nabla^2 u+\mu\frac{\partial}{\partial x}\left(\frac{\partial u}{\partial x}+\frac{\partial v}{\partial y}+\frac{\partial w}{\partial z}\right) \qquad (2\text{-}23)$$

From mass conservation in Eq. (2-8): $\left(\dfrac{\partial u}{\partial x}+\dfrac{\partial v}{\partial y}+\dfrac{\partial w}{\partial z}\right)=0$. The viscous force of an

infinitesimal particle in the x-direction is $\mu\nabla^2 u$. Following the same process, with y-direction and z-direction, the viscous forces will be $\mu\nabla^2 v$ and $\mu\nabla^2 w$, respectively.

Third, the final component of Newton's second law ($\vec{F}=m\vec{a}$) is acceleration, which would be obtained below.
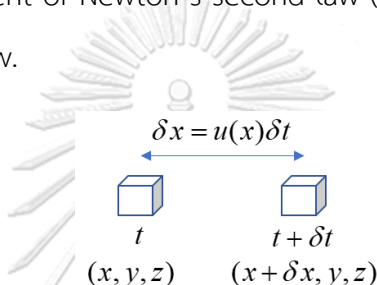
Figure 2-6 The particle after δt in x-direction

Consider a particle at the moment t at coordination (x,y,z) it has a velocity in the x-direction is u. After a short time (δt), it will move to coordinate at $(x+\delta x,y,z)$ (for easy deriving the acceleration, we would consider this particle move along the x-direction, hence coordination in y and z would not change). So, acceleration in the x-direction is

$$a_x = \frac{u[(x+\delta x),y,z]-u(x,y,z)}{\delta t}$$

$$= \frac{[u(x,y,z)+\dfrac{\partial u(x,y,z)}{\partial x}\delta x+h.o.t]-u(x,y,z)}{\delta t} \qquad \text{(Taylor's series expansion)}$$

$$= \frac{\dfrac{\partial u(x,y,z)}{\partial x}\delta x}{\delta t}=\frac{\dfrac{\partial u(x,y,z)}{\partial x}(u\delta t)}{\delta t}=u\frac{\partial u}{\partial x} \qquad (2\text{-}24)$$

where $\delta x = u\delta t$.

Now, if we consider the rest two directions, accelerations would be

$$a_x = u\frac{\partial u}{\partial x} + v\frac{\partial u}{\partial y} + w\frac{\partial u}{\partial z} \tag{2-25}$$

$$a_y = u\frac{\partial v}{\partial x} + v\frac{\partial v}{\partial y} + w\frac{\partial v}{\partial z} \tag{2-26}$$

$$a_z = u\frac{\partial w}{\partial x} + v\frac{\partial w}{\partial y} + w\frac{\partial w}{\partial z} \tag{2-27}$$

Final, Newton's second law is

$$\vec{F} = m\vec{a} = (\rho V)\vec{a} \tag{2-28}$$

alternatively, Newton's second law on the unit volume is

$$\rho\vec{a} = \frac{\vec{F}}{V} \tag{2-29}$$

The right-hand side of Eq. 2-29 is the total force on unit volume, which is the sum of pressure force and viscous force. The left-hand side contains the product of constant density and accelerations, derived above in each direction. Hence, the momentum equation system is

$$\rho\left(u\frac{\partial u}{\partial x} + v\frac{\partial u}{\partial y} + w\frac{\partial u}{\partial z} \right) = -\frac{\partial p}{\partial x} + \mu\nabla^2 u \tag{2-30}$$

$$\rho\left(u\frac{\partial v}{\partial x} + v\frac{\partial v}{\partial y} + w\frac{\partial v}{\partial z} \right) = -\frac{\partial p}{\partial x} + \mu\nabla^2 v \tag{2-31}$$

$$\rho\left(u\frac{\partial w}{\partial x} + v\frac{\partial w}{\partial y} + w\frac{\partial w}{\partial z} \right) = -\frac{\partial p}{\partial x} + \mu\nabla^2 w \tag{2-32}$$

alternatively, presented by a compact form as

$$\rho(\vec{V}\cdot\nabla)\vec{V} = -\nabla p + \mu\nabla^2\vec{V} \tag{2-33}$$

These above equations are well-known with the name Navier–Stokes equations, those equations named after Claude-Louis Navier and George Gabriel Stokes, describe the motion of viscous fluid substances. From the process of deviation, we had to use mass conservation (continuity equations)

$$\frac{\partial u}{\partial x} + \frac{\partial v}{\partial y} + \frac{\partial w}{\partial z} = 0 \tag{2-34}$$

or

$$\nabla \cdot \vec{V} = 0 \qquad (2\text{-}35)$$

That why the Navier–Stokes equations and the continuity equation are the coupled equations. These equations are non-linear because of the existence of $u\dfrac{\partial w}{\partial x}$, $v\dfrac{\partial u}{\partial y}$, etc. (an unknown variable multiplies to an unknown variable's derivative).

Now, coming to the **integral form** of momentum equations. One more time, we consider the arbitrary control volume in the fluid domain. The rate of change of momentum equals the sum of the forces on a fluid particle (The Newton second law). Forces acting on a fluid particle consist of pressure force and viscous forces.
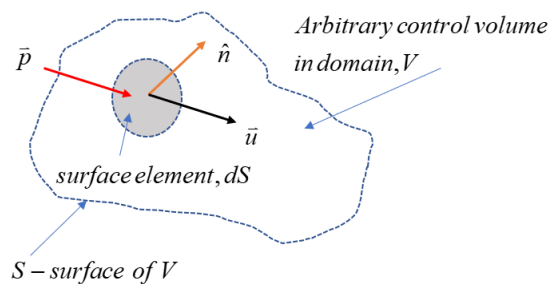
Figure 2-7 An arbitrary control volume in the fluid domain

The pressure force on the entire surface S of V is

$$\int_S -\bar{p}\hat{n}\,dS \qquad (2\text{-}36)$$

Also, the viscous force is denoted as $\vec{F}_{visc}$

The net rate of mass leaving volume V becomes (already mentioned in the integral form of continuity equations)

$$\int_S (\hat{n}.\bar{u})\rho\,dS \qquad (2\text{-}37)$$

Now, multiplying above equation with velocity $\bar{u}$, we obtain the net rate of momentum on the entire surface of V

$$\int_S (\hat{n}.\bar{u})\bar{u}\rho\,dS \qquad (2\text{-}38)$$

Total forces balance the net rate of momentum, so we have the integral form of Navier-Stokes equations for incompressible flow as

$$\int_S (\hat{n}.\bar{u})\bar{u}\rho dS = \int_S -\bar{p}\hat{n}dS + \vec{F}_{visc}$$ (2-39)

Table 2-1 Summary of the governing equations

	Differential form	Integral form
Conservation of mass	$\nabla \cdot \vec{V} = 0$	$\int_S \hat{n}\bar{u}dS = 0$
Conservation of momentum	$\rho(\vec{V} \cdot \nabla)\vec{V} = -\nabla p + \mu \nabla^2 \vec{V}$	$\int_S (\hat{n}.\bar{u})\bar{u}\rho dS = \int_S -\bar{p}\hat{n}dS + \vec{F}_{visc}$

2.1.1.3 Computational Fluid Dynamics (CFD)

As we discussed above, fluid flow is governed by three fundamental conservation laws (mass, momentum, and energy). The mathematical formulation of three laws leads to a set of governing equations for fluid flow. Also, they can be in the differential form or the integral form. Additionally, those equations are coupled and non-linear. In CFD, we solve the governing equations approximately by computer using software that converts the governing equations to a large set of algebraic equations. Then, the set of algebraic equations will be inverted on the computer to solve all the variables. The process above is called CFD, and nowadays, current CFD technology can handle flow around realistic geometries and complex physics.

The software we will use in this study is ANSYS Fluent from ANSYS Inc., which solves the governing equations by a numerical technique called Finite Volume Method (FVM). A wide range of physics can solve by ANSYS Fluent, such as turbulence, chemical reactions, non-Newtonian flows, and deforming boundaries.

2.1.2 CFD simulation sequence

For the wind load analysis, the CFD process would follow bellow sequences:

(1) Geometry: The spatial domain (computational fluid domain) and the 3D objects (the target building and surrounding building area) were created thanks to the computer-aided design programs (CAD). This study used AutoCAD and SketchUp.

(2) Meshing: At this crucial stage, the computational fluid domain is discretized into control volume cells to form a mesh (grid). Guidelines for this would be presented in section 2.1.3.

(3) Model set-up: The chosen boundary conditions, material properties, turbulence model, solution method, solution control parameters, and data output options, which plays an important role in this step. The boundary conditions and the choice of turbulence model are crucial, presented in this chapter.

(4) Solver: the CFD code would discretize the Navier-Stokes equations and solves them on over the computational domain.

(5) Postprocessor (Result analysis): the data from the previous step (velocity flow fields, vorticity, and pressures) would be analyzed and extracted on lines, planes, and other forms of the computational domain.

2.1.3 Discretization of analysis domain

The numerical technique for solving the governing equations of the wind flow is the Finite Volume Method (FVM). This method is used by ANSYS Fluent also some other commercial CFD codes. The basic idea of FVM is breaking fluid domain into small control volumes (cell) and apply the conservation in each one. Moreover, this process will use the governing equations as integral forms. The next result is that we get a set of algebraic equations that can be inverted to variables.
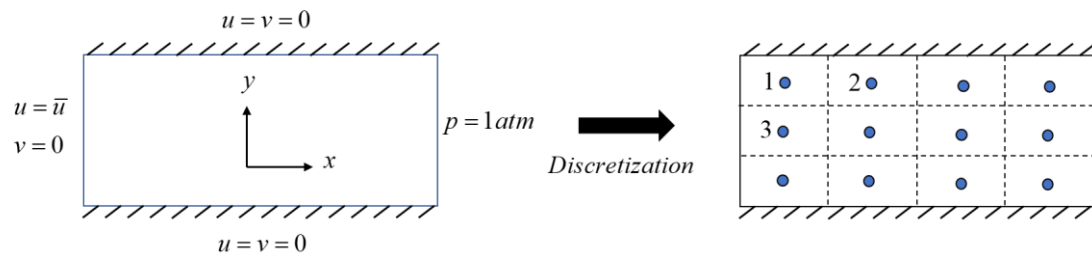
Figure 2-8 Cell discretization of an example by Finite Volume Method (FVM)

Considering a simple 2-dimensions domain described in Figure 2-8, which has full boundary conditions. The left boundary (called inlet) with a specific velocity in x-direction denoted by $u = \bar{u}$ while the velocity in the y-direction equals to 0 ($v = 0$). At the right boundary (called outlet) we had the constant pressure at 1 atm. At the top and bottom boundaries, the flow is limited, velocities in both directions equal to zero (no-slip condition). Equations govern the flow in this domain with three variable functions (2 functions of velocity and one of pressure): $u(x, y)$, $v(x, y)$ and $p(x, y)$.

The discretization will break the whole domain into multiple control volumes or "cells." In the example in Figure 2-8, the fluid domain was divided into 12 cells. Next, we reduce the problem from solving three functions to determining the velocity and pressure values at the cell centers of each cell. In the example, for one cell, we had three unknowns (two velocity-unknowns and one pressure-unknown); Hence, we have 12 cells with 36 total unknowns. Summarily, instead of determining three functions of two velocity-components and one pressure, we need to find 36 unknowns at cell centers.
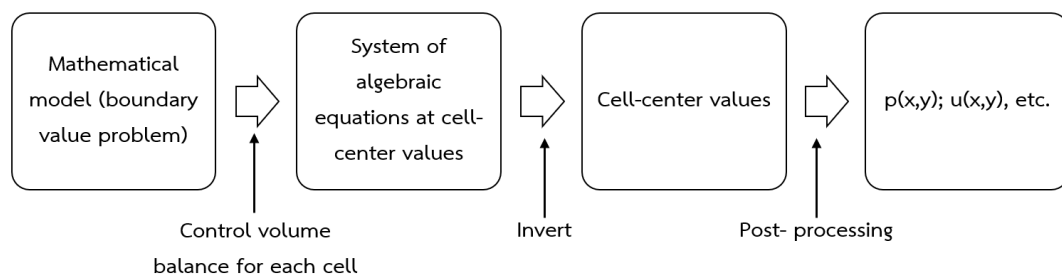
Figure 2-9 How to find velocity and pressure at cell-center?

To derive the algebraic equations from the mathematical model, in FVM, we use the governing equations as integral form rather than the differential form. With the integral form, we apply mass and momentum conservation to each cell. For example, in Figure 2-8, we applied the mass conservation one cell number 1 (cell no.1) by checking the volume of flow crossing each face of the cell; After we have the full contribution of volume flow, then set it equals to zero for mass conservation. Mass and volume are equivalent in the incompressible flow because they are just different by a constant, the density.
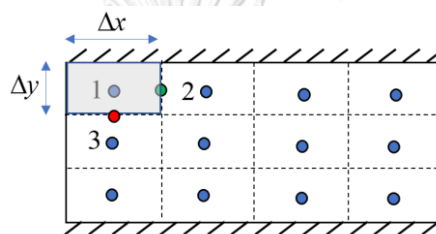
Let us focus on the neighboring face between cell no.1 and cell no.2, assuming the average velocity on this face is equals to the value at the midpoint u_{1-2}, which is shown by the green dot. The volume flow rate $\dot{V}_{1-2}$ (volume per unit time) is between cell no.1, and cell no.2 is

$$\dot{V}_{1-2} = u_{1-2}\Delta y(1) + (error1) \tag{2-40}$$

where

- $\Delta y(1)$ is the area of the neighboring face with assuming the dimension in the perpendicular to the paper equals one (1)

- $error1$ represents the error when assuming the velocity on over the surface equals to one at the midpoint.

The u_{1-2} is the average of the velocity at each cell-center of cell no.1 (u_1) and cell no.2 (u_2), and this generated another error denoted by $error2$.

$$u_{1-2} = \frac{u_1 + u_2}{2} + (error2) \tag{2-41}$$

So, the flow rate $\dot{V}_{1-2}$ now is

$$\dot{V}_{1-2} = \frac{u_1 + u_2}{2} \Delta y(1) + (2 \ errors) \tag{2-42}$$

If we consider the rest neighboring face with cell no.3, we obtain the net flow rate from cell no.1 to no.3 as

$$\dot{V}_{1-3} = \frac{v_1 + v_3}{2} \Delta x(1) + (2 \ errors) \tag{2-43}$$

the left boundary of cell no.1 with a uniform x-direction velocity $u = \bar{u}$, so the volume rate is

$$\dot{V}_{left} = \bar{u} \Delta y(1) \tag{2-44}$$

Also, there is no contribution from the top boundary condition of cell no.1.

Now applying the mass conservation on the cell no.1, the inflow volume rate equals to the outflow volume rate:

$$\dot{V}_{left} = \dot{V}_{1-2} + \dot{V}_{1-3} \tag{2-45}$$

or

$$\left(\frac{\Delta y}{2} \right) u_1 + \left(\frac{\Delta y}{2} \right) u_2 + \left(\frac{\Delta x}{2} \right) v_1 + \left(\frac{\Delta x}{2} \right) v_3 - (\Delta y) \bar{u} + errors = 0 \tag{2-46}$$

and Eq. (2-46) is the **algebraic equation** of mass conservation.

The mass conservation can be applied by integral form on all boundaries of a control volume (cell) or using the physical argument like above. Conservation is guaranteed for each control volume by the mean mass leaving control volume is equal to mass entering; there would be no loss of mass. The same ideas will be applied for momentum and energy conservation. However, there are interpolation errors or discretization errors thrown in through solving, which are unavoidable. Even with a fine mesh, the discretization errors sometimes lead to the unbalance between mass coming in and out or nonphysical results. The error control method will be discussed late in this chapter.

$$\int\limits_{S} (\hat{n}.\bar{u}) \bar{u} \rho \, dS = \int\limits_{S} -\bar{p}\hat{n} \, dS + \bar{F}_{visc} \tag{2-47}$$

The left side of momentum equations (Eq. 2-47) is a non-linear team (product of 2 unknowns, velocity times velocity component), which makes the algebraic equations to be non-linear. Back to the example in Figure 2-8, the rate of momentum flow in the x-direction at the middle face of cell no.1 and no.2 is

$$(\dot{mom}_x)_{1-2} = \rho u_{1-2} u_{1-2} \Delta y(1) + error\,1 \tag{2-48}$$

$$= \rho \left(\frac{u_1 + u_2}{2} \right)^2 \Delta y(1) + error\,1 + error\,2 \tag{2-49}$$

$$= \rho \left(\frac{u_1^2 + u_2^2 + 2u_1 u_2}{4} \right) \Delta y(1) + errors$$

Where the non-linear teams are u_1^2, u_2^2 and $u_1 u_2$. The non-linear teams cannot be solved directly. Then, the Newton method (or Newton-Raphson) will be used to solves momentum equations by linearizing about guess values (iterative solve). In detail, we come to an example of the non-linear term u_1^2. We can split velocity at cell no.1 as

$$u_1 = \underset{guess}{u_{1g}} + \underset{correction}{\Delta u_1} \tag{2-50}$$

The function of u_1 we can write as Taylor's series expansion

$$f(u_1) = f(u_{1g} + \Delta u_1) \tag{2-51}$$

$$= f(u_{1g}) + \Delta u_1 f'(u_{1g}) + \frac{\Delta u_1^2}{2} f''(u_{1g}) + h.o.t \tag{2-52}$$

Now, looking at the case $f(u_1) = u_1^2$

$$\begin{cases} f(u_1) = u_1^2 \rightarrow f'(u_1) = 2u_1 \\ f(u_{1g}) = u_{1g}^2 \rightarrow f'(u_{1g}) = 2u_{1g} \end{cases} \tag{2-53}$$

then submit back to the Taylor series, we obtain

$$u_1^2 = u_{1g}^2 + \Delta u_1 (2u_{1g}) + linearization\,error \tag{2-54}$$

The linearization error becomes small as the guess value (u_{1g}) tends to toward the exact solution, and the correction (Δu_1) becomes smaller and smaller.
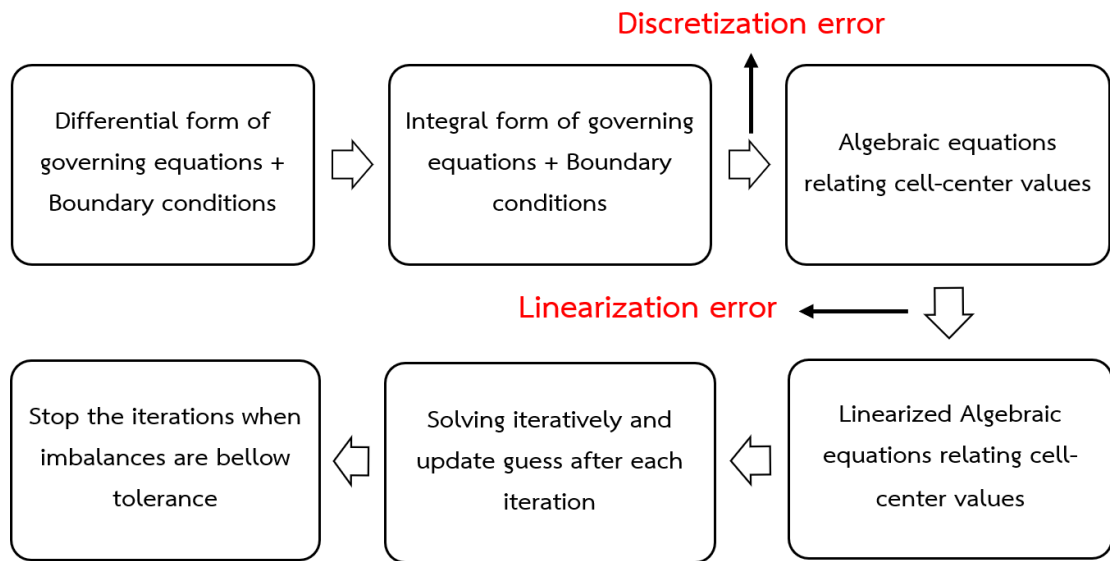
Figure 2-10 Discretization and linearization overview

The process of solving will generate two types of error, one is discretization error, which can be reduced by a fine mesh. In contrast, the other, linearization error, relates to the order of accuracy. Both errors need to control by the determined tolerance (in ANSYS Fluent, it is one of inputs information known as residuals) to stopping the iterative solving. Now we will answer the question, "how do we know when to stop iterating?" by going back to the example. The algebraic equation of mass conservation is

$$\left(\frac{\Delta y}{2}\right)u_1 + \left(\frac{\Delta y}{2}\right)u_2 + \left(\frac{\Delta x}{2}\right)v_1 + \left(\frac{\Delta x}{2}\right)v_3 - (\Delta y)\bar{u} = 0 \tag{2-55}$$

where u_1, u_2, v_1 and v_2 as exact values. However, after an iteration, the solution will come to approximate values, which are denoted by u_1^c, u_2^c, v_1^c and v_2^c, respectively. Now, submitting all the values again to the algebraic equations of mass conservation, the right-hand side of equations cannot be equals to zero any more and will become an error or an imbalance mass (R_i).

$$\left(\frac{\Delta y}{2}\right)u_1^c + \left(\frac{\Delta y}{2}\right)u_2^c + \left(\frac{\Delta x}{2}\right)v_1^c + \left(\frac{\Delta x}{2}\right)v_3^c - (\Delta y)\bar{u} = R_i \tag{2-56}$$

we aggregate all mass imbalances or mass residuals (also referred to as continuity residual) as

$$R = \frac{\sum |R_i|}{scale\ factor} \leq Tolerance \tag{2-57}$$

The absolute values mean whether the residual is negative or positive; it is also a mass imbalance or an error. We need to scale the aggregate mass imbalance by a scaling factor because it would seem like a small mass imbalance for a supersonic flow while a more massive imbalance for low-speed flow. Then, we will stop the iterations when this aggregate imbalance is less than some tolerance.

The same ideas will be applied to momentum equations; the momentum rate of a cell is not balanced with the net forces happing in each cell after an iteration, then it products a momentum residual. All the momentum residuals will be aggregated to be a momentum imbalance, and the iterative solving stops when that momentum imbalance is less than a particular tolerance.
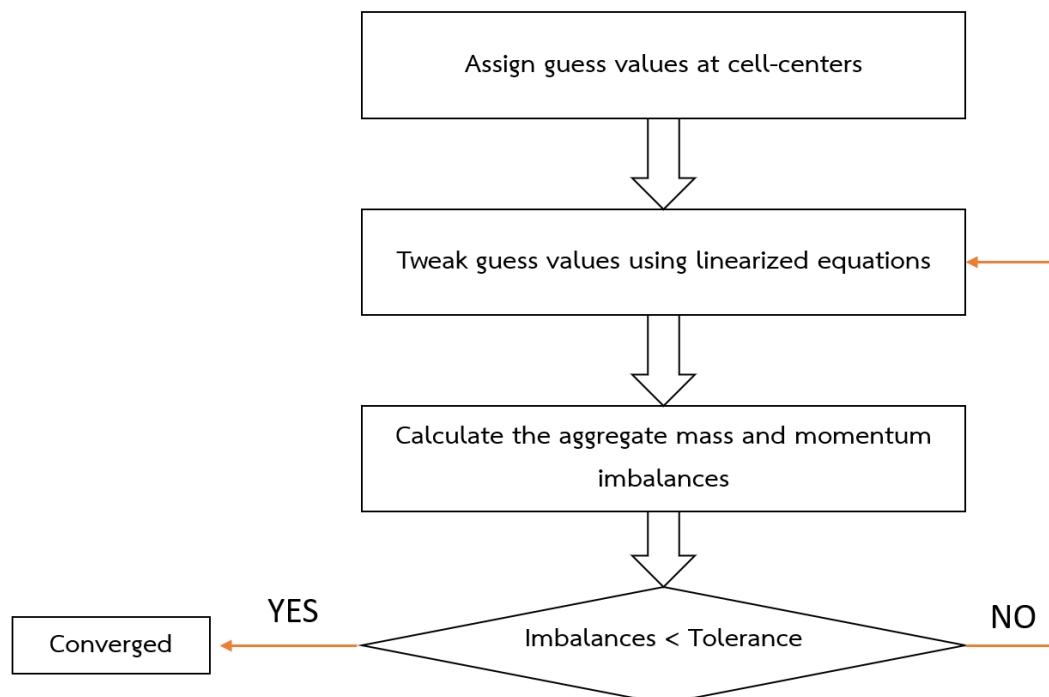
Figure 2-11 Algorithm for the iterative solving process

At the point when the imbalances of mass and momentum are below than specified tolerance levels and, we have a good-enough solution to a non-linear set of algebraic equations, we could stop the iteration with a convergent solution.

2.2 Turbulence flow definition

In fluid dynamics, turbulence or turbulent flow is fluid motion described by chaotic fluctuations in pressure and flow velocity. It is opposite a laminar flow, which happens when a fluid flows in parallel streamlines, with no disruption between those streamlines. Turbulent flow is linked to a non-dimensional quality called the flow **Reynold number**, which is the ratio of the inertial forces and the viscous forces. In practice, the Reynolds number is used to determine whether the flow is laminar or turbulent.

$$Re = \frac{inertial\ force}{viscous\ force} \tag{2-58}$$

From Figure 2-12, we can see the variation of Reynold number affecting the flow characteristics. The low Reynold number presents a flow with parallel streamlines, while the more increasing Reynold number, the more chaotic flow is.
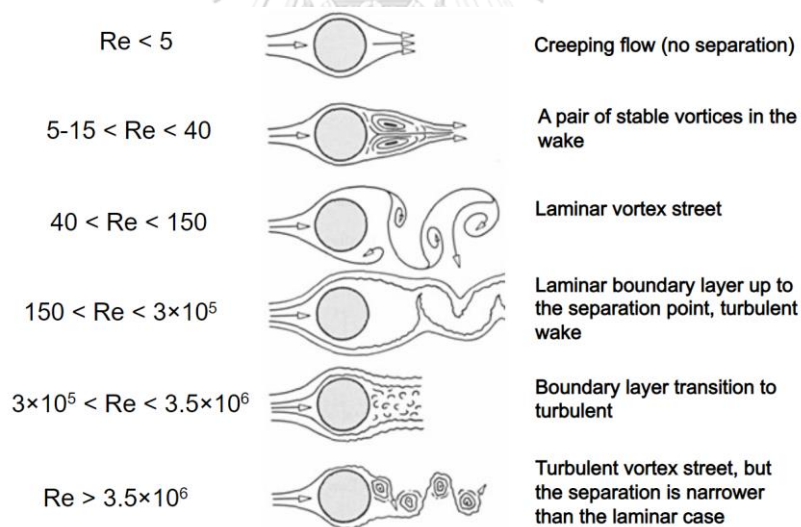
Figure 2-12 The Reynold numbers for different types of flow

(From ANSYS training document – Used courtesy of ANSYS, Inc.)

In the external flow, such as a flow over a building, there is a complicated layer form of turbulence flow. Imagine flow with a free stream velocity u_∞ approaching a plate in Figure 2-13. At the wall, the velocity is zero due to the wall's friction; however, at a distance far from the wall, the flow has a velocity u_∞. The boundary layer starts as

a low Reynold number as the laminar flow, which means the inertia forces are much smaller with viscous forces. When distance increases along with the plate, the inertia forces dominate (the increasing of Reynold number), causing the flow is more turbulent and chaotic. A transient zone happens before the turbulent is fully developed with chaotic eddies. Underneath the turbulence region, there is still a region remains laminar, called laminar sublayer.
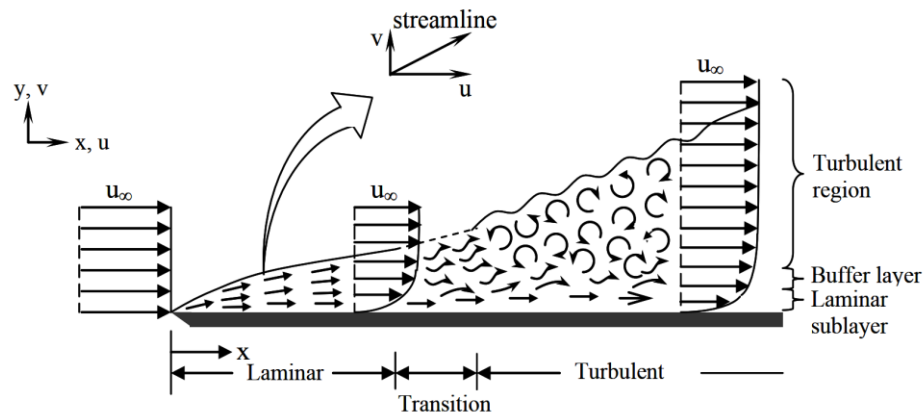
Figure 2-13 Boundary layer over a flat plate (Sayma, 2009)

Consider the measurement of velocity at one arbitrary point in turbulent flow with time variation. A signal in Figure 2-14 was collected. For highly turbulent flows, the fluctuation is variable, unpredictable, and random. The mean or average velocity is useful for most engineering applications. The average or mean of velocity (or other flow characteristics) can be calculated by time averaging over an integral time variation.

$$\bar{u} = \frac{1}{\Delta t} \int_{t}^{t+\Delta t} u \, dt \tag{2-59}$$

where

$$u = \bar{u} + u' \tag{2-60}$$

The same idea would be used to other variables such as pressure and velocity in the y-direction. Then,

$$p = \bar{p} + p' \tag{2-61}$$

and

$$v = \bar{v} + v'$$ (2-62)
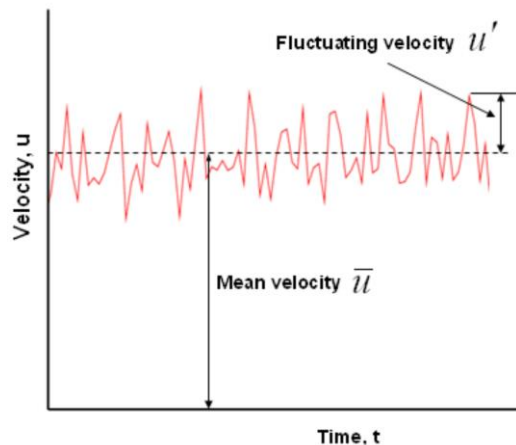
Figure 2-14 Instantaneous and average velocity in turbulent flow (Sayma, 2009)

The decomposition of velocity in Eq. (2-60) to the mean velocity and fluctuation, is known as **Reynolds decomposition**; Also, the average (mean) velocity is also called Reynold average velocity. Now we need to modify the governing equations in terms of Reynold average quantities. First, we come to the continuity equation

$$\frac{\partial u}{\partial x} + \frac{\partial v}{\partial y} + \frac{\partial w}{\partial z} = 0$$ (2-63)

Taking the Reynold decomposition, we had $u = \bar{u} + u'$, $v = \bar{v} + v'$, and $w = \bar{w} + w'$ which presented for velocity component of three directions at one arbitrary point within the fluid domain. Average these terms we obtain $u = \bar{u} + u' \rightarrow \bar{u} = \bar{u} + \bar{u'} \Rightarrow \bar{u'} = 0$. The same idea was applied; we got:

$$\begin{cases} \bar{u'} = 0 \\ \bar{v'} = 0 \\ \bar{w'} = 0 \end{cases}$$ (2-64)

From Eq. 2-63, we apply the Reynold decomposition on all variables and average it we obtain

$$\frac{\partial(\overline{u}+u')}{\partial x}+\frac{\partial(\overline{v}+v')}{\partial y}+\frac{\partial(\overline{w}+w')}{\partial z}=0 \tag{2-65}$$

$$\Rightarrow \frac{\partial(\overline{u}+\overline{u}')}{\partial x}+\frac{\partial(\overline{v}+\overline{v}')}{\partial y}+\frac{\partial(\overline{w}+\overline{w}')}{\partial z}=0 \tag{2-66}$$

$$\Rightarrow \frac{\partial\overline{u}}{\partial x}+\frac{\partial\overline{v}}{\partial y}+\frac{\partial\overline{w}}{\partial z}+\frac{\partial\overline{u}'}{\partial x}+\frac{\partial\overline{v}'}{\partial y}+\frac{\partial\overline{w}'}{\partial z}=0 \tag{2-67}$$

$$\Rightarrow \frac{\partial\overline{u}}{\partial x}+\frac{\partial\overline{v}}{\partial y}+\frac{\partial\overline{w}}{\partial z}=0 \tag{2-68}$$

So, Eq. 2-68 is the Reynold-Average version of the continuity equation, which looks the same with the original version. The difference will happen on the Navier-Stokes equations. Now back to the Navier-Stoke equation in the x-direction, which is

$$\rho\frac{\partial u}{\partial t}+\rho\left(u\frac{\partial u}{\partial x}+v\frac{\partial u}{\partial y}+w\frac{\partial u}{\partial z}\right)=-\frac{\partial p}{\partial x}+\mu\nabla^2 u \tag{2-69}$$

The equation is not like the previous equations derived as Eq. (2-30), with the additional term ($\rho\frac{\partial u}{\partial t}$) on the left-hand side, which is the velocity fluctuation following time variation. This term exists because the flow is unsteady. Applying the Reynold decomposition and average equation we have

$$\rho\left(\overline{u}\frac{\partial\overline{u}}{\partial x}+\overline{v}\frac{\partial\overline{u}}{\partial y}+\overline{w}\frac{\partial\overline{u}}{\partial z}\right)=-\frac{\partial\overline{p}}{\partial x}+\mu\nabla^2\overline{u}-\rho\left(\overline{u}\frac{\partial\overline{u}'}{\partial x}+\overline{v}\frac{\partial\overline{u}'}{\partial y}+\overline{w}\frac{\partial\overline{u}'}{\partial z}\right) \tag{2-70}$$

Let us break down. On the left side, this term is the acceleration due to the movement of fluid-particle, which calls the convection term; the first two terms in the right-hand side of equations present for the **Reynold average pressure** and **viscous forces**. Finally, the additional last term that involves the product of three fluctuations in 3 dimensions. Now rewriting this extra term and use the continuity relation, we obtain

$$\rho\left(\overline{u}\frac{\partial\overline{u}}{\partial x}+\overline{v}\frac{\partial\overline{u}}{\partial y}+\overline{w}\frac{\partial\overline{u}}{\partial z}\right)=-\frac{\partial\overline{p}}{\partial x}+\mu\nabla^2\overline{u} \tag{2-71}$$

$$+\underbrace{\left(\frac{\partial}{\partial x}(-\rho\overline{u'u'})+\frac{\partial}{\partial y}(-\rho\overline{u'v'})+\frac{\partial}{\partial z}(-\rho\overline{u'w'})\right)}_{\overline{f}_{turb,x}}$$

Three notable terms $-\rho\overline{u'u'}$, $-\rho\overline{u'v'}$ and $-\rho\overline{u'w'}$ which behave like stress terms; the first is normal stress term, and the rest are shear stress terms. These additional terms are the product of turbulence, which represents the effect of fluctuation velocity on the average fields. They are well-known as Reynold-stresses. Now if we write the Reynold shear stress or turbulent shear stress (denoted by $\tau_{xy}{}^{t}$) as an analogous term with viscous stress, we have

$$-\rho\overline{u'v'} = \tau_{xy}{}^{t} = \mu_{t}\left(\frac{\partial\overline{u}}{\partial y} + \frac{\partial\overline{v}}{\partial x}\right)$$
(2-72)

where μ_t is the eddy-viscosity, which can think as analogous to the molecular fluid viscosity μ (a fluid characteristic). The greater eddy-viscosity is the more significant shear stress caused by turbulence.

$$Viscous\ shear\ stress \qquad Turbulent\ shear\ stress$$

$$\tau_{xy} + \frac{\partial\tau_{xy}}{\partial y}\delta y \qquad\qquad \tau^{t}{}_{xy} + \frac{\partial\tau^{t}{}_{xy}}{\partial y}\delta y$$

$$\tau_{xy} \qquad\qquad\qquad \tau^{t}{}_{xy}$$
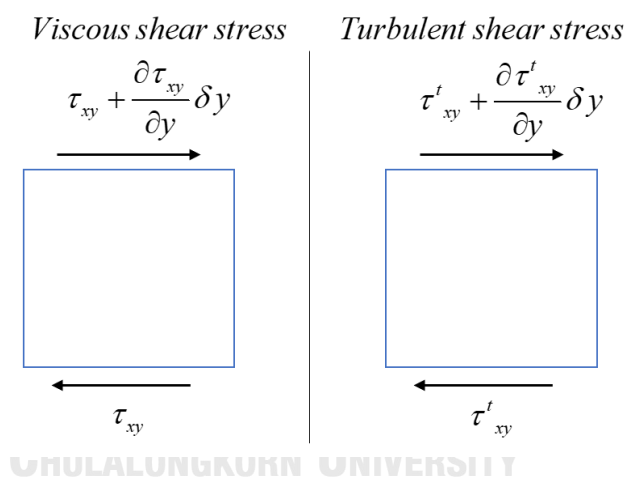
Figure 2-15 Viscous and turbulent shear stress

Prandtl proposed this approach, called the eddy-viscosity turbulence model, and obviously, it is not a conservation law. All the processes based on guesswork, but it is an excellent assumption because the hypothesized Reynold-stresses term behaves like the viscous stresses term. All the processes based on guesswork, but it is an excellent assumption because the hypothesized Reynold-stresses term behaves like the viscous stresses term. Keep in mind the turbulent viscosity (μ_t) is not a material

property; it is the function and needs to be calculated as a part of the solution process and would be mentioned in section 2.3.

Applied same ideas for the rest directions, the set of governing equations, which are the Reynold-average continuity equations and the Reynold-Average Navier-Stokes equations (RANS) written as

$$\frac{\partial \overline{u}}{\partial x} + \frac{\partial \overline{v}}{\partial y} + \frac{\partial \overline{w}}{\partial z} = 0 \tag{2-73}$$

$$\rho\left(\overline{u}\frac{\partial \overline{u}}{\partial x} + \overline{v}\frac{\partial \overline{u}}{\partial y} + \overline{w}\frac{\partial \overline{u}}{\partial z}\right) = -\frac{\partial \overline{p}}{\partial x} + \mu\nabla^2\overline{u} + f_{turb,x}(u_t, \overline{u}, \overline{v}, \overline{w}) \tag{2-74}$$

$$\rho\left(\overline{u}\frac{\partial \overline{u}}{\partial x} + \overline{v}\frac{\partial \overline{u}}{\partial y} + \overline{w}\frac{\partial \overline{u}}{\partial z}\right) = -\frac{\partial \overline{p}}{\partial y} + \mu\nabla^2\overline{v} + f_{turb,y}(u_t, \overline{u}, \overline{v}, \overline{w}) \tag{2-75}$$

$$\rho\left(\overline{u}\frac{\partial \overline{u}}{\partial x} + \overline{v}\frac{\partial \overline{u}}{\partial y} + \overline{w}\frac{\partial \overline{u}}{\partial z}\right) = -\frac{\partial \overline{p}}{\partial x} + \mu\nabla^2\overline{w} + f_{turb,x}(u_t, \overline{u}, \overline{v}, \overline{w}) \tag{2-76}$$

The whole set of governing equations contains three unknown functions of Reynold average velocity components $(\overline{u}(x,y,z); \overline{v}(x,y,z); \overline{w}(x,y,z))$, one function of pressure force $(\overline{p}(x,y,z))$, and the turbulent viscosity (μ_t). The discretization process will base on the same idea with the process in 2.1.3 in order to transfer governing equations to set of algebraic equations; however, the appearance of a new variable (μ_t) needs to be provided one additional equation to solve all variables.

2.3 Turbulence models

Like discussion at the last of the previous part, we need one additional equation for solving turbulent viscosity (μ_t). All the turbulence models are a numerical approach method to calculate this parameter.

2.3.1 Spalart-Allmaras model

The Spalart-Allmaras model (Spalart and Allmaras, 1992)is a one-equation model that solves turbulent viscosity by only one modeled transport equation. This model

was mostly used for the aerospace (wall-bounded flows) and turbomachinery applications.

The original Spalart-Allmaras model is only suitable for low Re number flow, which means the viscosity-influenced regions need to be resolved. Recently, by using the Enhanced Wall Treatment, Spalart-Allmaras model has been modified to apply in various applications with various flow types.

The turbulent viscosity is computed from

$$\mu_t = \rho \tilde{v} f_{v1} \tag{2-77}$$

where the viscous damping function is given by

$$f_{v1} = \frac{\chi^3}{\chi^3 + \chi_{v1}^{\ 3}} \tag{2-78}$$

and

$$\chi = \frac{v}{\tilde{v}} \tag{2-79}$$

The transportation equation $\tilde{v}$ is

$$\frac{\partial}{\partial t}(\rho \tilde{v}) + \frac{\partial}{\partial x_i}(\rho \tilde{v} u_i) = G_v + \frac{1}{\sigma_{\tilde{v}}}\left[\frac{\partial}{\partial x_i}\left\{(\mu + \rho \tilde{v})\frac{\partial \tilde{v}}{\partial x_j}\right\} + C_{b2\rho}\left(\frac{\partial \tilde{v}}{\partial x_j}\right)^2\right] - Y_v + S_{\tilde{v}} \tag{2-80}$$

Where G_v is the production of turbulent viscosity, which equals to

$$G_v = C_{b1}\rho \tilde{S}\tilde{v} \tag{2-81}$$

$$\tilde{S} \equiv S + \frac{\tilde{v}}{\kappa^2 d^2} f_{v2} \tag{2-82}$$

$$f_{v2} = 1 - \frac{\chi}{1 + \chi f_{v1}} \tag{2-83}$$

and d is the distance to the wall, and S is the deformation tensor's scalar measure. In ANSYS Fluent, as in the original model proposed by Spalart and Allmaras, S is based on the vorticity magnitude.

$$S = \sqrt{2Q_{ij}Q_{ij}} = \frac{1}{2}\left(\frac{\partial \mu_i}{\partial x_j} - \frac{\partial \mu_j}{\partial x_i}\right) \tag{2-84}$$

Y_v is the destruction of turbulent viscosity, which occurs in the near-wall area due to wall blocking and viscous damping:

$$Y_v = C_{w1}\rho f_w \left(\frac{\tilde{v}}{d}\right)^2 \tag{2-85}$$

$$f_w = g\left(\frac{1+C_{w3}^6}{g^6+C_{w3}^6}\right)^{1/6} \tag{2-86}$$

$$g = r + C_{w2}(r^6 - r) \tag{2-87}$$

$$r \equiv \frac{\tilde{v}}{\tilde{S}\kappa^2 d^2} \tag{2-88}$$

where v is a user-defined source term and $\sigma_{\tilde{v}}$ & $C_{b2\rho}$ are the constants.

Some of constants were used in the above equation (Spalart and Allmaras, 1992):

$$C_{b1} = 0.1355, \quad C_{b2} = 0.662, \quad \sigma_{\tilde{v}} = \frac{2}{3}, \quad C_{v1} = 7.1$$

$$C_{w1} = \frac{c}{\kappa^2} + \frac{(1+C_{b2})}{\sigma_{\tilde{v}}}, \quad C_{w2} = 0.3, \quad C_{w3} = 2.0, \text{ and } \kappa = 0.4187$$

Dacles-Mariani et al. (1995) proposed modification on the original model that concerned the mean strain rate on turbulence production. It was described

$$S \equiv |\Omega_{ij}| + C_{prod} \min\left(0, |S_{ij}| - |\Omega_{ij}|\right) \tag{2-89}$$

where $C_{prod} = 2.0$, $|\Omega_{ij}| = \sqrt{2\Omega_{ij}\Omega_{ij}}$, $|S_{ij}| = \sqrt{2S_{ij}S_{ij}}$

$$\Omega_{ij} = \frac{1}{2}\left(\frac{\partial \mu_i}{\partial x_j} - \frac{\partial \mu_j}{\partial x_i}\right) \tag{2-90}$$

$$S_{ij} = \frac{1}{2}\left(\frac{\partial \mu_i}{\partial x_j} + \frac{\partial \mu_j}{\partial x_i}\right) \tag{2-91}$$

2.3.2 The $k-\varepsilon$ turbulence model

In the $k-\varepsilon$ turbulence model μ_t will be calculated by two parameters, that are the turbulent kinetic energy (k) and its dissipation (ε) as

$$\mu_t = \rho C_\mu \frac{k^2}{\varepsilon} \tag{2-92}$$

where

k is the turbulent kinetic energy, which is a measure of how much the energy contained in the fluctuation. So, the more significant fluctuation is, the larger k is.

ε is the turbulence dissipation, which is a measure of the rate at how turbulent kinetic energy is dissipated.

$C_\mu = 0.09$ is an adjustable constant.

The first $k-\varepsilon$ turbulence model is presented by Launder and Spalding (1972) called the Standard $k-\varepsilon$ turbulence model. Time changes, historically, the development of this model has not stopped. RNG $k-\varepsilon$ model (Orszag, 1993) and the Realizable $k-\varepsilon$ model (Shih et al., 1995) were born later to improve the accuracy of the original one. The turbulent kinetic energy (k) and its dissipation (ε) are calculated from the following transport equations in Standard $k-\varepsilon$ turbulence model:

$$\frac{\partial}{\partial t}(\rho k)+\frac{\partial}{\partial x_i}(\rho k u_i)=\frac{\partial}{\partial u_j}\left[\left(\mu+\frac{\mu_t}{\sigma_k}\right)\frac{\partial k}{x_j}\right]+G_k+G_b-\rho\varepsilon-Y_M+S_k \tag{2-93}$$

$$\frac{\partial}{\partial t}(\rho\varepsilon)+\frac{\partial}{\partial x_i}(\rho\varepsilon u_i)=\frac{\partial}{\partial x_j}\left[\left(\mu+\frac{\mu_t}{\sigma_\varepsilon}\right)\frac{\partial\varepsilon}{\partial x_j}\right]+C_{1\varepsilon}\frac{\varepsilon}{k}(G_k+C_{3\varepsilon}G_b)$$
$$-C_{2\varepsilon}\rho\frac{\varepsilon^2}{k}+S_\varepsilon \tag{2-94}$$

In the above equations, G_k stands for the generation of k due to the mean velocity gradients, calculated by

$$G_k=-\overline{\rho\mu_i'\mu_j'}\frac{\partial\mu_j}{\partial x_i} \tag{2-95}$$

or by the Boussinesq hypothesis,

$$G_k=\mu_t S^2 \tag{2-96}$$

where S is the mean rate-of-strain tensor's modulus, known as

$$S=\sqrt{2S_{ij}S_{ij}}=\sqrt{2\left(\frac{1}{2}\left(\frac{\partial\mu_j}{\partial x_i}+\frac{\partial\mu_i}{\partial x_j}\right)\right)^2} \tag{2-97}$$

G_p presents the generation of k due to buoyancy, calculated by

$$G_p = \beta g_i \frac{\mu_t}{Pr_t} \frac{\partial T}{\partial x_i} \qquad (2\text{-}98)$$

where Pr_t is the turbulent Prandtl number for energy and g_i the gravitational vector's component in the ith direction. For the Standard and Realizable $k - \varepsilon$ models, the default value of Pr_t is 0.85; β is thermal expansion coefficient:

$$\beta = -\frac{1}{\rho}\left(\frac{\partial \rho}{\partial T}\right)_p \qquad (2\text{-}99)$$

$C_{1\varepsilon} = 1.44$, $C_{2\varepsilon} = 1.92$, $C_\mu = 0.09$, $\sigma_k = 1.0$ and $\sigma_\varepsilon = 1.3$ are model constants following the default value (Launder and Spalding, 1972) from experiments for fundamental turbulent flows;

Y_M represents the contribution of the fluctuating dilatation in compressible turbulence flow to the overall dissipation rate.

$$Y_M = 2\rho\varepsilon M_t^2 \qquad (2\text{-}100)$$

where M_t is the turbulent Mach number as

$$M_t = \sqrt{\frac{k}{a^2}} \qquad (2\text{-}101)$$

where $a = \sqrt{\gamma RT}$ is the sound speed.

Furthermore, S_k an S_ω are user-defined source terms that are provided in ANSYS Fluent to help users to modify the equations.

Now, it is coming to the RNG $k - \varepsilon$ model (Orszag, 1993). The RNG $k - \varepsilon$ model was derived by a statistical technique, called "renormalization group theory" (RNG) which is similar in the original form of the standard $k - \varepsilon$ model, however, includes the following improvement:

- The additional term in the dissipation equation helps improve the accuracy for rapidly stained flows

• RNG model now includes the effect of swirl on turbulence, that enhances the accuracy for swirling flows

• In the standard model, the Prandtl number used as a constant value, while the RNG theory provides an analytical formula to derive this parameter.

• The RNG theory provides an analytically differential form to calculate the effective viscosity, that allows this model to handle the low Reynold number and near-wall flow, better than the standard model.

All the above improvement makes the RNG $k-\varepsilon$ model more accurate and reliable than the standard $k-\varepsilon$ model in various flow types.

Shih et al. (1995) presented the realizable $k-\varepsilon$ model, which is not identical to the standard $k-\varepsilon$ model in:

- Introduce a new alternative formulation for the turbulent viscosity.
- A modified the dissipation equation rate, which is derived from an exact equation for the transport of the mean-square vorticity fluctuation.

The term "realizable" means this model can satisfy specific mathematical constraints on Reynolds' stresses, which are compatible with the physics of the turbulent flow. In contrast, both the Standard $k-\varepsilon$ model and the RNG $k-\varepsilon$ model are not realizable.

All three models: standard $k-\varepsilon$, the RNG $k-\varepsilon$, and the realizable $k-\varepsilon$ have been used in ANSYS Fluent codes. The detail of the transport equations of the RNG $k-\varepsilon$ model and the realizable $k-\varepsilon$ model will not be presented in this study. We highly recommended referring to the free publication form ANSYS Inc. "ANSYS Fluent theory guide" (Fluent, 2013).

2.3.3 The $k-\omega$ turbulence model

The $k-\omega$ turbulence model is one of the famous used in CFD. Like the $k-\varepsilon$ turbulence models, The $k-\omega$ is a two-equation turbulence model with the transport equations for turbulent kinetic energy (k) and its dissipation ω. The $k-\omega$ turbulence model used in ANSYS Fluent was based on the Wilcox model provided by Wilcox (1998). Wilcox model focus on modifying the low Re number effecting on compressibility and shear flow spreading, but it is sensitive for the solution at shear layers (free-stream sensitivity). Even, ANSYS Fluent has provided the new formulation to reduce this dependency, but it can still have a significant effect on the solution, especially for free shear flow.

The standard $k-\omega$ model's transport equations are:

$$\frac{\partial}{\partial t}(\rho k)+\frac{\partial}{\partial x_i}(\rho k u_i)=\frac{\partial}{\partial u_j}\left(\Gamma_k \frac{\partial k}{\partial x_j}\right)+G_k+Y_M+S_k \tag{2-102}$$

$$\frac{\partial}{\partial t}(\rho\omega)+\frac{\partial}{\partial x_i}(\rho\omega u_i)=\frac{\partial}{\partial x_j}\left(\Gamma_\omega \frac{\partial \omega}{\partial x_j}\right)+G_\omega-Y_\omega+S_\omega \tag{2-103}$$

In transport equations, G_k represents the generation of k due to mean velocity gradients (defined in 2.3.2); G_ω for the generation of ω. Y_k, Y_ω describe the dissipation of k and ω due to turbulence, respectively. Also, S_k and S_ω are user-defined source terms that are provided in ANSYS Fluent to help users to modify the equations.

- The effective of diffusivity (denoted by Γ_k and Γ_ω) is defined as

$$\Gamma_k=\mu+\frac{\mu_t}{\sigma_k} \tag{2-104}$$

$$\Gamma_\omega=\mu+\frac{\mu_t}{\sigma_\omega} \tag{2-105}$$

where σ_k and σ_ω are the Prandtl numbers of k and ω.

- Product of ω is given by

$$G_\omega=\alpha\frac{\omega}{k}G_k \tag{2-106}$$

where G_k was defined in 2.3.2; the coefficient α is given by

$$\alpha = \frac{\alpha_\infty}{\alpha}\left(\frac{\alpha_0 + Re_t / R_\omega}{1 + Re_t / R_\omega}\right)$$

(2-107)

where $R_\omega = 2.95\alpha^*$ and the Re_t is given by the equation (2-127).

- The dissipation k is given by

$$Y_k = \rho\beta^* f_{\beta^*} k\omega$$

(2-108)

where

$$f_{\beta^*} = \begin{cases} 1 & (\chi_k \leq 0) \\ \dfrac{1 + 680\chi_k^2}{1 + 400\chi_k^2} & (\chi_k > 0) \end{cases}$$

(2-109)

where

$$\chi_k = \frac{1}{\omega^3}\frac{\partial k}{\partial x_j}\frac{\partial \omega}{\partial x_j}$$

(2-110)

and

$$\beta^* = \beta_i^*\left[1 + \zeta^* F(M_t)\right]$$

(2-111)

$$\beta_i^* = \beta_\infty^*\left(\frac{4/15 + (Re_t / R_\beta)^4}{1 + (Re_t / R_\beta)^4}\right)$$

(2-112)

$$\zeta^* = 1.5$$

(2-113)

$$R_\beta = 8.0$$

(2-114)

$$\beta_\infty^* = 0.09$$

(2-115)

where Re_t is given by Eq. (2-127).

The dissipation for ω is given by

$$Y_\omega = \rho\beta f_\beta \omega^2$$

(2-116)

where

$$f_\beta = \frac{1 + 70\chi_\omega}{1 + 80\chi_\omega}$$

(2-117)

$$\chi_\omega = \left| \frac{\Omega_{ij}\Omega_{jk}S_{ki}}{\left(\beta_\infty^*\omega\right)^3} \right| \tag{2-118}$$

$$\Omega_{ij} = \frac{1}{2}\left(\frac{\partial u_i}{\partial x_j} - \frac{\partial u_j}{\partial x_i} \right) \tag{2-119}$$

The equation gives the strain rate tensor in (2-91)

$$\beta = \beta_i\left[1 - \frac{\beta_i^*}{\beta_i}\zeta^* F\left(M_t\right) \right] \tag{2-120}$$

where $F\left(M_t\right)$ is the compressible functions given by

$$F\left(M_t\right) = \begin{cases} 0 & (M_t \le M_{t0}) \\ M_t^2 - M_{t0}^2 & (M_t > M_{t0}) \end{cases} \tag{2-121}$$

where

$$M_t^2 = \frac{2k}{a^2} \tag{2-122}$$

$$M_{to} = 0.25 \tag{2-123}$$

$$a = \sqrt{\gamma RT} \tag{2-124}$$

For the case of high-Reynold number flows, the coefficient becomes $\beta_i^* = \beta_\infty^*$, in the compressible form $\beta^* = \beta_i^*$.

- Model constants

$$\alpha_\infty^* = 1; \alpha_\infty = 0.52; \alpha_0 = \frac{1}{9}; \beta_\infty^* = 0.09; \beta_i = 0.072; R_\beta = 8$$

$$R_k = 6; R_\omega = 2.95; \zeta^* = 1.5; M_{t0} = 0.25; \sigma_k = 2; \sigma_\omega = 2$$

After all, the turbulent viscosity μ_t is followed as

$$\mu_t = \alpha^*\frac{\rho k}{\omega} \tag{2-125}$$

In the above equation, the coefficient α^* is a correction for low-Reynolds number flows, defined as

$$\alpha^* = \alpha_\infty^*\left(\frac{\alpha_0^* + \mathrm{Re}_t/R_k}{1 + \mathrm{Re}_t/R_k} \right) \tag{2-126}$$

where

$$Re_t = \frac{\rho k}{\mu \omega} \tag{2-127}$$

also, constants $R_k = 6, \alpha_0^* = \frac{\beta_i}{3}, \beta_i = 0.072$

For the case of high-Reynold number flows, the coefficient becomes maximum as

$\alpha^* = 1$

2.3.4 The Menter SST $k - \omega$ turbulence model

Menter (1994) developed the shear-stress transport (SST) $k - \omega$ model, which combines the robust and accuracy of the $k - \omega$ model at the near-wall region, and the $k - \varepsilon$ model's free stream independence at the far-field. The $k - \omega - SST$ model is like the standard $k - \omega$ model, but it includes some refinement bellow:

- Both of standard $k - \omega$ model and the $k - \varepsilon$ model is added in $k - \omega - SST$ model. Now, Introducing a "blending function," which helps to move the calculation to the standard $k - \omega$ model in the near-wall region, while it will be zero to active the $k - \varepsilon$ model in the region far away from the surface (far-fields).

- The $k - \omega - SST$ model includes a damped cross-diffusion derivative term in the dissipation ω equation.

- Modifying the turbulent viscosity to work with the transportation of turbulent shear stress.

- The modeling constants are different from the standard $k - \omega$ model.

The $k - \omega - SST$ model has similar transport equations to the standard $k - \omega$ model:

$$\frac{\partial}{\partial t}(\rho k) + \frac{\partial}{\partial x_i}(\rho k u_i) = \frac{\partial}{\partial u_j}\left(\Gamma_k \frac{\partial k}{\partial x_j}\right) + G_k - Y_k + S_k \tag{2-128}$$

$$\frac{\partial}{\partial t}(\rho \omega) + \frac{\partial}{\partial x_j}(\rho \omega u_i) = \frac{\partial}{\partial x_j}\left(\Gamma_\omega \frac{\partial \omega}{\partial x_j}\right) + G_\omega - Y_\omega + D_\omega + S_\omega \tag{2-129}$$

In these equations, some difference with the standard $k-\omega$ model will be described below:

- The effective of diffusivity (denoted by Γ_k and Γ_ω) is defined as

$$\Gamma_k = \mu + \frac{\mu_t}{\sigma_k} \tag{2-130}$$

$$\Gamma_\omega = \mu + \frac{\mu_t}{\sigma_\omega} \tag{2-131}$$

where σ_k and σ_ω are the Prandtl numbers of k and ω, respectively, defined as

$$\sigma_k = \frac{1}{F_1 / \sigma_{k,1} + (1-F_1)/\sigma_{k,2}} \tag{2-132}$$

$$\sigma_\omega = \frac{1}{F_1 / \sigma_{\omega,1} + (1-F_1)/\sigma_{\omega,2}} \tag{2-133}$$

where

$$F_1 = \tanh\left(\Phi_1^4\right) \tag{2-134}$$

$$\Phi_1 = \min\left[\max\left(\frac{\sqrt{k}}{0.09\omega y}, \frac{500\mu}{\rho y^2 \omega}\right), \frac{4\rho k}{\sigma_{\omega,2} D_\omega^+ y^2}\right] \tag{2-135}$$

$$D_\omega^+ = \max\left[2\rho \frac{1}{\sigma_{\omega,2}} \frac{1}{\omega} \frac{\partial k}{\partial x_j} \frac{\partial \omega}{\partial x_j}, 10^{-10}\right] \tag{2-136}$$

with y is the distance to the next surface, and D_ω^+ is the positive portion of the cross-diffusion term.

- The product of ω

$$G_\omega = \frac{\alpha}{v_t} G_k \tag{2-137}$$

where G_k is defined in section 2.3.1; the coefficient α is given by

$$\alpha = \frac{\alpha_\infty}{\alpha}\left(\frac{\alpha_0 + Re_t / R_\omega}{1 + Re_t / R_\omega}\right) \tag{2-138}$$

In the $k-\omega-SST$ model α_∞ is not a constant like in the standard $k-\omega$ model, it is defined as

$$\alpha_\infty = F_1 \alpha_{\infty,1} + (1-F_1)\alpha_{\infty,2} \tag{2-139}$$

where

$$\alpha_{\infty,1} = \frac{\beta_{i,1}}{\beta_{\infty}^*} - \frac{\kappa^2}{\sigma_{w,1}\sqrt{\beta_{\infty}^*}} \tag{2-140}$$

$$\alpha_{\infty,2} = \frac{\beta_{i,2}}{\beta_{\infty}^*} - \frac{\kappa^2}{\sigma_{w,2}\sqrt{\beta_{\infty}^*}} \tag{2-141}$$

where $\kappa = 0.41$

- Dissipation of k and ω

The term Y_k in the $k-\omega-SST$ model is defined similarly with the standard $k-\omega$ model with only one difference, which is the term f_{β^*} now becomes a constant equal to 1, thus

$$Y_k = \rho\beta^* k\omega \tag{2-142}$$

Similarly, the term Y_ω differs from the standard $k-\omega$ model at term β_i and term f_β. The term f_β now becomes a constant equal to 1; while the β_i is defined as a function as

$$\beta_i = F_1\beta_{i,1} + (1-F_1)\beta_{i,2} \tag{2-143}$$

Then

$$Y_\omega = \rho\beta_i\omega^2 \tag{2-144}$$

- An additional term of cross-diffusion modification D_ω

To blend the two models $k-\omega$ and $k-\varepsilon$, the $k-\omega-SST$ adds a new term D_ω called cross-diffusion

$$D_\omega = 2(1-F_1)\rho\sigma_{\omega,2}\frac{1}{\omega}\frac{\partial k}{\partial x_j}\frac{\partial \omega}{\partial x_j} \tag{2-145}$$

- Model constants

$$\sigma_{k,1} = 1.176; \sigma_{\omega,1} = 2; \sigma_{k,2} = 1; \sigma_{\omega,2} = 1.168;$$

$$a_1 = 0.31; \beta_{i,1} = 0.075; \beta_{i,2} = 0.0828$$

After all, the modify of turbulent viscosity is defined as

$$\mu_t = \frac{\rho k}{\omega} \frac{1}{\max\left[\dfrac{1}{\alpha^*}, \dfrac{SF_2}{a_1\omega}\right]} \tag{2-146}$$

where

$$F_2 = \tanh\left(\Phi_2^2\right) \tag{2-147}$$

$$\Phi_2 = \max\left[2\frac{\sqrt{k}}{0.09\omega y}, \frac{500y}{\rho y^2\omega}\right] \tag{2-148}$$

2.4 Large Eddy Simulation (LES)

2.4.1 Governing equations

Before getting to know about Large Eddy Simulation (LES), we need to understand the basic idea of Direct numerical simulation (DNS). DNS is a time-dependent simulation in CFD, which solve the flow governing equations directly without any turbulence model like RANS. DNS solves the turbulence in the full range of spatial and temporal scales. From the Kolmogorov microscales (which generates the smallest vortex) up to the integral scale (which contains most of the kinetic energy and generate the large eddy). Therefore, DNS requires a high-resolution mesh and extensive computational resources and hard to approach in practical.
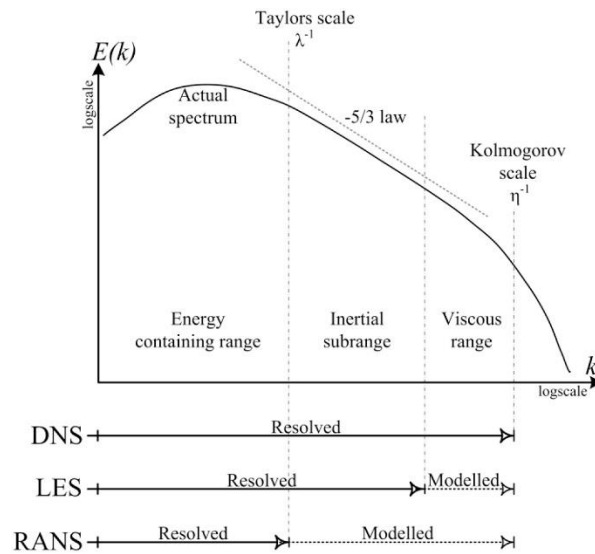
Figure 2-16 The correlation between a power density spectrum and turbulence

modeling

(Thordal et al., 2019)

The LES is also a simulation that is directly solving the governing equations in a time-dependent solution. However, in contrast to DNS, the only large scale of eddies are resolved, while these smaller are modeled. A spatial filtering operation is integrated to separate the larger eddies and the smaller ones, making LES a space averaging method and opposite to the time-averaging turbulence models – RANS. LES provides a filtering operation that could filter out any eddies smaller than the "cut-off" width and only release the larger eddies to resolved. The filtering of a variable ϕ can be described as

$$\bar{\phi}(x,t) = \int_{domain} \phi(x,t)G(x,x',\Delta)dx' \tag{2-149}$$

where $\bar{\phi}(x,t)$ are filtered variables, $\phi(x,t)$ are unfiltered variables, G is the filtering function, and Δ is the cut-off width.

In the commercial software, the is the cut-off width (Δ) is calculated from the size of the smallest grid size. The chosen cut-off width smaller than the smallest grid size is meaningless because the numerical solution just solves variables only on the cell sizes. The cut-off width often calculated by

$$\Delta = \sqrt[3]{\Delta x \Delta y \Delta z} \tag{2-150}$$

where Δx, Δy, Δz are the grid size for the three-dimension, respectively.

After the filtering, now, the momentum equation is rewritten as

$$\rho \frac{\partial \overline{u}_i}{\partial t} + \rho \frac{\partial \overline{u_i u_j}}{\partial x_j} = -\frac{\partial \overline{p}}{\partial x_i} + \mu \nabla^2 \overline{u} - \frac{\partial \tau_{ij}}{\partial x_j} \tag{2-151}$$

Between the resolved-scales (large eddies) and unresolved scales (smaller ones, which also called the sub-grid scale (SGS) eddies), is contained the sub-grid scale stress (τ_{ij}). The decomposition τ_{ij} can be written as

$$\begin{aligned} \tau_{ij} &= \rho \overline{u_i u_j} - \rho \overline{u}_i \overline{u}_j \\ &= (\rho \overline{\overline{u}_i \overline{u}_j} - \rho \overline{u}_i \overline{u}_j) + (\rho \overline{\overline{u}_i u'_j} + \rho \overline{u'_i \overline{u}_j}) + (\rho \overline{u'_i u'_j}) \\ &= \qquad L_{ij} \qquad + \qquad C_{ij} \qquad + \quad R_{ij} \end{aligned} \tag{2-152}$$

where

    (1) L_{ij} are the Leonard stresses which contain information of the resolved scales exclusively.

    (2) C_{ij} are the Cross-tresses which present the interaction between the resolved and unresolved scales.

    (3) R_{ij} are the LES Reynold stresses, which are created by convective transfer between the SGS eddies. These stresses are like the Reynold stresses in the RANS and only relate to the unresolved eddies. Hence, Sub-Grid Scale (SGS) models would be used to handle those stressed.

2.4.2 The key of Sub-Grid Scale (SGS) models

Smagorinsky (1963) introduced a model for stresses R_{ij} in 1963, known as the first SGS model. The model's basic idea is that the local SGS stresses R_{ij} have a ratio with the local rate of strain of the resolved flow $\overline{S}_{ij}$, which define in Versteeg and Malalasekera (2007) as

$$R_{ij} = -\mu_{SGS} \left(\frac{\partial \overline{u}_i}{\partial x_j} + \frac{\partial \overline{u}_j}{\partial x_i} \right) + \frac{1}{3} R_{ii} \delta_{ij} \tag{2-153}$$

where the SGS eddy viscosity is

$$\mu_{SGS} = \rho L_s^2 \left| \overline{S} \right| \tag{2-154}$$

where $L_s = min(\kappa d, C_{SGS}\Delta)$ is the mixing length for SGS model; with κ is the von Karman constant, d is the distance to the closest wall, C_{SGS} is a constant, and $\left| \overline{S} \right| = \sqrt{2\overline{S}_{ij}\overline{S}_{ij}}$.

C_{SGS} in the standard Smagorinsky (1963) SGS model is a constant and has been optimized in Murakami (1997) between 0.1 to 0.25. The large C_{SGS} cause excessive damping of large-scale fluctuations in transitional flows as the near-solid boundary. So that C_{SGS} cannot be a universal constant, and other SGS models have been introduced C_{SGS} as a function of time and space. However, C_{SGS} equals to 0.1 has been found to yield the best results for a wide range of flows, and this value is as default in ANSYS Fluent.

In the dynamic Smagorinsky-Lilly model, the C_{SGS} was dynamically modified based on the characteristics of the resolved flow parts.

$$C_{SGS} = -\frac{1}{2}\frac{L_{ij}M_{ij}}{M_{kl}^2} \tag{2-155}$$

where L_{ij} are previously defined as the Leonard stresses, and

$$M_{ij} = \overline{\overline{\Delta}^2 \left| \overline{\overline{S}} \right| \overline{\overline{S}}_{ij}} - \overline{\overline{\Delta^2 \left| \overline{S} \right| \overline{S}_{ij}}} \tag{2-156}$$

Additionally, Porté-Agel et al. (2000) provided a better optimization of the Smagorinsky-Lilly model. Near the wall region, the length scales become comparable to the distance to the wall. This near-wall model was proven to perform better than the other released before. In the LES simulation, it is assumed that the flow which closes to the wall will be resolved; it means the first node must be very close to the wall boundary; and, it required a high-resolution grid if the wall function cannot be used.

CHAPTER 3

WIND TUNNEL TEST DESCRIPTION

The wind tunnel test (WTT) data was collected based on the experiment, which was conducted by Assoc. Prof. Dr. Virote Boonyapinyo and his colleges at Thammasat University Research and Consultancy Institute (TU-RAC), Pathum Thani, Thailand, in 2016 (Boonyapinyo et al., 2016).

The target building consists of 48 stories floor, located in the center of Bangkok, Thailand. The building has 31.86 m width, 71.51 m depth, and 149.50 m roof height. The study building has the following unique characteristics: (1) a flexible building, (2) having an irregular shape, and (3) located in a dense area of surrounding buildings.

In WTT, the 1:400 scale models of the target structure and its surrounding area within a 400m radius were mounted on a 2m diameter turntable. This table can rotate to represent different wind directions. In other words, 36 wind directions at 10-degree intervals were considered in WTT. The WTT's wind condition was regenerated to get the same condition in the building's location, such as wind velocity profile, turbulent intensity, and turbulence spectrum density.

Figure 3-1 Three-dimensional view of studied building in WTT (Boonyapinyo et al., 2016)

The WTT's wind simulation and testing are compatible with the provision of in ASCE Manual of Practice No. 67 (1999), "Wind Tunnel Studies of Buildings and Structures"

and the requirements of the Department of Public Works and Town & Country Planning, Thailand – Standard No. 1311-50 (DPT, 2007), "Wind Loading Calculation and Response of Buildings."

According to the DPT Standard 1311-50 (DPT, 2007), the reference velocity pressure for the design of primary structure and cladding shall be based on a probability of being exceeded in any one year of 1 in 50 (50-year return period) corresponding to reference wind speed of 25 m/s at the height of 10 m in open terrain. Because the proposed building is in the urban terrain, exposure C was applied in this study, and the typhoon factor equals 1.0. Then, the design wind speed is $\bar{V} = T_F V_{50} = 1.0 \times 25 = 25\,m/s$, and corresponding to the design wind speed of 28.19 m/s at the 149.50 m (roof height) in exposure C.

The tunnel cross-section is 2.5m × 2.5m with 25.5 m in total length, which can generate the wind speed from 0.5 to 20m/s. A system of spires, barrier, and roughness elements generate boundary layer wind at a length scale of 1/400. For details, three triangular spires were used as vortex generators by being placed at the trailing edge of contraction. The fetch of roughness elements is 12-m long.
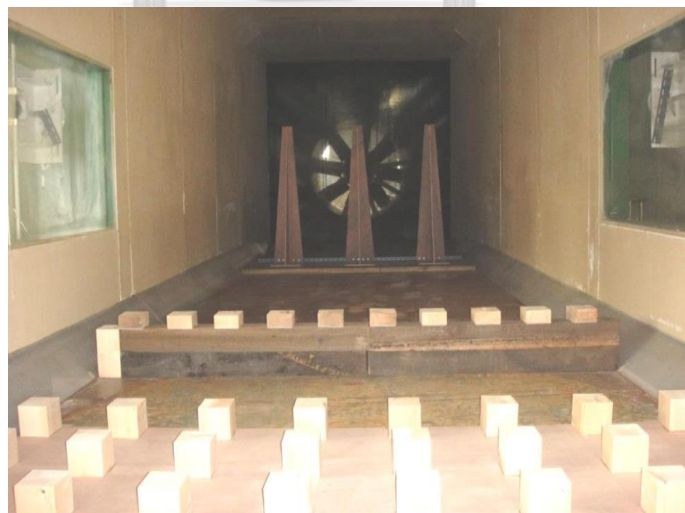
Figure 3-2 Spires, barrier and roughness elements along the wind tunnel floor
(Boonyapinyo et al., 2016)

The test was carried out at a mean wind speed of 7.58 m/s at the roof height of the wind tunnel. Therefore, the velocity scale is $7.58/26.22 = 1/3.46$, resulting in a time scale $(1/400)/(1/3.46) = 1/115.73$. Similarly, the frequency scale is 115.73. The sampling frequency was 400 Hz., which means that pressure fluctuations with frequencies up to $400/115.73 = 3.46\,Hz$ in full scale (prototype) were captured without distortion or attenuation. The pressure data were recorded for about $3600 \times (1/115.73) = 62.21s$, corresponding to 2 hours on the full scale.

Table 3-1 Reference wind speeds and typhoon factor (DPT, 2007)

Zone	Area	V_{50}	T_F
Zone 1	Central	25	1.0
Zone 2	Lower part of the Northern region and East-west border region	27	1.0
Zone 3	Upper part of the Northern region	29	1.0
Zone 4A	East coast of Southern peninsula	25	1.2
Zone 4B	Phetchaburi and West coast of Southern peninsula	25	1.08
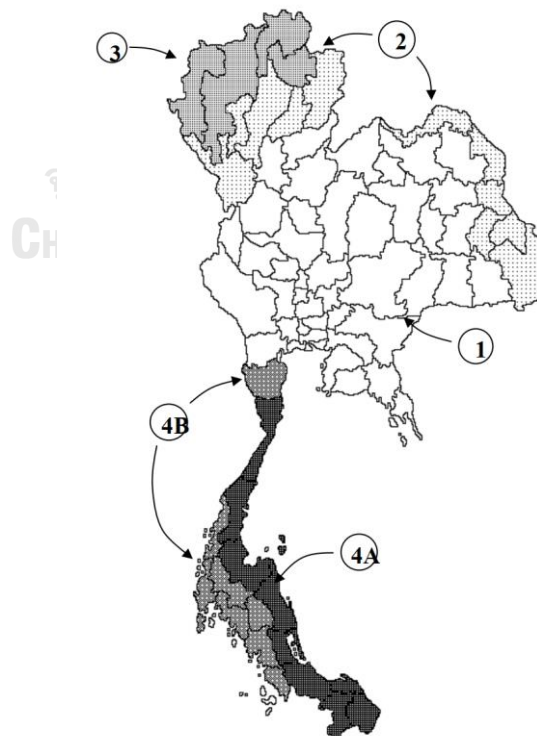
Figure 3-3 Reference wind speed for Thailand (DPT, 2007)

CHAPTER 4

CFD SIMULATION BY ANSYS FLUENT

The CFD simulation sequence, briefly presented in 2.1.2, will be deployed in detail in this chapter.

4.1 Simulation cases

In this study, three cases would be simulated.

(1) Wind simulation on the target building without the neighboring area with the Large Eddy Simulation (LES) approach, denoted by LES–isolated case.

(2) Wind load simulation on the target building with the neighboring area with $k-\omega-SST$ turbulence model (RANS) approach, denoted by SST–SBs case.

(3) Wind simulation on the target building with the neighboring area using the Large Eddy Simulation (LES) approach, denoted by LES–SBs case

In these cases, the wind direction is selected at 270°, corresponding with the same wind direction in WTT, and using the same data of this wind direction to evaluate the accuracy of CFD. Also, based on the current CFD development, this study will concentrate only on the most effective, usable, and accurate simulations, which are the $k-\omega-SST$ turbulence model and LES.

This study aims to evaluate the accuracy of CFD in wind load analysis. In other words, the main comparison will be on the LES-SBs case simulation and WTT data. Besides, the comparison between LES-SBs case simulation and SST-SBs case would indicate the accuracy and applicability of these two approaches. Finally, the influence of the neighboring area (SBs) in the simulation would be mentioned by the difference between the two cases: LES-isolated case and LES–SBs case.

4.2 Geometry of buildings

The target building within 400m surrounding buildings needs to be re-created as virtual 3D objects by Computer-aided design (CAD) and then imported to the ANSYS

Fluent. The geometry's size of the target building was collected directly from the wind tunnel test data while surrounding building geometries were collected thanks to Google Map tools and the internet information.
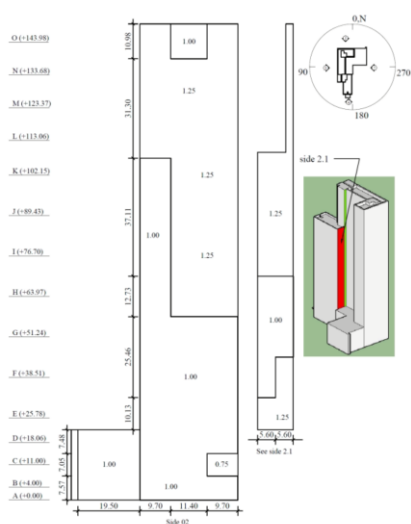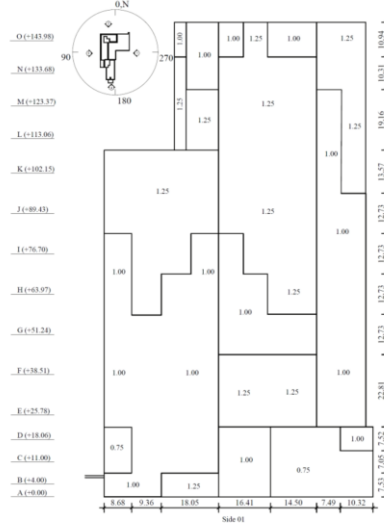
Figure 4-1 Geometry measurement of the target building in WTT (Boonyapinyo et al., 2016)
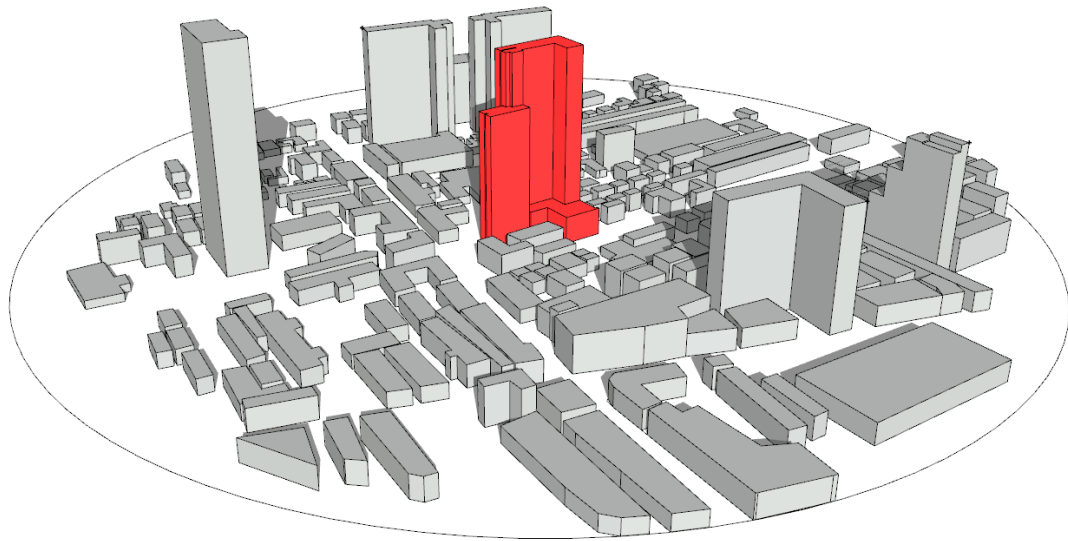
Figure 4-2 The geometry in the simulation of CFD (above) and WTT (below)
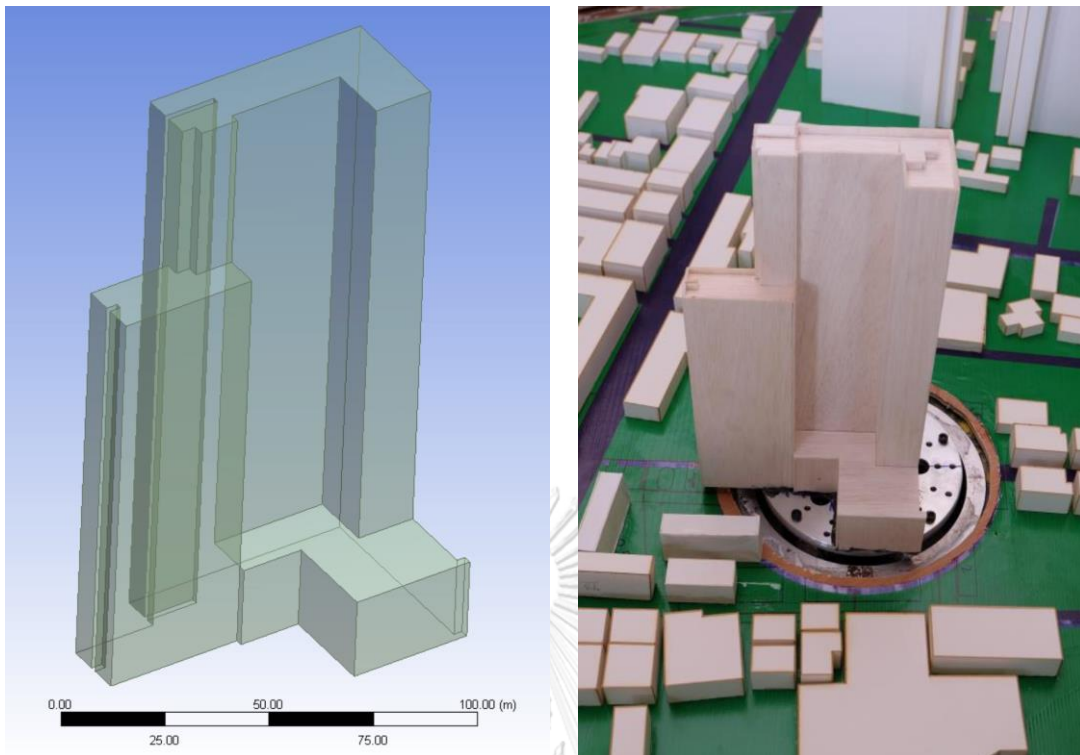
Figure 4-3 The target building in CFD simulation (left) and WTT (right)

4.3 Computational domain

The computational domain (CD) is where the flow is computed based on solving the governing equations. CD should be large enough to fully develop all relevant flow characteristics that influence the region of interest, but not too large to affect the computational cost.

AIJ (2017) recommended that, if H is the height of the target building, the analysis domain extends 5H away from the building and neighboring area to the top and lateral sides except for the back (leeward) side, where the outlet side is 10H away from the neighboring area (Tominaga et al., 2008). While J Franke et al. (2004) recommended similarly except increasing the distance behind the building to the outlet to 15H, then the domain size is 5H, 15H, 5H, and 5H, respectively. Moreover, based on some previous experience, this recommendation of CD size allows the Atmosphere boundary layer (ABL) to develop fully. One notices that if the CD is too

large, which leads to increase the distance with the main building, hence, the flow energy would dissipate before reaching the interesting area (buildings); that means it makes a reduction of wind load on the target building, especially for LES. Another reason is that the larger CD is, a significant computational resource will be taken. In this study, the target building is about 150m height, and the surrounding building within a 400m radius, the domain size will be set up as

(1) Inlet is 400+(150x5) =1150m from the front side of the target building.
(2) Outlet is 400+(150x15) =2650m from the backside of the target building.
(3) Two lateral boundaries are 400+(150x5) =1150m far from the target building.
(4) The top boundary is 150x5 = 750m height.

So, the size of the domain is 2300m x 750m x 3800m; by a scale of 1/400, it will be 5.75m x 1.875 x 9.5m. The size of the domain will apply similarly to all cases of simulation, especially to evaluate the influence of surrounding buildings in CFD simulation.
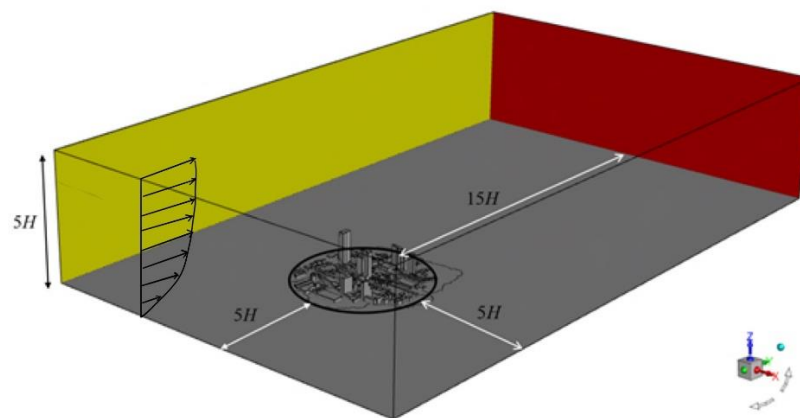
Figure 4-4 CFD domain size

4.4 Mesh

The quality of mesh has a tremendous impact on the accuracy of simulation, also the computational cost. In wind load analysis, the pressure on the surface, like the wall of the building (cladding surface), is of interest; it is vital to make a fine mesh in

the near-wall region. There is a way to use the high-quality layered poly-prism mesh, which will be added in the near-wall area and the bottom layer of the computational domain. These poly-prism layers are always to be set as a minimum number; because they make the total cells increases massively, which is unwanted in computational saving. Hexahedral, polyhedral, or tetrahedral elements generally were used to fill in the bulk region to accomplish the whole mesh.
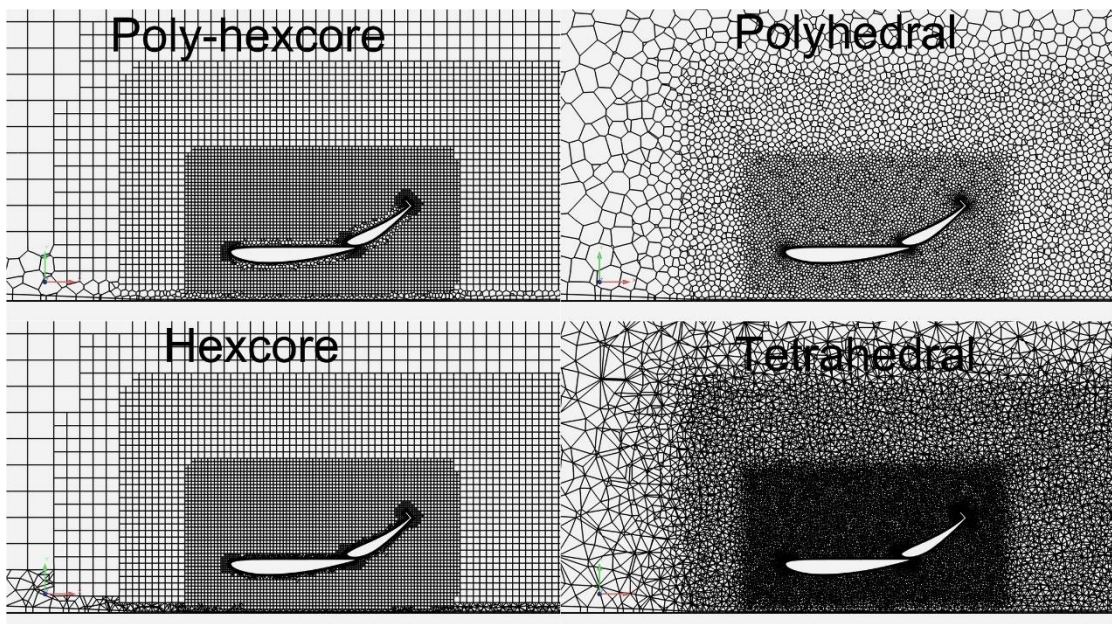
Figure 4-5 Few grid types have been used in CFD
(copyright belongs to Hashan Mendis)

Hexahedral Elements

The advantage of hexahedral or quadrilateral cells are very accurate and save computational sources. In the early days of CFD, when CFD had just solved some simple application with basic geometries, this type of mesh was pretty widely used. Time changes and solution of CFD has been getting more complicated on both flow characteristics and geometries. Thus, hexahedral mesh shows its weakness in complicated areas or too many curve shapes. Hence, this mesh type is often used to fill the far-field area, which is dominated by air or solid. Furthermore, taking a

combination with a different type of mesh, which can be well adapt with curve shapes, is the best solution.

2D Cell Types

Triangle   Quadrilateral

3D Cell Types

Tetrahedron   Hexahedron

Prism/Wedge   Pyramid   Polyhedron
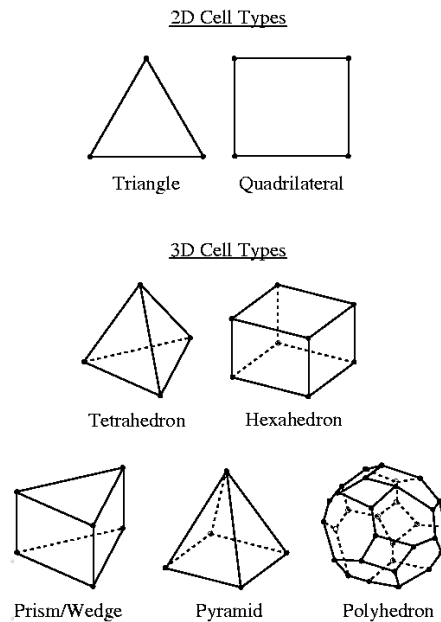
Figure 4-6 Hexahedral elements are well-known as cubes

Tetrahedral (TET)/ Wedge Elements/ Pyramid Elements

Easy to catch all the complex geometry properties, easy to generate automatically, and combine with the other solution has more than one type of mesh inside are the great points of a tetrahedral mesh. These advantages made this mesh used until a decade or so ago. The accuracy of this type of mesh has been argued, but easily came over by solver improvement. However, one big shot that made engineer nowadays limit using this type of mesh because it generates a vast number of cell, which increase computational resources.

Polyhedral Elements

Around 2010, a new mesh type was developed in the CFD application is Polyhedral and showed their promising strong points with other kinds of mesh. Now we make a comparison between the TET and polyhedral elements. The conclusion is

(1) With a control volume, polyhedral mesh reduces the significant number of elements.

(2) One polyhedral cell has 12- 14 faces (compared to four faces of a TET cell); thus, it has more neighbor cells than TET's one. FVM calculate on face centroid values and cell centroid values, so that, the increasing of information around one cell, the more accurate calculation.

(3) In the solving process, polyhedral cells tend to use much more memory (RAM) than TETS, but in the same domain size, the total cell in the polyhedral mesh is significantly less than TET mesh. Overall, the polyhedral mesh saves more computational cost.
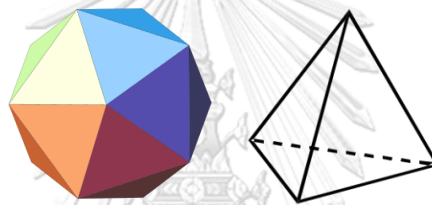
Figure 4-7 Example of polyhedral (left) and TET cell (right)

Mosaic technology and Poly-Hexco mesh

In the CFD simulation, there is no type of cell that is better of accuracy than the others if it would not be fine enough. The critical purpose is that which mesh will be better in saving the solution time. On the one hand, It noted that hexahedral elements are strong in accuracy and efficiency. On the other hand, polyhedral elements are more efficient and well-suited with complex geometries. ANSYS Fluent developers developed a type of mesh named **Poly-Hexcore**, which combines both types of elements and automatically generated by a connecting algorithm (mosaic technology).

Poly-hexcore mesh is the first application of Mosiac technology. It fills the bulk region with octree hexes (cube – the hexahedral elements). A hexahedral element has fewer face than a polyhedral one, which reduces the memory or the storage

space. Next, it generates high-quality poly-prism layers in the near-wall regions. Finally, it builds the connection between them by the layers of the polyhedral element. The polyhedral layers generate a smooth transition between meshes and maintain their high-quality. ANSYS, Inc. did many cases in CFD application to prove outstanding of new mesh about accuracy and computational time-saving in a White Paper *"ANSYS Fluent Mosaic Technology Automatically Combines Disparate Meshes with Polyhedral Elements for Fast, Accurate Flow Resolution."*

In this study, the Poly-Hexcore mosaic technology mesh was used in all cases. In the cases of simulation with isolated target building only, the number of polyhedral cells gets 4,184,929 cells, while it creases to 5,856,047 cells in simulation cases with surrounding buildings.

Primary building without surrounding area: isolated-case mesh (4,18 million cells)

This case uses Poly-Hexcore mesh, which contained only the target building and the fluid domain. A high-solution mesh (also known as a sub-mesh area), which is near the target building, was generated to capture wind flow characteristics in front & back of the primary building. The wall of the building and the ground (bottom face of the domain) are treated as no-slip walls, combine with one inlet, one outlet, and three-symmetric-surface.
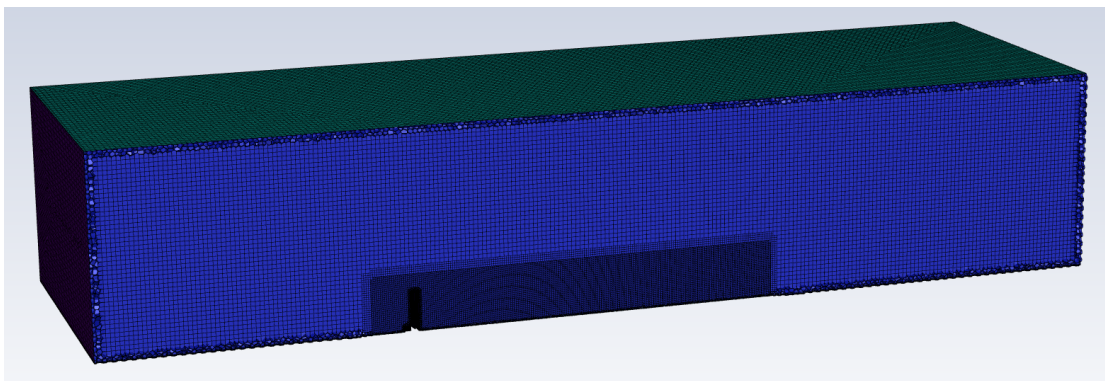
Figure 4-8 The isolated case mesh
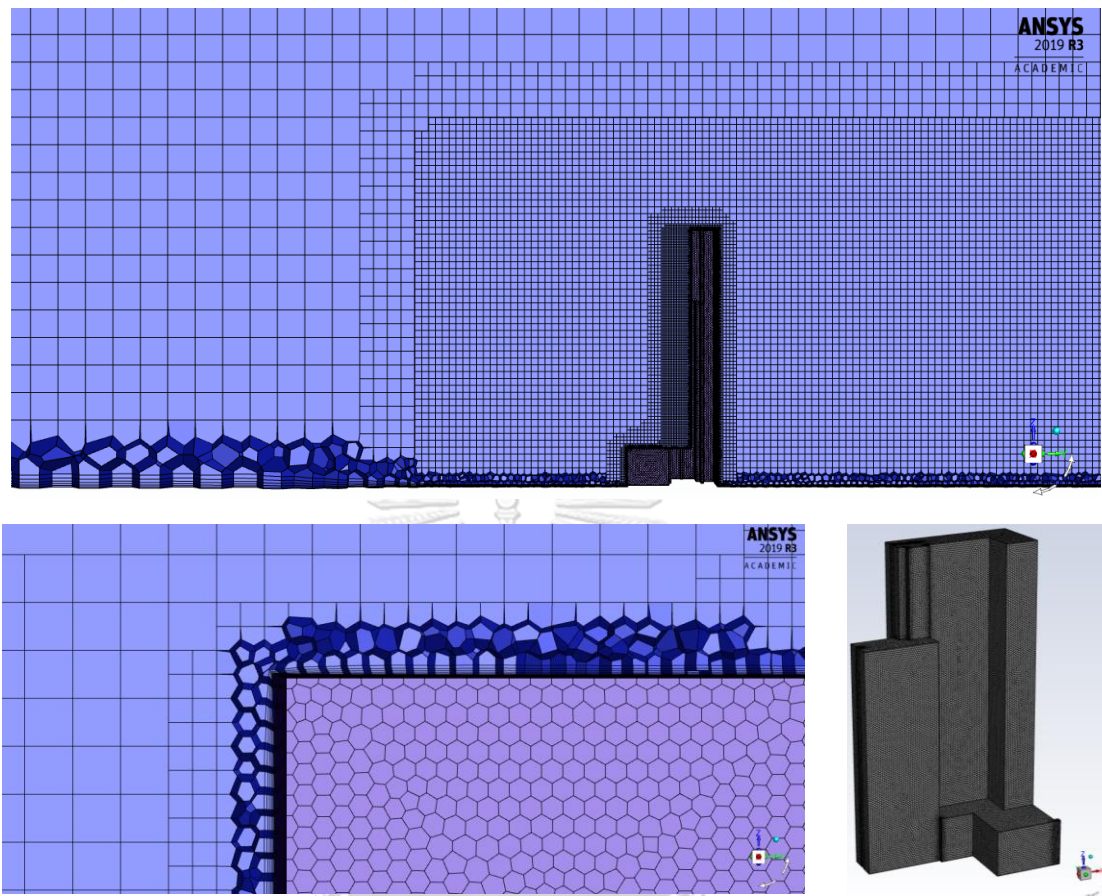
Figure 4-9 The near-wall region mesh of isolated case

Primary building with surrounding area: SBs case mesh (5,86 million cells)

The mesh of primary building with the neighbor area differs basically with the isolated case in the appearance of surrounding buildings. That required a high-solution mesh to capture all flow characteristics in this neighbor area. Additionally, like the primary school and the ground, all walls of surrounding buildings are also treated as no-slip walls and were refined by high-solution poly-prism layers as below pictures.
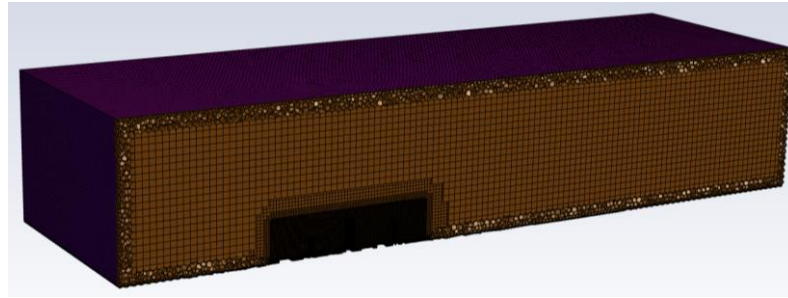
Figure 4-10 SBs case mesh
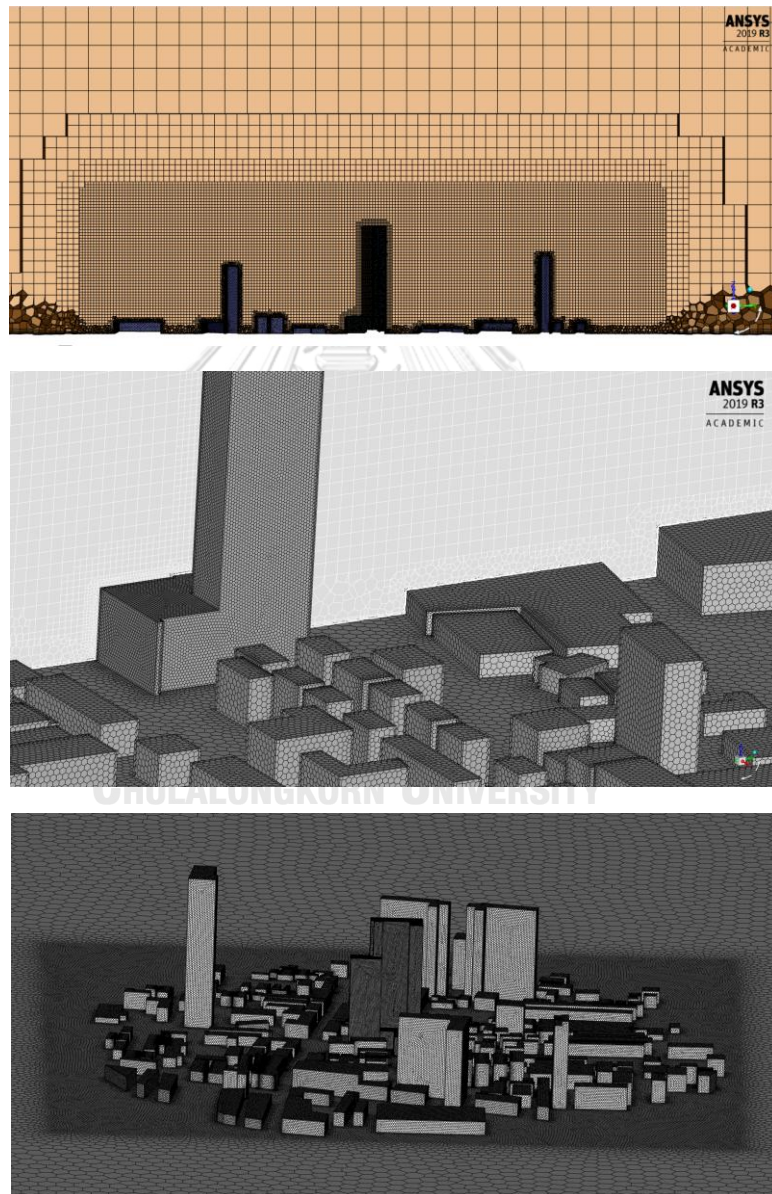
Figure 4-11 SBs case mesh detailed views

4.5 Model set-up

4.5.1 Boundary conditions

The computational domain includes one inlet, one outlet, one no-slip wall bottom surface (ground), and the last three surfaces are symmetry boundaries. The primary and surrounding building's walls were as no-slip wall boundaries.

Velocity Inlet

The most crucial CFD purpose arms to re-perform natural wind flow characteristics; it means that CFD regenerates the atmosphere boundary layer (ABL), which is the lowest layer of the troposphere that is in contact directly with the earth surface. In the ABL layer, the wind speed is affected by height, temperature (rate average - 1°C/100 m for ABL), and the area properties. The wind speed in ABL is changing as the gradient parameter. The maximum wind speed occurs at the top of ABL and almost be constant above this layer (Planetary Boundary Layer – PBL in Figure 4-13). In the ABL, the change of velocity follows two famous wind speed laws, and those are "power law" and "logarithmic law."
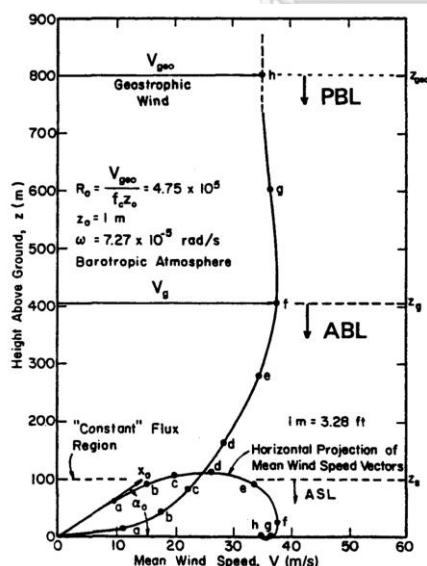
FIGURE C2.1. *Planetary Boundary Layer Example According to Model of Lett*
(1962).

TABLE C2.2. ABL Characteristics

Class	Terrain Description	(z_0) (m)[a]	$(1/\alpha)$[b]	$I_u(\%)$[c]	Exposure[d]	z_g (m)
1	Open sea, fetch at least 5 km	0.0002	0.10	9.2	D	215
2	Mud flats, snow; no vegeta-tion, no obstacles	0.005	0.13	13.2		
3	Open flat terrain; grass, few isolated obstacles	0.03	0.15	17.2	C	275
4	Low crops; occasional large obstacles, $x'/h > 20$	0.10	0.18	21.7		
5	High crops; scattered obsta-cles, residential suburbs, $15 < x'/h < 20$	0.25	0.22	27.1	B	370
6	Parkland, bushes; numerous obstacles, $x'/h \sim 10$	0.5	0.29	33.4		
7	Regular large obstacle cover-age (dense spacing of low buildings, forest)	1.0–2.0	0.33	43.4	A	460
8	City center with high- and low-rise buildings	≥ 2	0.40~ 0.67	—		

[a] Regional roughness lengths from Wieringa (1992).
[b] Power-law exponents from Davenport (1960).
[c] Turbulence intensities for FUR terrain ($z = 10$ m) according to (C2.6)
[d] Exposure categories and gradient heights from ASCE 7–95.

Figure 4-12 The ABL and PBL characteristics described in ASCE Manual of Practice No. 67 (1999)
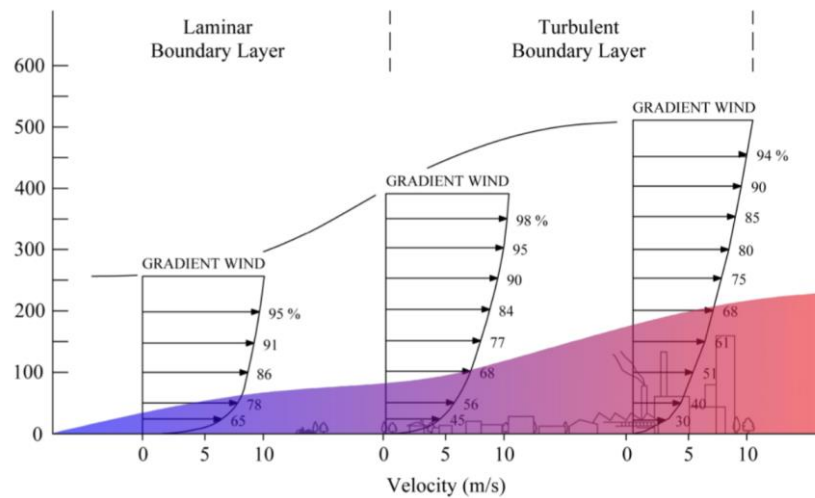
Figure 4-13 The wind speed gradient at different areas in ABL (Daemei, 2019)

The vertical velocity profile $U(z)$ of an urban area given by "power law" in ASCE MANUAL OF PRACTICE NO. 67 (1999) and ASCE (2005) was adopted to generate the wind speed gradient in ABL, with an attempt to match the wind characteristics in WTT. The profile $U(z)$ is defined as

$$U(z) = U(z_g) \left(\frac{z}{z_g} \right)^{1/\alpha}$$

(4-1)

where

$z_g = 460\,m$ is the *gradient* height (the ABL thickness),

$1/\alpha = 0.33$ is an empirical exponent, and

$U(z)$ & $U(z_g)$ are velocities at the height z and z_g, respectively.

Figure 4-14 illustrated the wind speed profile between CFD simulation and WTT. Both were normalized by 10.98m/s, which is the wind speed at the top of WTT. While it is 7.58m/s at the top of the building (Boonyapinyo et al., 2016). Hence, the velocity formula in equation (4-1) yield to

$$U(z) = 10.9837 \left(\frac{z}{1.15} \right)^{0.33} [m/s]$$

(4-2)
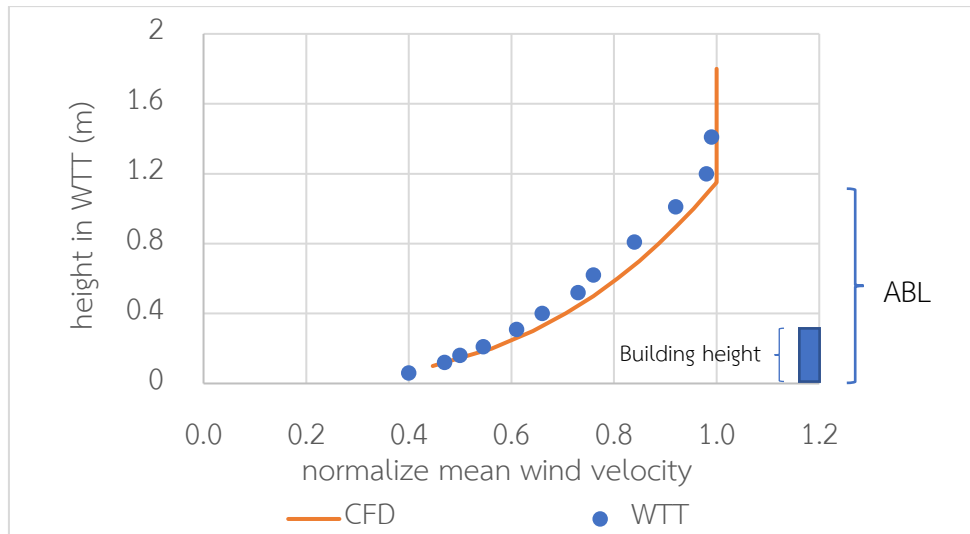
Figure 4-14 Wind velocity profile in CFD and WTT

(Primary building height is 0.375m at 1/400 ratio scale down)

Moreover, under the effects of these above elements, the wind speed in ABL is still heterogeneous (turbulent). Turbulent intensity (as often referred to as turbulent level) is defined as the ratio of root-mean-square of velocity fluctuation & mean flow velocity, and it represents the intensity of wind velocity fluctuation (Fluent, 2013).

$$I = \frac{u'}{U} = \frac{\sqrt{\frac{1}{3}(u_x'^2 + u_y'^2 + u_z'^2)}}{\sqrt{U_x^2 + U_y^2 + U_z^2}} \qquad (4\text{-}3)$$

where I is the turbulent intensity, u' is the root-mean-square velocity and U is the mean flow velocity, and subscripts x, y & z stands for three main directions.

In ASCE Manual of Practice No. 67 (1999) and ASCE (2005), the longitudinal turbulent intensity defined as

$$I = \frac{1}{\ln\left(\frac{z}{z_0}\right)} \qquad (4\text{-}4)$$

where z_0 is the aerodynamic surface-roughness length.

The wind speed gradient and turbulence intensity are the initial inputs for the inlet boundary condition (Figure 4-16). However, the turbulence intensity in simulation

cannot be adopted by an equation like equation (4-4) in simulation (Figure 4-15), especially in ANSYS Fluent.
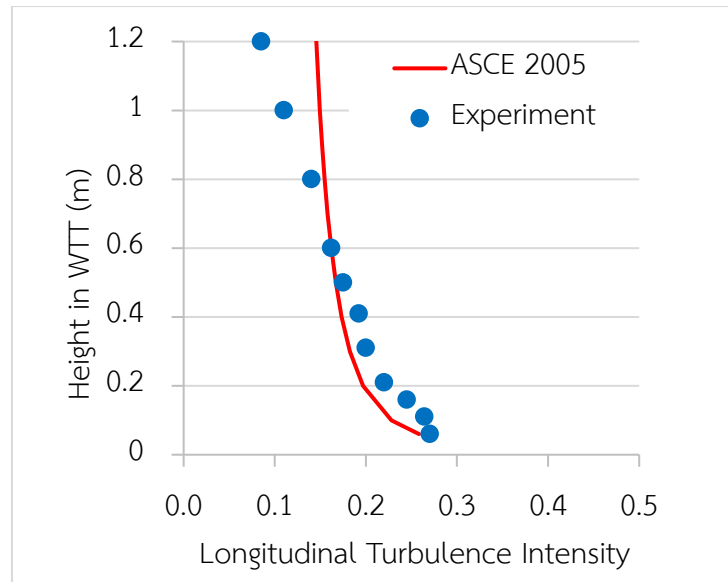
Figure 4-15 Longitudinal turbulence intensity in CFD and WTT

Hence, the turbulent initial properties would be set base on the concept "Intensity and Hydraulic Diameter" (as an option in ANSYS Fluent). The Turbulent intensity (%) was assumed at 15% (this took the average of turbulent intensity from WTT results, and though the process, it solved a good match with wind flow characteristics in WTT). While Hydraulic Diameter was calculated as

$$D = \frac{2ab}{a+b} \tag{4-5}$$

where a and b are the sizes of the rectangular inlet. The inlet size is 5.75 x 1.875 m^2, so the Hydraulic Diameter is 2.828 meters.
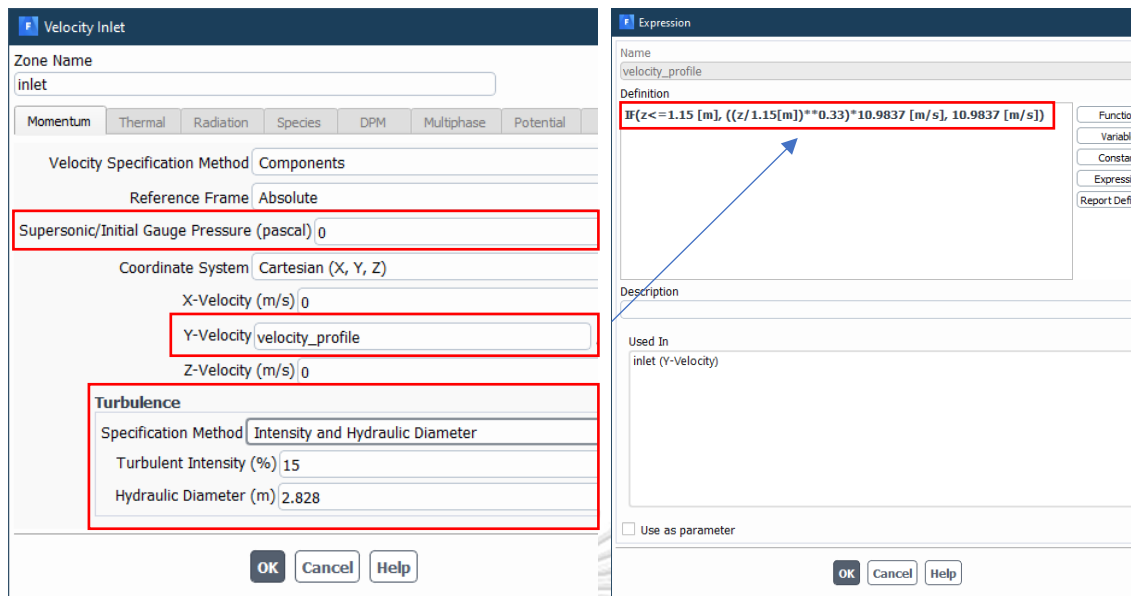
Figure 4-16 The velocity inlet boundary input (ANSYS Fluent ver. 2019R2)

Pressure outlet

The outlet (or pressure outlet) is set up with zero Gauge pressure (same with inlet Gauge pressure), which means no "backflow" pressure affects the flow inside of the domain. This guarantee wind flows locally with balanced pressure condition.
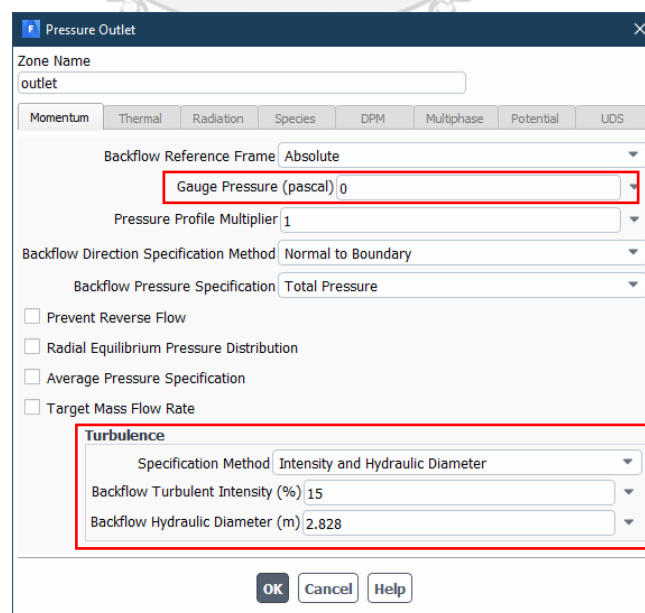
Figure 4-17 The pressure outlet boundary condition in ANSYS Fluent

4.5.2 Material properties

The airflow is considered as an incompressible flow with density at 1.2 kg/m^3, which is taken the density measured in WTT (Boonyapinyo et al., 2016). The air viscosity is 1.7894x10^{-5} kg/m-s, and all properties in the computational domain are homogeneous.

4.5.3 Viscous model

For the simulation case (steady-state) uses the $k-\omega-SST$ turbulence model, all the equations and constants would be kept as default values of ANSYS Fluent, which were discussed in 2.3.4.
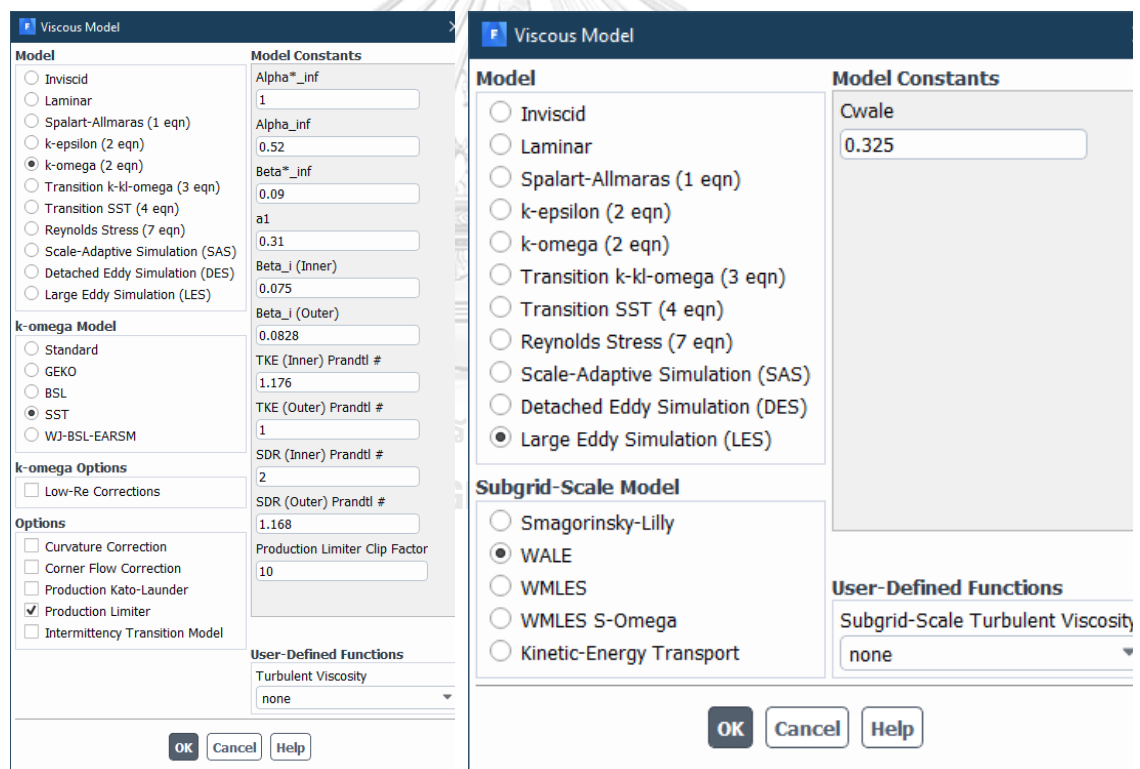
Figure 4-18 The $k-\omega-SST$ turbulence model and Large Eddy Simulation properties in ANSYS Fluent

While LES (transition state simulation) used the result of the *SST case*, which means the data of the domain after solving by $k-\omega-SST$ will be transferred to be an

initial condition for LES. ANSYS Fluent supports this process automatically without any setting more. The Subgrid-Scale model used WALE.

The simulation used the second-order upwind scheme for momentum, turbulence kinetic energy, specific dissipation rate, and pressure (Dagnew and Bitsuamlak, 2013). For the pressure-velocity coupling, the semi-implicit method for pressure linked equations-consistent (SIMPLEC) algorithm was used with skewness correction equal to 1 (ANSYS, 2016). A strict convergence condition of 10^{-6} was applied to all residuals. In the transient simulation of LES, computational time step size Δt = 0.002 sec, and when the solution reached a stable state (often as a periodic state), the data would be sampled.

4.6 Solution process

The CFD code would discretize the Navier-Stokes equations and solves them over the computational fluid domain with the aid of the initial boundary conditions. In solving progress, the residuals of any variables need to be observed clearly. When all the residuals satisfy selective tolerance, the solving will stop to provide a convergent solution. However, convergence occurs in two cases. One, all the variable's residuals drop under tolerance values; the other happens when residuals cannot drop lower (*). In other words, the solution keeps being solved, and the residuals are getting stable or periodic. In the case of wind load simulation, the vortex in the back of the building is generated periodically (vortexes will be generated by the most significant kinetic energy, dissipated into smaller ones and repeating endlessly). This made the errors unstable periodically. Figure 4-19 showed that when the residuals of the dissipation omega cannot be reduced more, these other residuals start periodically.

(*) This case is different from the bad-meshing cases, which lead to the wrong solution.
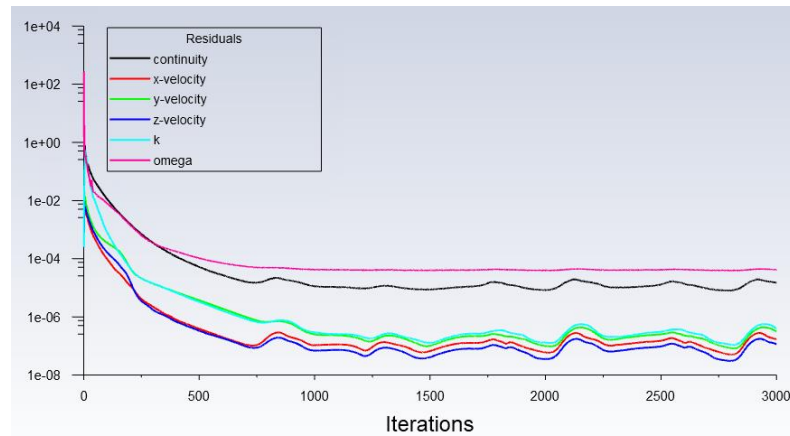
Figure 4-19 Residuals of variables in SST-SBs case

A transient solving like LES provides the results as time-dependent data. Depending on the purpose, users can go with it or averaged one. In the next section, the comparisons with WTT and RANS solution will be on the time-averaged terms (such as pressure coefficients (C_p) and velocity magnitude). Thus, the LES solution needs to be averaged through the time-solving.

Figure 4-21 presented how changeable of instantaneous C_p values compared to time-average ones. They are different because of the change of flow state in the domain at every moment. However, it is periodic because the development & dissipation of the flow *goes on and on* (energy metabolism) in the domain. That means LES needs to solve the flow through a few periods (at least) before averaging to stable the mean solution. The stable solution is considered as the state of the full development of the flow inside the domain. It includes the creation of a vortex, its energy decline, breaking down to smaller eddies, and total disappearance; then, all above would be re-generated as a periodic flow. In other words, the solving was keep continuously run until the average teams were getting stable (Figure 4-21). On top of that, the average data did not start in the beginning. It began to sampling data (averaging – sampling is as a function of ANSYS Fluent) after *1.2 seconds* running

because the flow needs time to stabilize when moving from RANS initial conditions to LES solving.
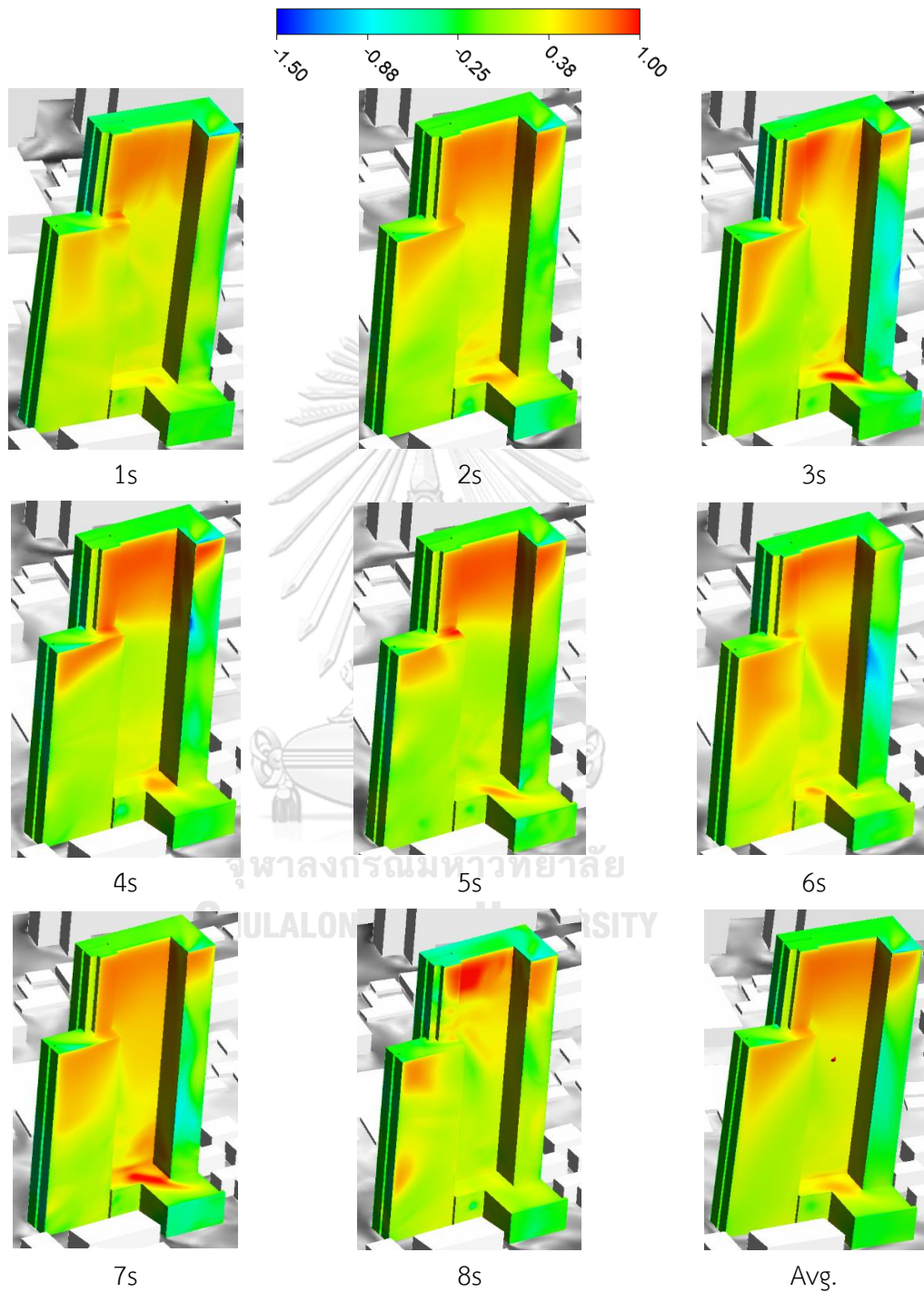
Figure 4-20 Pressure coefficient contour maps in LES-SBs case for wind direction 270°

Tracking point

Starting sampling
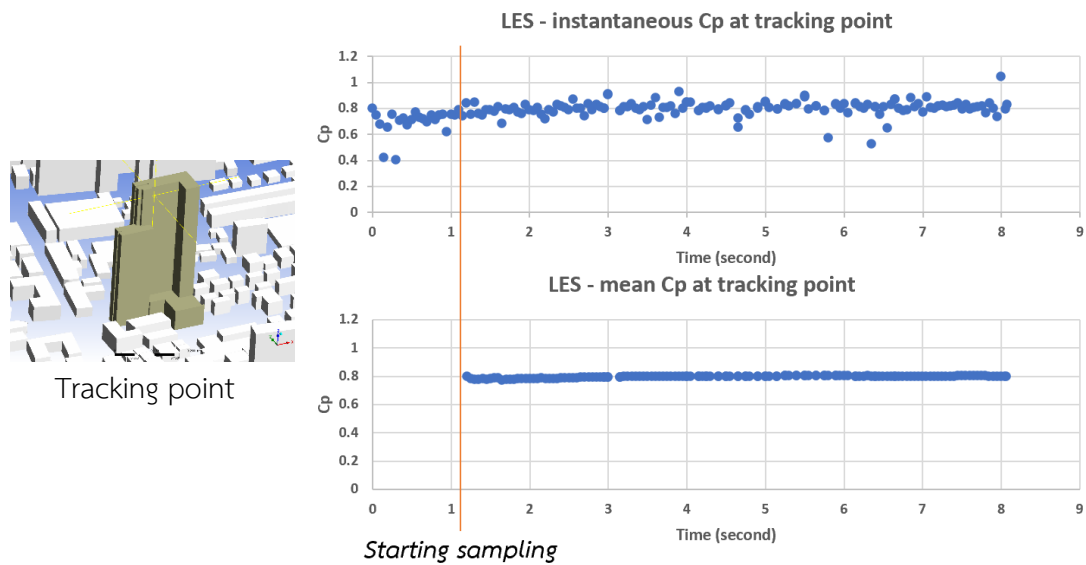
Figure 4-21 Pressure coefficient at a tracking point on primary building in LES–isolated case.

4.7 Post-processing

The data from the previous step, such as velocity flow fields, vorticity, and pressures, will be analyzed and extracted on lines, planes, and so on to perform the solution. The program in use was ANSYS Result (in the old version of ANSYS, it was named CFD Post), which is a subprogram ANSYS, Inc. provided to read and perform CFD data. In this study, only the processed data will be used in the next chapters; the practical steps of post-processing will not be mentioned.

CHAPTER 5

INFLUENCES OF SURROUNDING BUILDINGS ON WIND LOADS

OF THE TARGET STRUCTURE

To study the influence of surrounding buildings (SBs) on wind loads of the primary structure, we conducted two simulations with the LES approach only, which are LES-isolated case and LES-SBs case. The reason for choosing the LES approach in simulations is its transient state, which lets us observe flow characteristics easily. The only difference in the two simulations is the geometry at the input. In the LES–SBs case, it had the appearance of a 400m radius neighbor area (with different height buildings (Figure 5-1). While other elements and conditions such as domain size, meshing, boundary conditions, wind direction, simulation setup properties are identical with LES–isolated case. By presenting flow patterns (streamlines pattern) and the pressure distribution on the cladding surfaces (through pressure coefficients on the primary building), this study would indicate the importance of SBs in CFD simulation.

       a. LES–isolated case   *b.* LES–SBs case
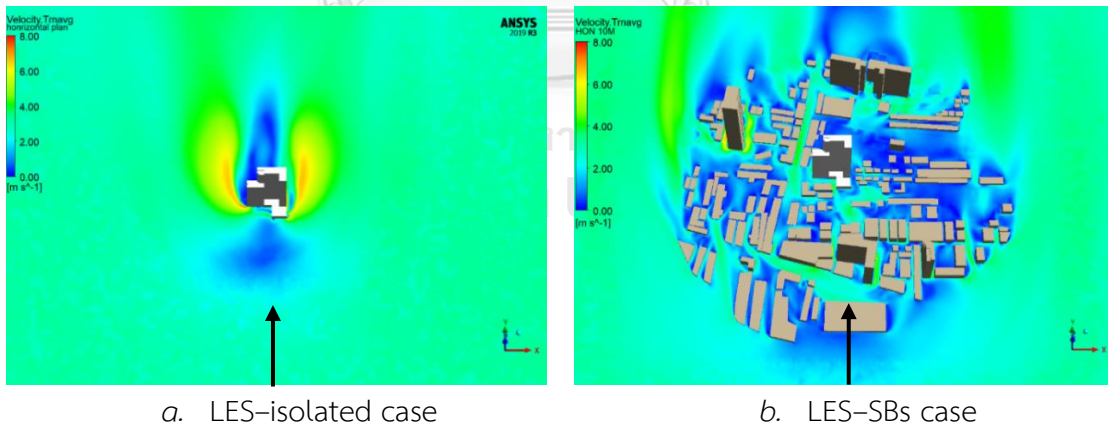
Figure 5-1 Mean velocity contour map at 10m from ground

Influences of surrounding buildings on wind loads of the primary structure

5.1 Wind flow pattern

5.1.1 Isolated case

Beranek (1980) conducted wind tunnel tests with sand-erosion and oil-film techniques to visualize a single rectangle building's flow pattern. His study of flow patterns (Figure 5-2) would give the architects and building engineers a practical model to judge the air environment without using wind tunnel tests. Its value has been maintained until nowadays in the building concept design.
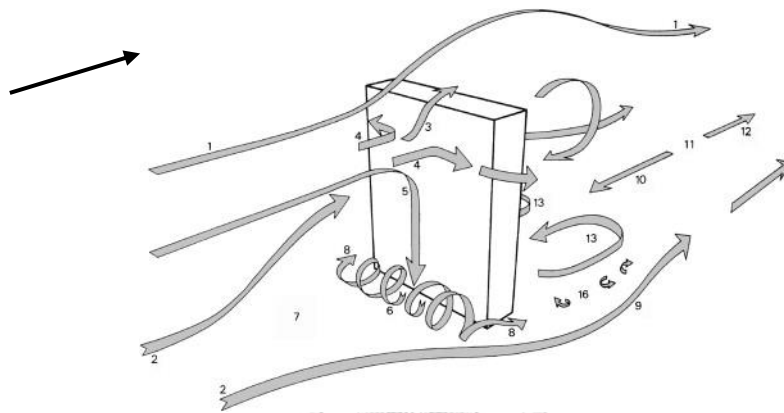
Figure 5-2 Schematic representation of wind flow pattern around a rectangular building (Beranek, 1980)

Under the CFD simulation aid, the streamline patterns are now supported natively in ANSYS Fluent to visualize the air interactions around the building/urban area. In this study, to observe the flow patterns around the primary building, two streamline patterns were created by ANSYS Fluent (Figure 5-3). Even the building's shape is not usual rectangular; however, wind regime can be distinguished that:

a) The airflow separated at building corners; then, its speed will be accelerated. This phenomenon can be observed easily at roof corners, and both side edges of the primary building.

b) At around 2/3 height of the primary building, after the impacting between wind flow and the building, on the windward surface, the flow tends to separate into two directions:

- A part transports upward, and velocity magnitude intensification occurred (corner effect), which caused the change of pressure around the building. The top of the building will become a high-pressure area, while it is a low-pressure area in the building's leeward side. That turns the leeward side to be a suction area, which sucks the airflow into it (from the top and around the building) to creates the giant eddy here. The flow transported through two lateral sides is sucked in this eddy simultaneously.
- The rest part of the airflow on the windward surface is extent transported downwards (downdraft effect), causing energetic vortexes in the low level of the windward side, right in the front of the building.
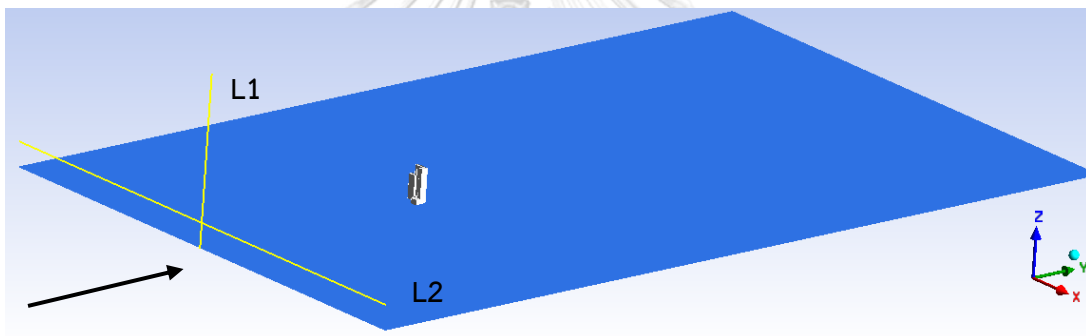
a. Line L1 (x=0, y=-2.875, z=[0, 1.875]) &
Line L2 (x=[-2.875, 2.875], y=-2.875, z=0.25)

b. Streamlines from L1

c. Streamlines from L2

0.00   2.77   5.54   8.31   11.08
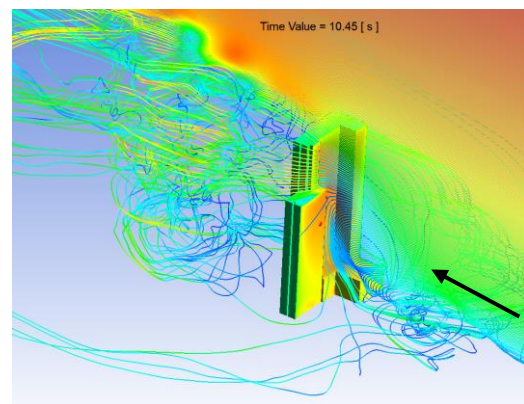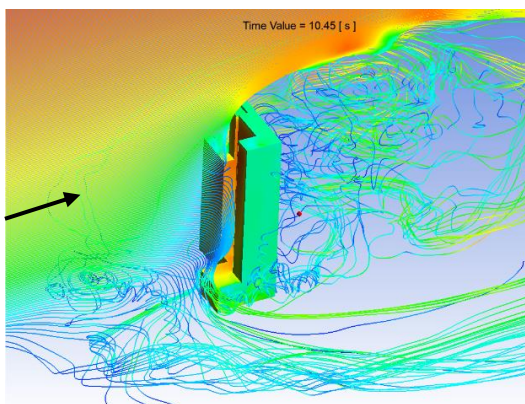
[m s^-1]
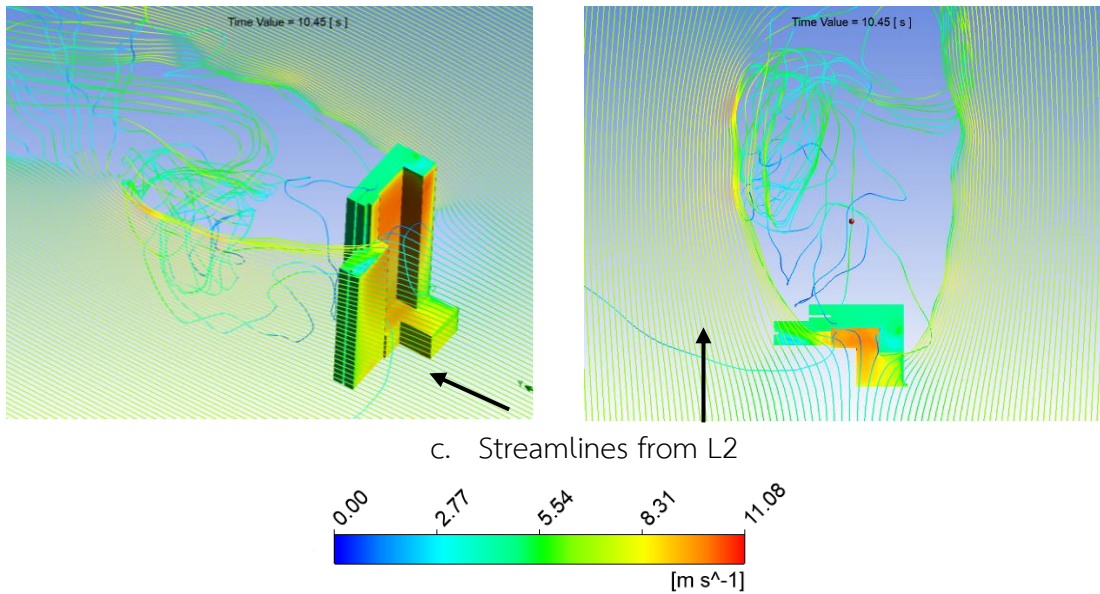
Figure 5-3 Flow pattern around the primary building at 10.45s (LES–isolated case)

Figure 5-3 illustrated the wind flow pattern of the LES-isolated case by streamlines in ANSYS Fluent. One starts from the vertical line (L1), which is in the center of the inlet. The second is the horizontal line (L2), which locates at 100m from the ground. In the 1:400 scaled simulation, the coordinates of the two straight lines are: L1 (x=0, y=-2.875, z= [0, 1.875]) and L2 (x= [-2.875, 2.875], y=-2.875, z=0.25), respectively.

5.1.2 With surrounding buildings (SBs) case

Figure 5-5 presents the streamline pattern, which starts from line L3 and line L4 in LES-SBs case with different views (the same way of L1 and L2 in 5.1.1). Generally, adding surrounding buildings in a simulation will bring the authenticity of the natural flow re-generation. It rarely has an urban area on the earth under low building density nowadays. When the flow comes through a high-density building area, its characteristics (such as direction, speed, and turbulent intensity) will be affected by many elements, especially by two effects:

a. Venturi effect (Figure 5-4a)

Venturi effect is a well-known physic phenomenon when the flow comes into a constricted area, the speed will be accelerated, and the pressure in that area will be drop.

b. Corner effect - flow separation at the building corner (Figure 5-4b)

The pressure differences between in front of the building (high pressure) with the lateral sides (low pressure) make the flow detaching itself from the surface, and a velocity intensification happens. Flow separation increases the drag coefficient to a very high level.
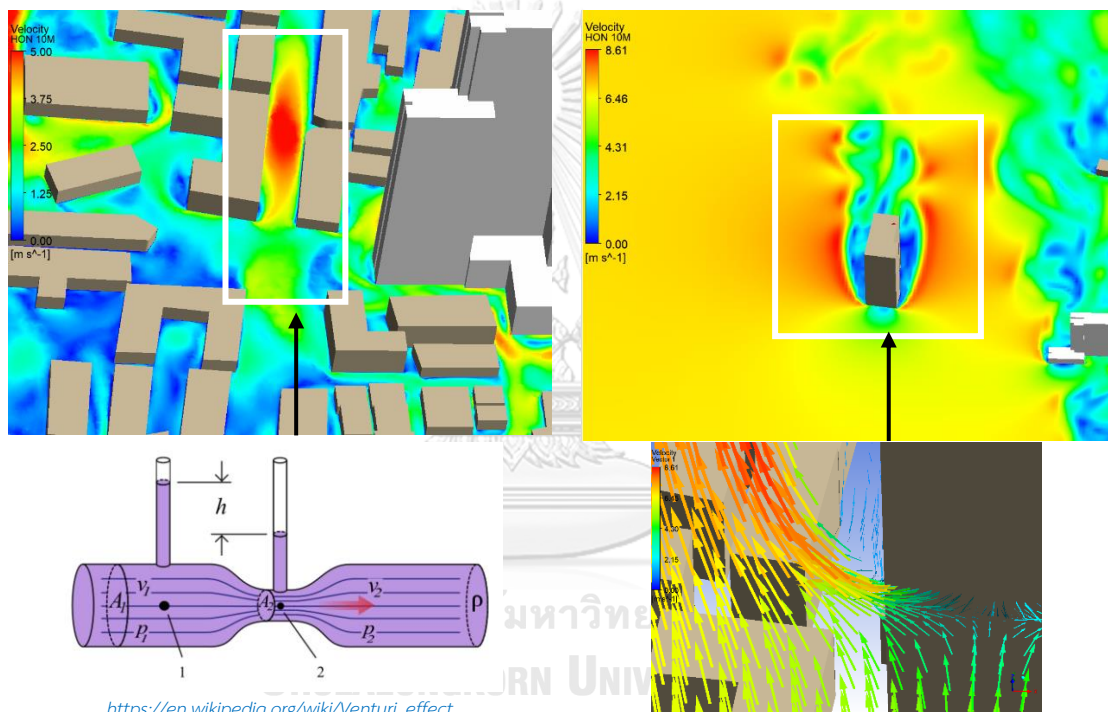
Figure 5-4 Venturi effect (left) and the flow separation at building corners (right)

When the flow starts at the inlet, it follows general rules in ABL (speed is gradually increasing from the ground, the turbulent intensity keeps a balance). When it comes to the urban area, with more complicated about topography, the flow cannot maintain its characteristics. With some specific wind direction, for example, in Figure 5-5, the impact happened with neighbor buildings (the L-shape building) before the airflow touched the primary one. A building in the neighbor area with a significant

height could get all the effects like one described in the LES–isolated case. After the flow attacks the building in the SBs area, it can bring many phenomena such as speed acceleration, direction changing, large eddy occurring in the leeward side, and high turbulent intensity at the low-level (high constructed density in this elevation). At that moment, the flow is no longer maintain its fundamental properties, which now becomes more complicated and unpredictable. All its characteristics in SBs case are unidentical with the flow in the isolated case. So, the primary building now would be affected by not only direct wind flow but also the wind environment generated by the neighbor area.
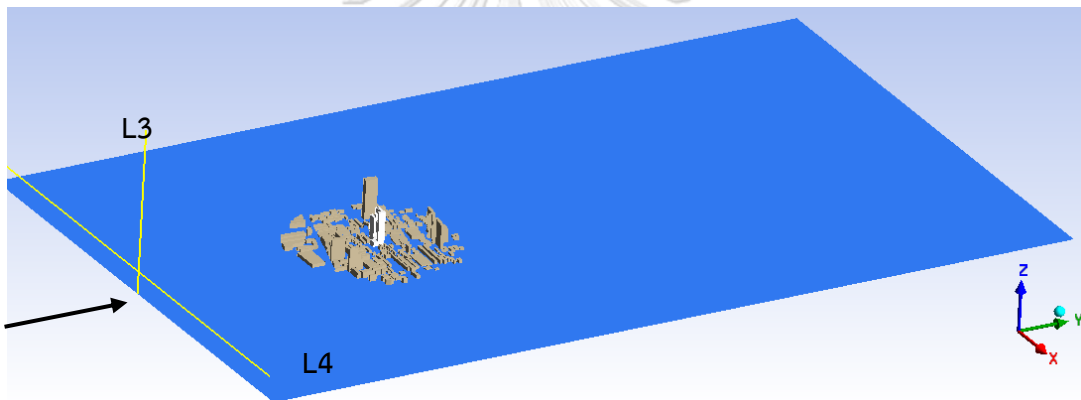
a. Line L3 (x=0, y=-2.875, z=[0, 1.875]) &
Line L4 (x=[-2.875, 2.875], y=-2.875, z=10m)

b. Streamlines from L3

c. Streamlines from L4

[m s^-1]
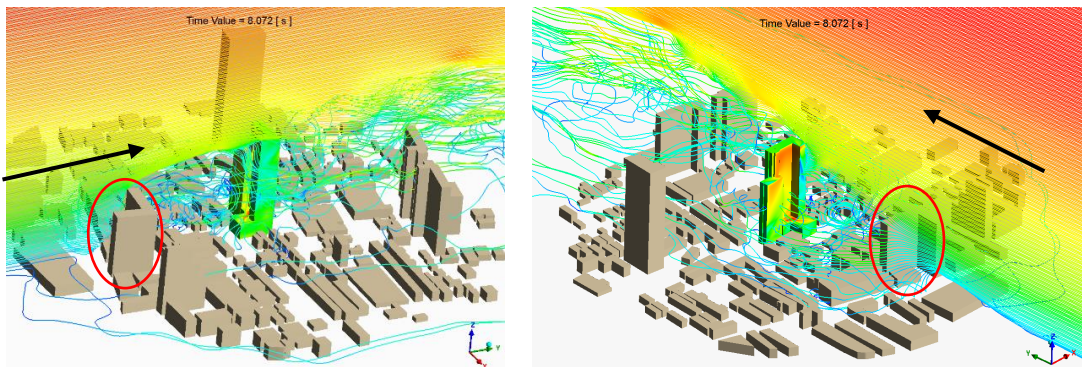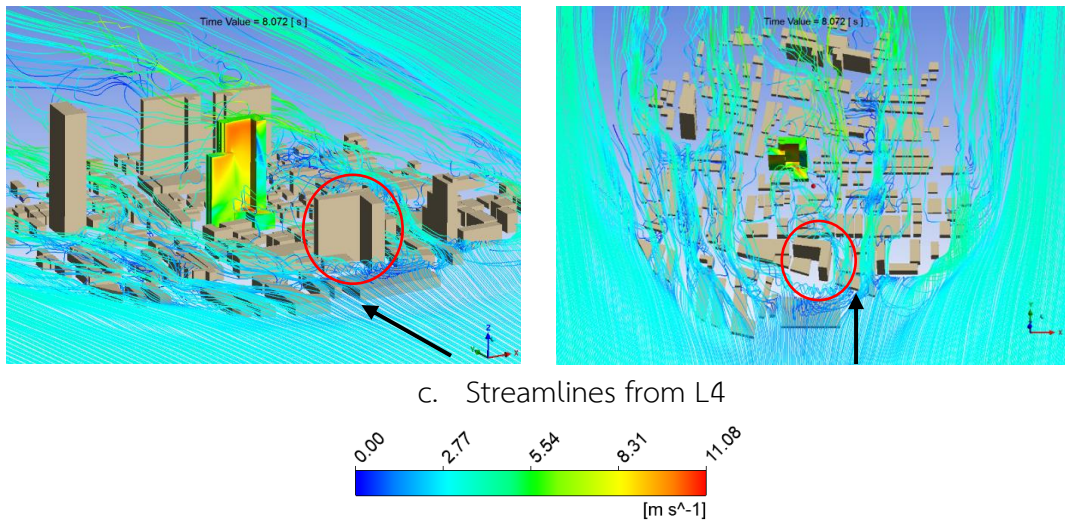
Figure 5-5 Flow pattern around the primary building at 8.07s (*LES –SBs case*)

(The building in the red circle will be mentioned as the L-shape building)

Figure 5-5 illustrated the wind flow pattern of LES-SBs case by streamlines in ANSYS Fluent. One starts from the vertical line (L3), which is in the center of the inlet. The second is the horizontal line (L4), which locates at 100m from the ground. In the 1:400 scaled simulation, the coordinates of the two straight lines are: L3 (x=0, y=-2.875, z=[0, 1.875]) and L4 (x=[-2.875, 2.875], y=-2.875, z=0.25), respectively.

5.2 Pressure coefficients

The pressure coefficient (C_p) is a dimensionless parameter applied widely in aerodynamics and hydrodynamics. C_p presents the relative of the net pressure (at the point C_p evaluated), and the fluid properties. These properties are the reference velocity (V_{ref}) and the fluid density (ρ).

$$C_p = \frac{p - p_0}{\frac{1}{2}\rho V_{ref}^2} \tag{5-1}$$

where ($p - p_0$) is the net pressure, p is the static pressure, and p_0 is the stagnant pressure. In detail, the formula (5-1) contains: V_{ref} (m/s) is the reference velocity at the building roof level, p (Pa) is the static pressure caused by wind flow at the point C_p evaluated, p_o (Pa) is the barometric pressure at a reference location, and ρ

(kg/m^3) is the air density. Noted that the simulation's barometric pressure is at zero pascal for simplifying the solving progress, ρ equals 1.2 kg/m^3, and V_{ref} at the rooftop of the primary building is 7.58 m/s, which are similar to WTT setup conditions.

Civil engineers apply C_p as a critical parameter in predicting and analyzing wind loads. The use of C_p has been published in many civil codes/building standards globally. In aerodynamics, C_p is independent of the body size but mainly effected by body shape. Consequently, engineers have measured C_p in wind tunnel tests with a scaled-down model but have been confident to predict the fluid pressure on a full-scale model.

LES-isolated case

The pressure distribution on the cladding surfaces of the building is straightforward. The windward surface had a large area dominated by positive pressure. The most considerable area pressure locates around 2/3 height of building to the top, where the wind flow attached the surface directly. Vortexes that happened at the windward side's low level were reducing this pressure magnitude in this area (Figure 5-6a). Typically, those vortexes cause negative pressure, but in this case, they are small compared to the positive pressure (by the direct wind flow attack).

The leeward surface is a suction area because of the large eddy. Few areas at the rooftop had high negative pressure because of the corner effect.

LES-SBs case

In Figure 5-5, in the wind flow direction (y-axis), the L-shape building is the biggest obstacle restricting the flow attack directly to the primary structure. The result is a large eddy generated in the L-shape building's leeward side; this eddy affected the primary structure and caused a considerable negative pressure area (suction) on the cladding surface. Figure 5-6 indicated that, in the LES–SBs case, many significant areas in the primary building's windward side are suction, which is greenfield on the

contour map (negative pressure coefficients). However, in the LES-isolated case with the same location, those areas were dominated by positive pressure.

(a) LES-isolated case   (b) LES-SBs case
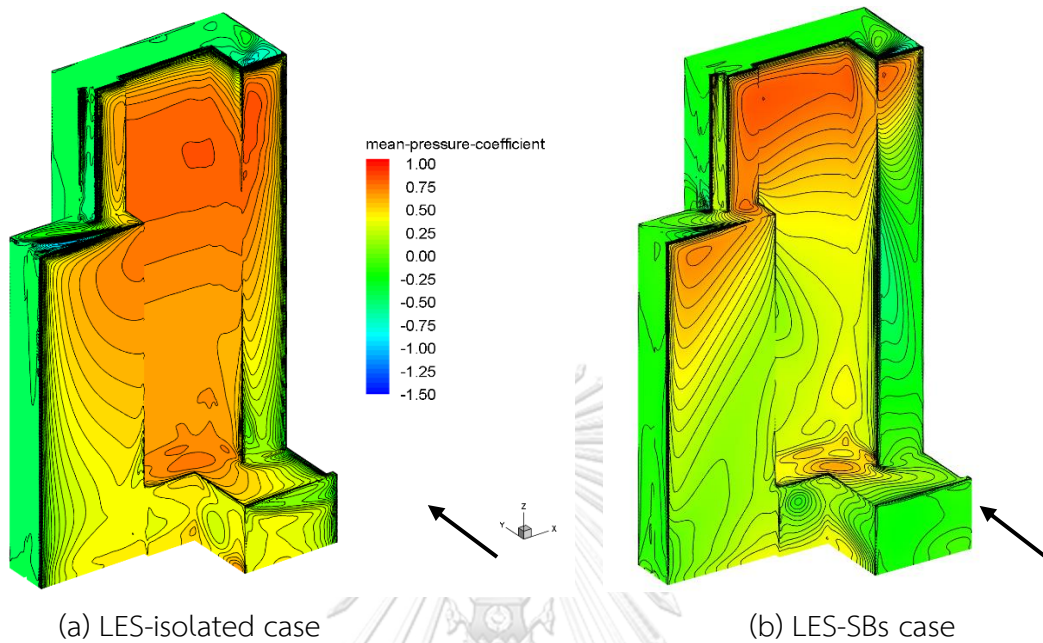
Figure 5-6 Mean pressure coefficient contour map of the primary building:
(a) LES-isolated case (b) LES–SBs case

In Figure 5-7, the comparison of pressure coefficients on two elevations (18.06m and 102.15m) of the primary building presented the influence of the SBs. Each elevation in WTT, there were 28 pressure censors installed to collect the wind pressure. The results of the experiment (WTT) & LES-SBs case stands for the wind pressure with the appearance of the SBs area, while the LES-isolated case is the simulation without the affecting of SBs. A few points of attention are as follows:

(1) At both elevations, the C_p of all positions on the windward side of LES – isolated cases are positive. Without the appearance of the SBs, the airflow impacted directly on the windward and pushed the cladding straight. Hence, most of the areas in the windward side are positive pressure in isolated

building simulation. This conclusion was proved by the negative C_p of all positions on the windward side of LES – isolated cases at both elevations.

Another observation that, in these positions, the magnitude of C_p in LES-isolated case is greater than the experiment (WTT) and LES–SBs case. The reason is the energy attenuation when the flow is traveling through buildings area before impacting the primary structure, in simulation with the appearance of SBs.

(2) At the positions 13 & 14 (at elevation 102.5m) and 10, 11 & 12 (at elevation 18.06m), there was a difference of pressure distribution. Meanwhile, the LES-isolated case kept the positive pressure trend, the experiment (WTT) & LES-SBs case dropped the pressure in this area (even they are negative at elevation 18.06m). Combining with wind flow streamlines in 5.1.2, the influence of the SBs can explain this. In LES–SBs case, the flow impacted the L-shape building (and others), then a large eddy occurred in the leeward of it, which changed the properties of the flow from pushing the surface to suck it out (Figure 5-8).

(3) The pressure distribution on the primary building's leeward side is almost identical for all cases in these two elevations.

Location of censors at elevation 102.15m

Location of censors at elevation 18.06m
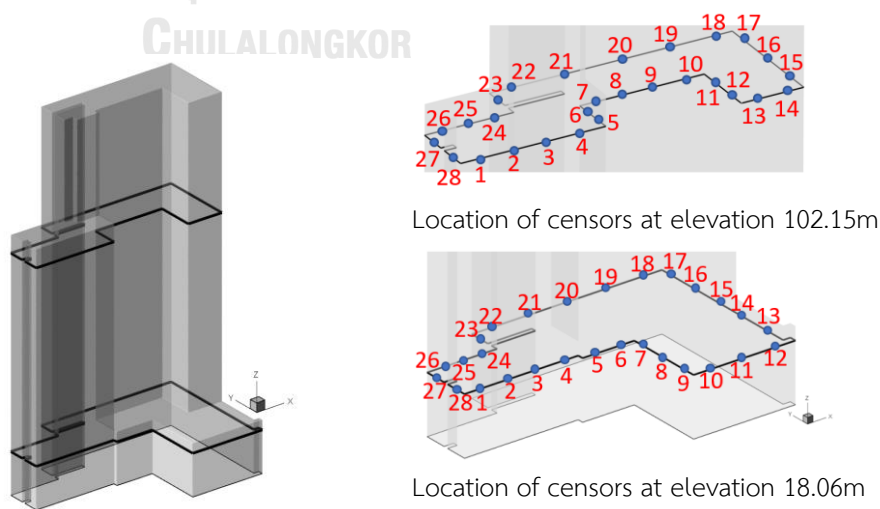
(a) Positions of the pressure sensors
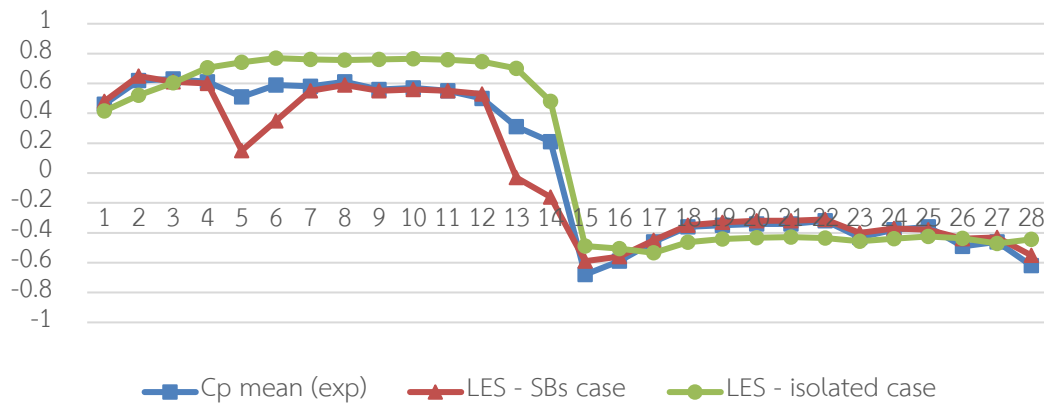
(b) Pressure coefficients plot at elevation 102.15m
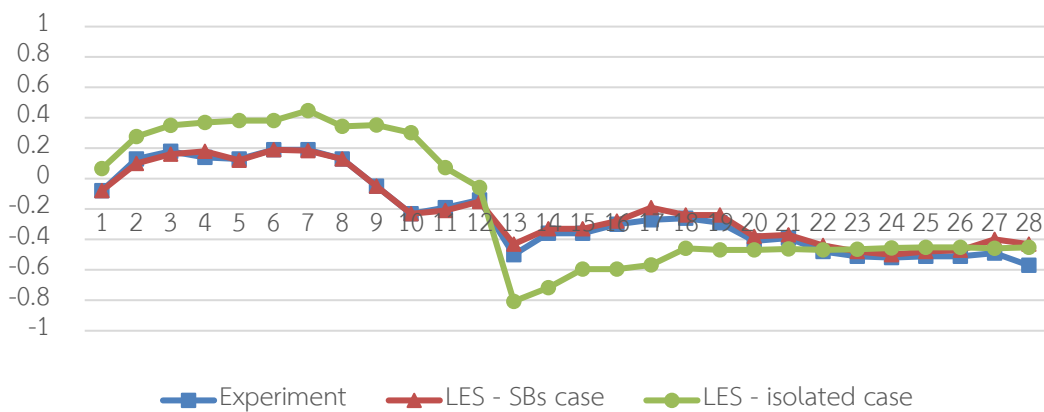
(c) Pressure coefficients plot at elevation 18.06m

Figure 5-7 The comparison of pressure coefficients at the elevation 18.06m and 102.15m of the experiment (WTT), LES-SBs case, and LES–isolated case:

(a) Positions of the pressure sensors,

(b) Pressure coefficients plot at elevation 102.15m, and

(c) Pressure coefficients plot at elevation 18.06m.
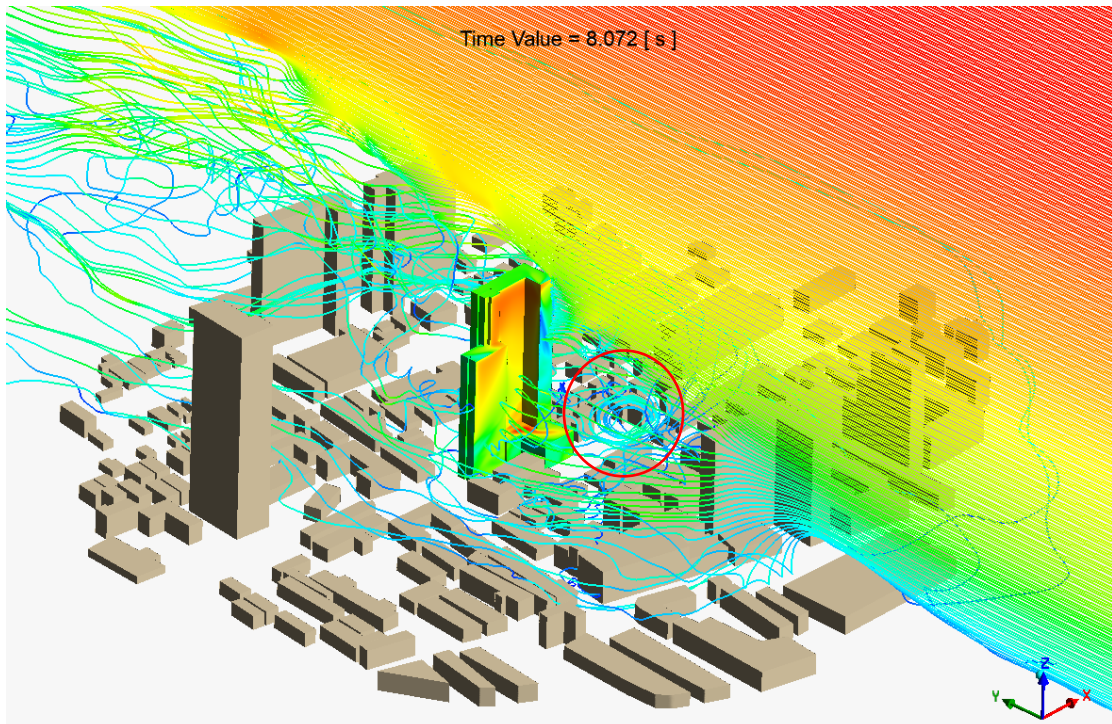
Figure 5-8 A capture of a large eddy (red circle) in LES-SBs case cause by flow
traveled through L-shape building at 8.072s

In Figure 5-9, this area was mostly received direct flows in both cases (with & without
SBs), which mean the flow straightforwardly impacted this area (without any touching
the SBs). However, the pressure on this area is not identical (up to 28% at censor
number 3). Reason came from the flow's reciprocal interaction, which affected
airflow's properties. Hence, even flowing straightly from the inlet without any
interactions with buildings in the SBs area, they can affect each other and make the
complicated wind environment.
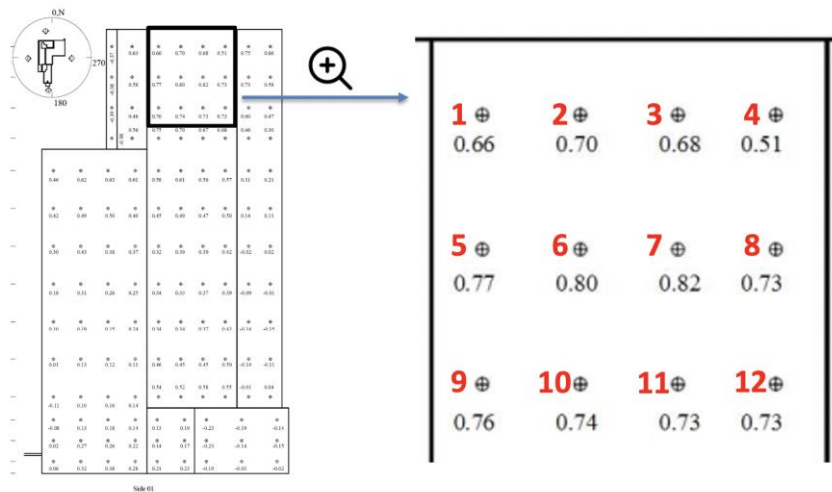
(a) Positions of the pressure sensors in WTT
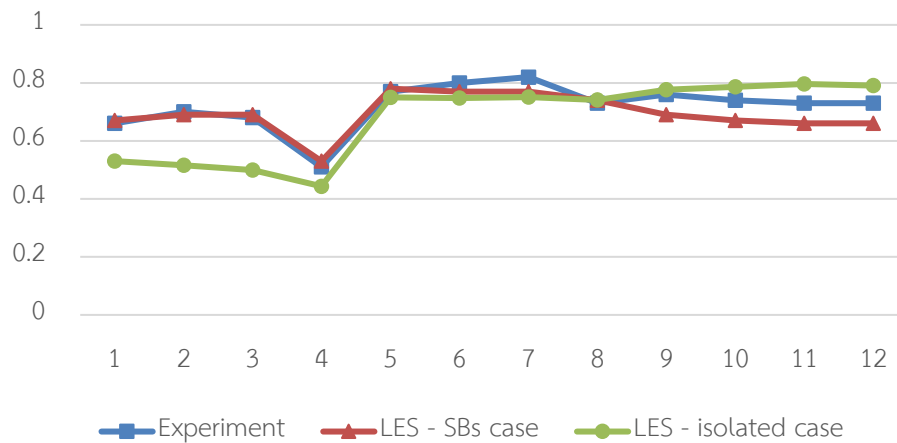
(b) Pressure coefficients plot of the positions in (a)

Figure 5-9 The comparison of pressure coefficients at the largest positive pressure area of the experiment (WTT), LES-SBs case, and LES–isolated case:

(a) Positions of the pressure sensors in WTT and

(b) Pressure coefficients plot of the positions in (a).

Figure 5-10 indicates the difference between the mean Cp distributed on the primary structure's windward surface. Note that, in the Figure 5-10c, the ratio of mean Cp in LES–isolated case (Figure 5-10a) to mean Cp in LES–SBs case (Figure 5-10b) is the best when it equals to one, while the smaller values and larger values stand for under or over estimation. The ratio in the range of 0.8 to 1.2 means the difference is

only less than 20% in two cases. The negative ratio presents the opposite of prediction in two cases (negative and positive mean Cp).

		-0.39	0.56	0.60 0.60	0.58 0.53	0.76	0.60		
		-0.46	0.58	0.76 0.76	0.76 0.75	0.83	0.62		
		-0.52	0.54	0.77 0.79	0.80 0.79	0.81	0.59		
		-0.54	0.48	0.76 0.77	0.79 0.80	0.76	0.53		
0.40	0.55	0.63	0.71	0.76 0.76	0.76 0.76	0.70	0.46		
0.39	0.60	0.67	0.70	0.71 0.71	0.71 0.72	0.63	0.40		
0.33	0.55	0.62	0.65	0.66 0.66	0.66 0.66	0.55	0.34		
0.28	0.48	0.56	0.59	0.62 0.62	0.62 0.62	0.47	0.26		
0.22	0.42	0.49	0.53	0.61 0.60	0.60 0.61	0.37	0.18		
0.16	0.35	0.42	0.46	0.64 0.64	0.64 0.65	0.20	0.06		
0.11	0.29	0.38	0.33	0.65 0.64	0.66 0.65	0.09	0.02		
0.09	0.28	0.35	0.37	0.40	0.44	0.28	0.06	-0.03	
0.11	0.33	0.37	0.36	0.35	0.39	0.32	0.35	0.19	
0.18	0.38	0.40	0.42	0.42	0.46	0.34	0.35	0.13	

(a) Mean Cp in LES–isolated case

		0.09	0.75	0.67 0.69	0.69 0.53	0.73	0.57		
		0.10	0.69	0.79 0.77	0.75 0.75	0.64	0.35		
		0.13	0.70	0.70 0.67	0.66 0.66	0.26	0.11		
		0.20	0.67	0.61 0.57	0.54 0.54	-0.03	-0.06		
0.48	0.65	0.59	0.59	0.55 0.59	0.55 0.56	-0.03	-0.16		
0.48	0.54	0.42	0.35	0.27 0.37	0.39 0.41	-0.47	-0.23		
0.47	0.41	0.35	0.17	0.14 0.24	0.33 0.36	-0.50	-0.29		
0.37	0.29	0.21	0.14	0.17 0.17	0.28 0.33	-0.43	-0.33		
0.28	0.19	0.13	0.16	0.27 0.26	0.28 0.34	-0.32	-0.31		
0.19	0.12	0.11	0.19	0.26 0.29	0.33 0.41	-0.21	-0.22		
0.12	0.08	0.13	0.20	0.39 0.36	0.38 0.39	-0.10	-0.07		
-0.08	0.11	0.16	0.17	0.12	0.19	-0.23	-0.23	-0.17	
0.01	0.09	0.17	0.22	0.06	0.08	-0.24	-0.23	-0.18	
0.01	0.12	0.22	0.28	0.22	0.27	-0.21	-0.17	-0.10	

(b) Mean Cp LES-SBs case

-4.20	0.74	0.88	0.87	0.84	1.01	1.03	1.04		
-4.88	0.83	0.96	0.99	1.01	1.00	1.29	1.78		
-4.03	0.78	1.11	1.17	1.21	1.21	3.06	5.43		
-2.70	0.72	1.25	1.37	1.47	1.47	-27.71	-9.35		
0.83	0.85	1.06	1.20	1.38	1.29	1.38	1.37	-22.58	-2.99
0.80	1.10	1.57	2.01	2.65	1.91	1.81	1.72	-1.35	-1.73
0.71	1.32	1.75	3.81	4.70	2.78	2.02	1.84	-1.10	-1.18
0.74	1.68	2.65	4.38	3.64	3.53	2.22	1.89	-1.09	-0.77
0.80	2.21	3.80	3.39	2.24	2.34	2.14	1.76	-1.14	-0.58
0.84	2.91	3.71	2.44	2.47	2.23	1.94	1.60	-0.97	-0.27
0.87	3.66	2.85	1.61	1.64	1.78	1.74	1.66	-0.87	-0.23
-1.06	2.69	2.24	2.25	3.38	2.33	-1.22	-0.27	0.21	
17.07	3.84	2.21	1.61	6.03	4.76	-1.32	-1.52	-1.06	
21.44	3.22	1.80	1.49	1.92	1.70	-1.57	-2.04	-1.39	

(c) The ratios of mean Cp in **LES-isolated** case to **LES-SBs** case   (d) Contour map of ratios in (a)

Figure 5-10 The comparison of mean Cp of LES-SBs case and LES–isolated case at the windward face of the primary building:

(a) Mean Cp in LES–isolated case,

(b) Mean Cp LES-SBs case,

(c) The ratios of mean Cp in LES–isolated case(Figure 5-10b) to mean Cp in LES-SBs case (Figure 5-10c).

Only 21 of over 129 tracking locations (16%) in the windward surface show the agreement between two cases. In comparison, the rest 108/129 (84%) illustrates a lack of accuracy in simulation without the appearance of SBs (Figure 5-11).
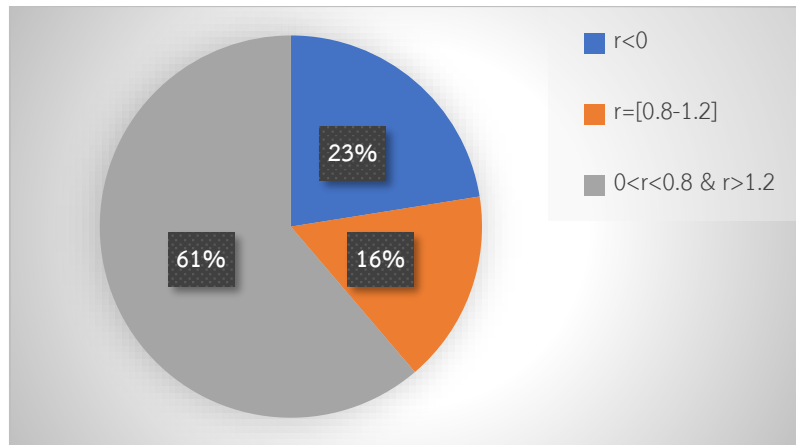
Figure 5-11 Statistical percentage of values in Figure 5-10c

In Figure 5-12, the standard deviation of the ratios in Figure 5-10c indicates that most of the ratios (68%) range from 0.98 to 2.93. And almost 50.1% of the ratios are higher than 1.95. All those statistics proved that simulation without SBs was overestimated the mean C_p compared to the case with SBs.
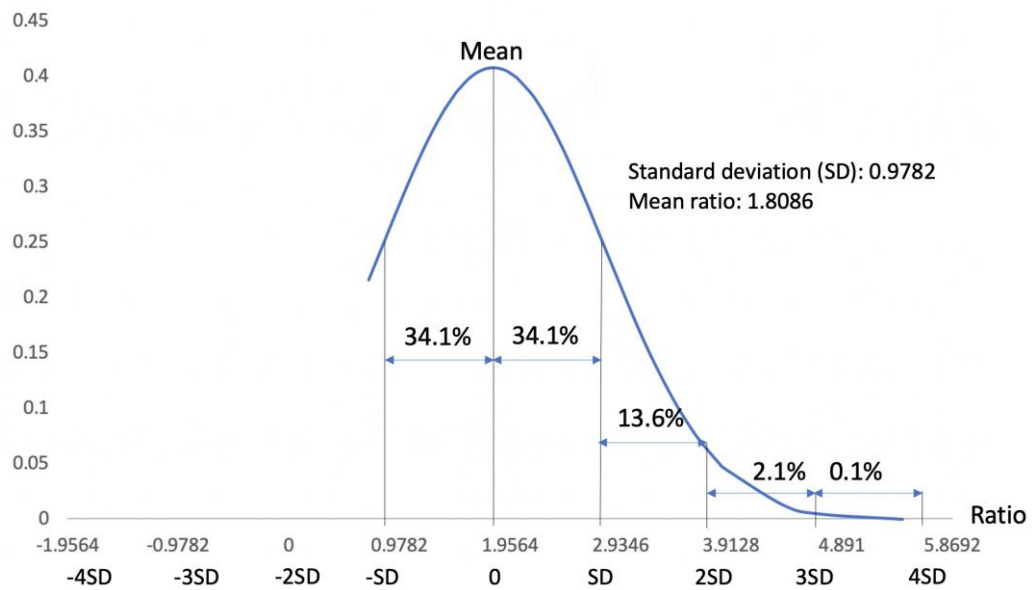
Figure 5-12 Standard deviation of the ratio in Figure 5-10c (*)

(*) The ratios were taken as the same locations where the mean Cp form WTT greater than 0.2. Because when the Cp is smaller than 0.2, the ratios calculated from this point are often significantly large, affecting the statistic's observation. Also, standard derivation calculation is only workable with the positive value; hence, all the ratios in the calculation were filtered (greater than zero).

All the above indicates that lacking SBs in simulation can lead to an inaccuracy in wind load analysis. Especially for dense building areas (high building intensity) with significant tall buildings around, the simulation without neighbor area can bring far-different results caused by differences in flow patterns. With a wind direction without any obstacles restricting the flow, the wind load can be like an isolated case. However, except the primary structure has an outstanding height comparing with others in the neighbor area, it always gets influences from the wind environment.

CHAPTER 6

ACCURACY OF CFD

In the previous section, the importance of adding SBs in simulating the primary structure was initially evident. Once again, the simulation with the neighbor area plays a vital role in re-modeling the natural wind flow. So, the results of the wind load analysis on the primary structure would approach the experiment test. Based on this acceptance, in this section, the simulation used compared to the experiment (WTT) will be only in the SBs cases. Two approach methods in CFD simulations are LES and $k-\omega-SST$ turbulence model.

In this section, the comparisons would focus on the pressure field (pressure coefficient on the primary structure), and wind velocity patterns in the air domain (computational fluid domain).

6.1 Wind velocity

As discussed in section 4.5.1, the wind velocity profile at the inlet boundary condition follows the general laws in ABL and PBL. CFD simulations aim to re-model the airflow, which targets the experiment's wind properties (WTT). Figure 6-1 presented the wind velocity at many positions in the airflow domain between two CFD simulation cases and experiments (WTT) to compare the accuracy. Note that velocity in WTT was given only at the center of the turntable table, and the data was measured without the appearance of the primary building (only SBs building).

Both of LES and SST cases were successful in re-modeling the airflow. In the term of wind speed magnitude, the CFD simulation in both LES and SST took a high agreement with experimental data (Figure 6-1). Physically, the airflow in simulation precisely followed the trend of wind in ABL (increase gradually) and PBL (constant balance), which are governed by the power law. In both cases, the velocity in ABL will be increased from 0m/s to 10.98m/s and maintain with this speed (10.98m/s) in all elevations of PBL.

For the cost-saving purpose, the simulation did not use the obstacles to generate real friction on the ground, like in WTT. In detail, the WTT uses a system of obstacles to re-model the friction, and thereby, it can transfer the laminar flow to the natural flow. Back to the CFD simulation, the vertical velocity profile and turbulent intensity at 15% were used at the inlet's boundary conditions for the same purpose (discussed section 4.5.1).
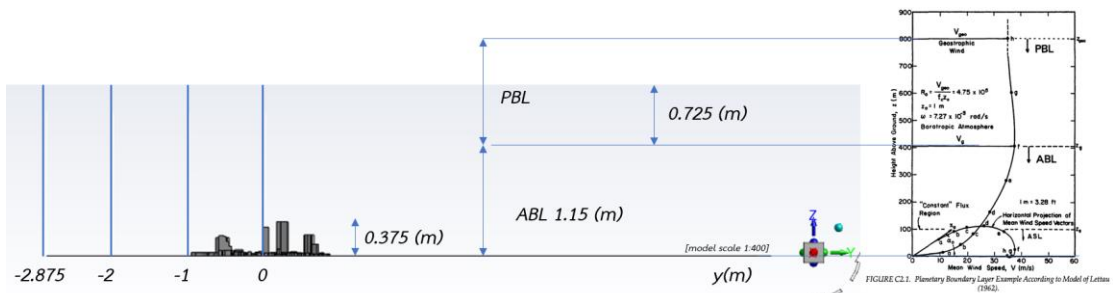
(a) Tracking line locations in airflow domain: inlet (y=-2.875), center (y=0), lines in domain (y=-2, -1)
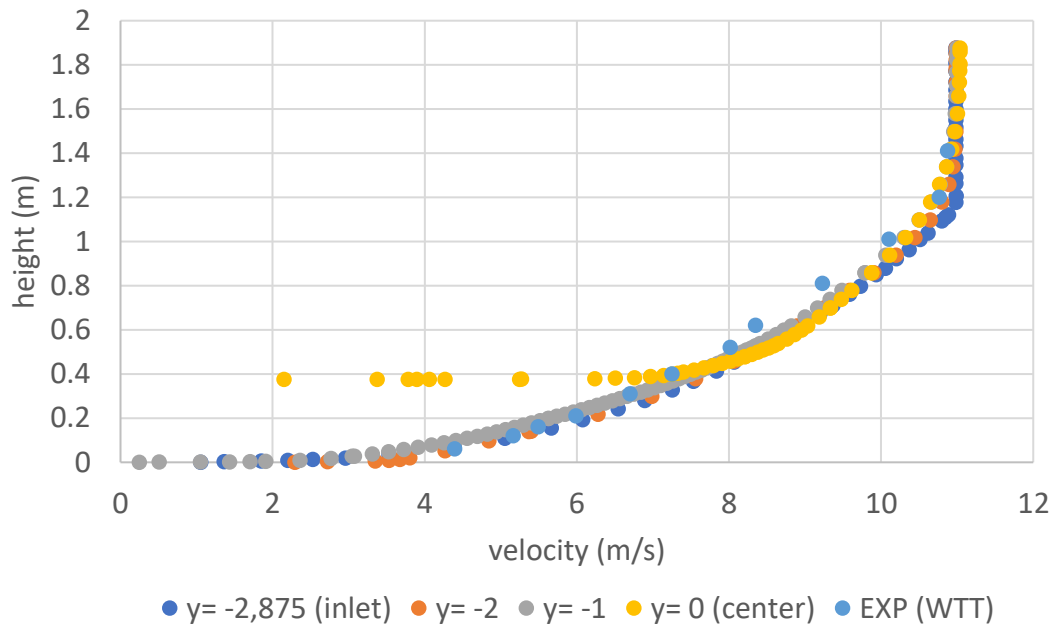
(b) Mean velocity plots of SST-SBs case & experiment (WTT)
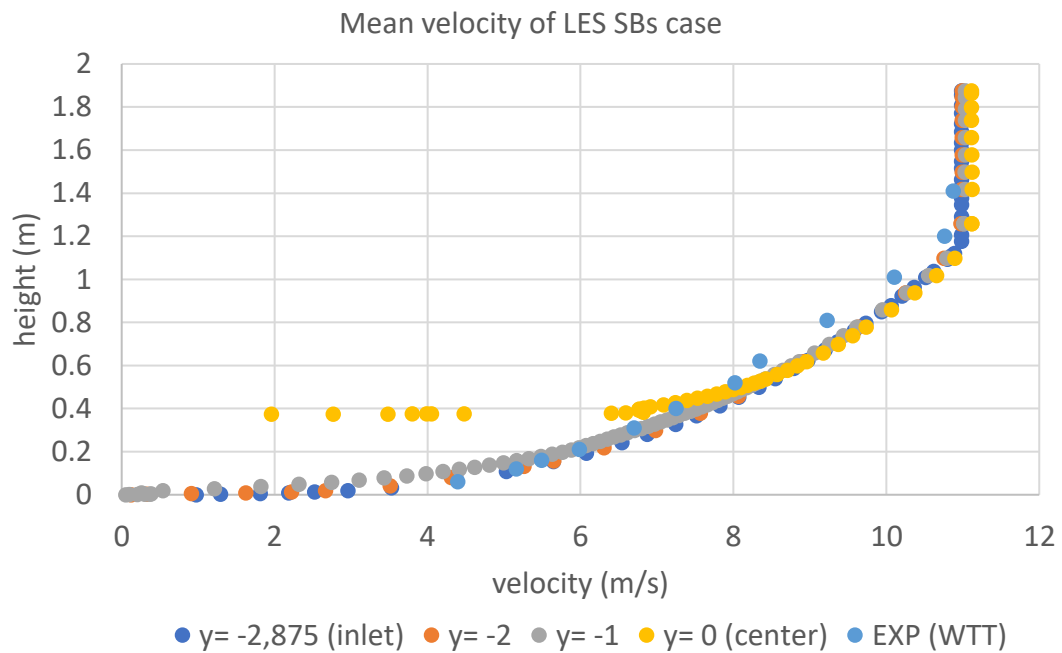
(c) Mean velocity plots of LES-SBs case & experiment (WTT).

Figure 6-1 Velocity distribution in CFD simulation and WTT (*):

(a) Tracking line locations in airflow domain: inlet (y=-2.875), center (y=0), lines in domain (y=-2, -1),

(b) Mean velocity plots of SST-SBs case & experiment (WTT), and

(c) Mean velocity plots of LES-SBs case & experiment (WTT).

(*) Note that, in the CFD simulation, at the center of the neighbor area (the line with y=0), the velocity magnitudes were just collected from the top of primary building up to the top boundary surface (z=[0.375; 1.875]); which means other values been empty because of the taking-place of the primary building at z=[0; 0.375].
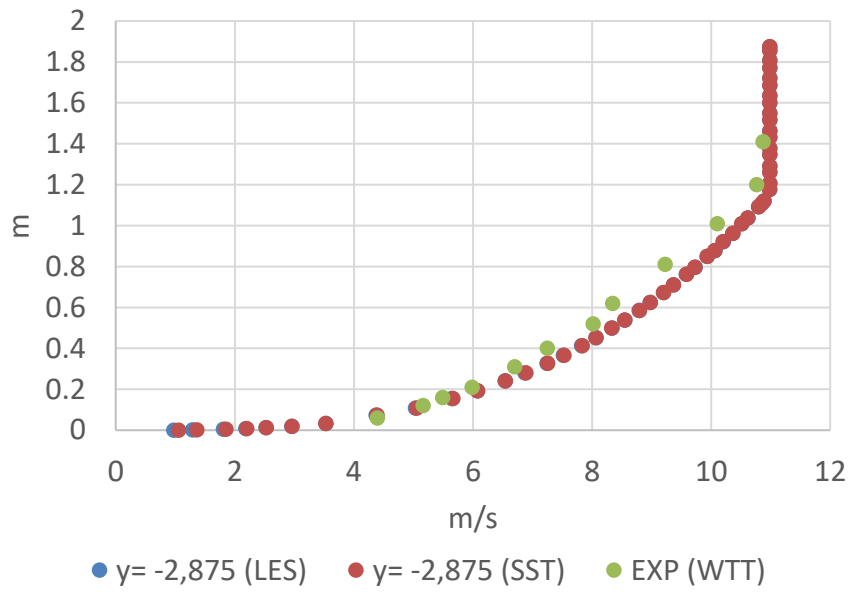
(a) y=-2.875 m (inlet)
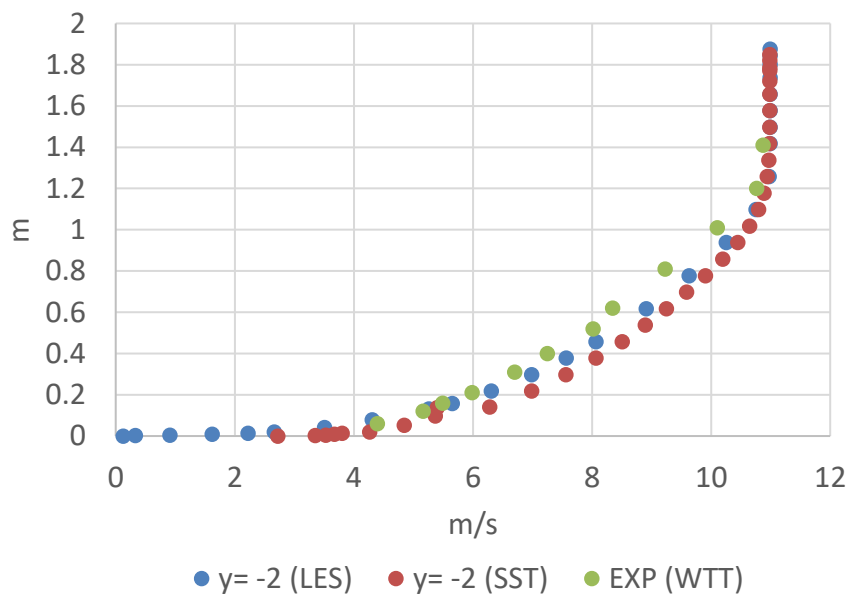
(b) y=-2.0 m
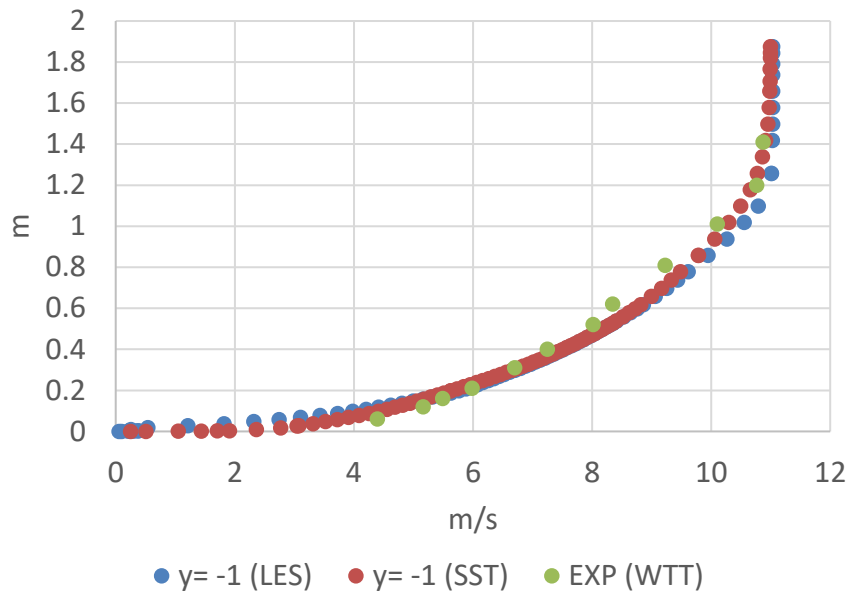
(c) y=-1.0 m
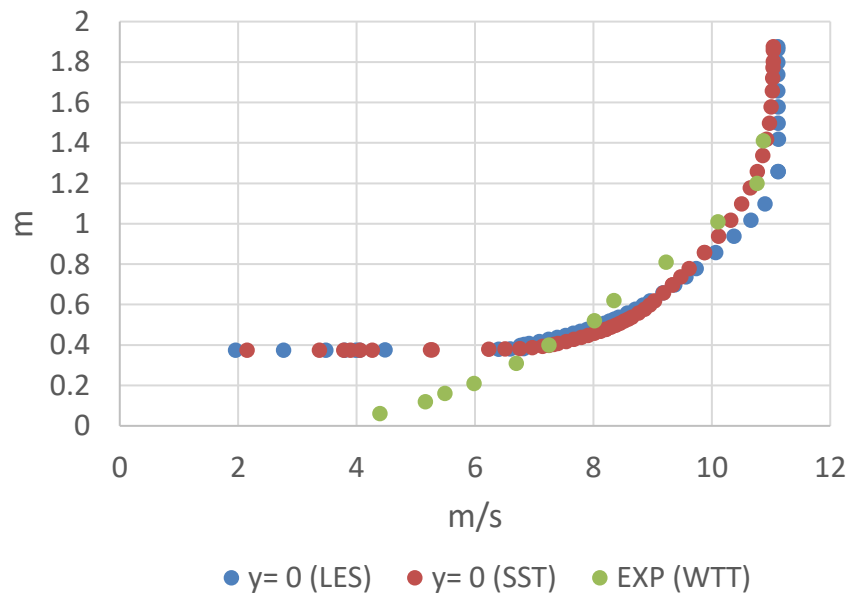
(d) y = 0 m (at the center of the primary structure)

Figure 6-2 Velocity distribution in CFD simulation and WTT at:

(a) Position of the line at y=-2.875 m (inlet),

(b) Posision of line at y=-2.0 m,

(c) Posision of line at y=-1.0 m, and

(d) Position of the line at y= 0 m (at the center of the primary structure).

LES and SST (RANS) simulations are different in the way of the mathematical approach. SST simulation based on a RANS turbulence model, which solves the mean terms and models the fluctuation. LES solves more about the flow than RANS because of its direct mathematical solving, and just an only small part which had a size smaller than grid width is modeled (sub-grid scale (SGS) eddies). With a high-resolution mesh (fine mesh), LES promises to get close to WTT's flow conditions. A transient state simulation like LES is highly recommended for studying the flow characteristics because of the time-independent flow properties. For example, the instantaneous velocity of LES and RANS are different in Figure 7-1. However, in terms of average velocity, both two methods were excellent in the remake of the wind condition compared to the experiment (Figure 6-2).

6.2 Pressure coefficients

From Figure 6-3 to Figure 6-7, the contour maps of the mean C_p on the cladding surfaces of the primary building in five main perspectives: windward (270^0), leeward (90^0), two lateral side views (0^0 & 180^0), and the top view. The LES-SBs case had a complicated wind flow characteristic in the region near the main structure (presented in section 5.1.2). For instance, even facing the wind flow direction directly, the positive pressure did not dominate the windward surface completely. On the contrary, the lower part on the right side (Figure 6-3) had a large area of negative pressure because of the large vortexes. Note that those vortexes were not only created by flowing through the primary building, but also came from the influence of SBs area.

The rest surfaces of the primary building are mainly dominated by negative pressure (suction). Wind flows through a building causes a variation of the pressure around it. For a simple rectangular building, it exists the positive pressure area right in frontal of the building, while both lateral and leeward are the low-pressure areas (negative

pressure). In the back of that building, the airflow is sucked in the low-pressure area, moves roundly, and finally, a large eddy is created. This eddy is the reason for the negative pressure on the leeward side. For the lateral side, the suction on surfaces is the sequence of the corner effect. Negative pressure is hugely harmful at the lateral side edges and on the main building's rooftop, such as destroying roof structures or windows.

SST – SBs case   LES–SBs case
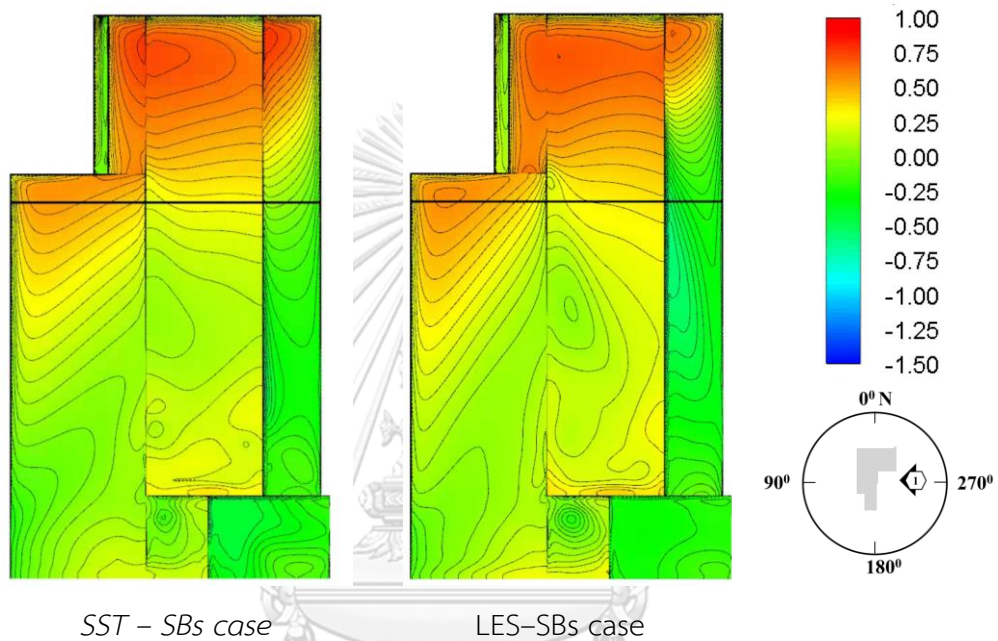
Figure 6-3 Mean pressure coefficient for wind direction 270°
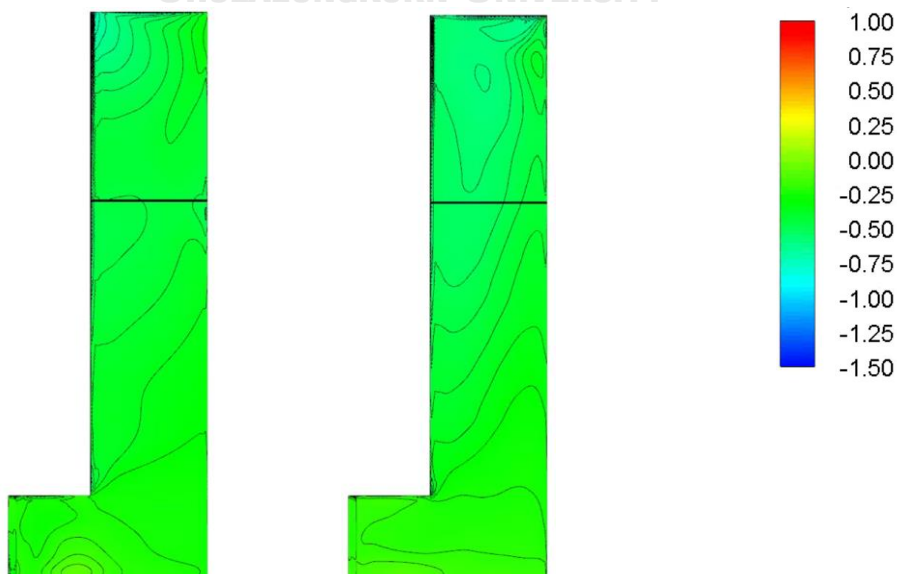
SST – SBs case　　　　　　LES–SBs case
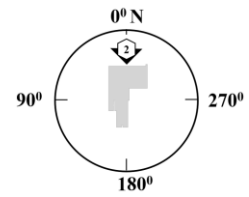
Figure 6-4 Mean pressure coefficient for wind direction 270° (continuous)
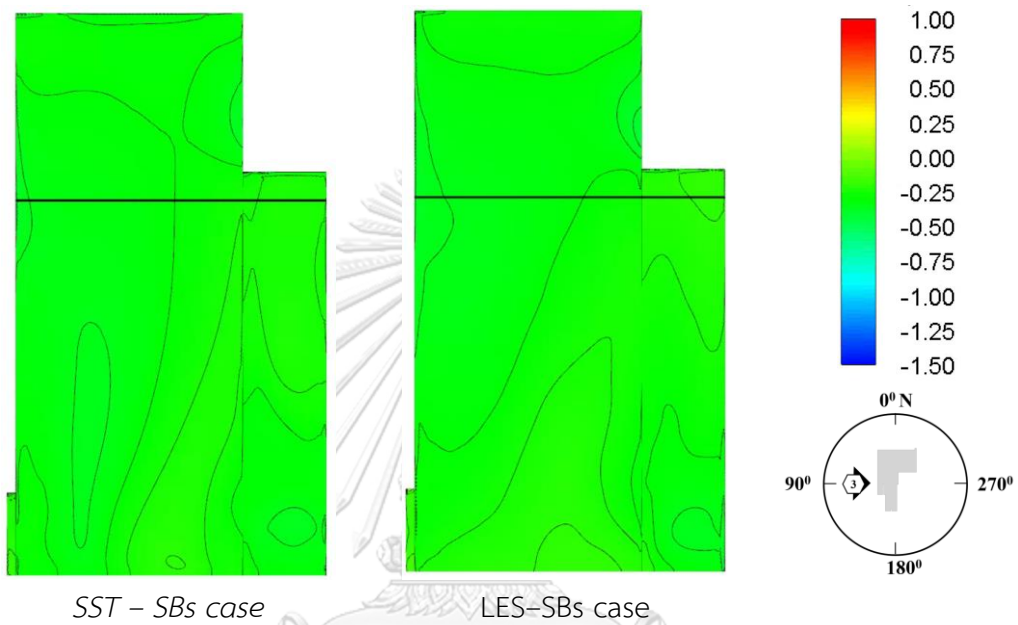
SST – SBs case　　　　　　LES–SBs case

Figure 6-5 Mean pressure coefficient for wind direction 270° (continuous)
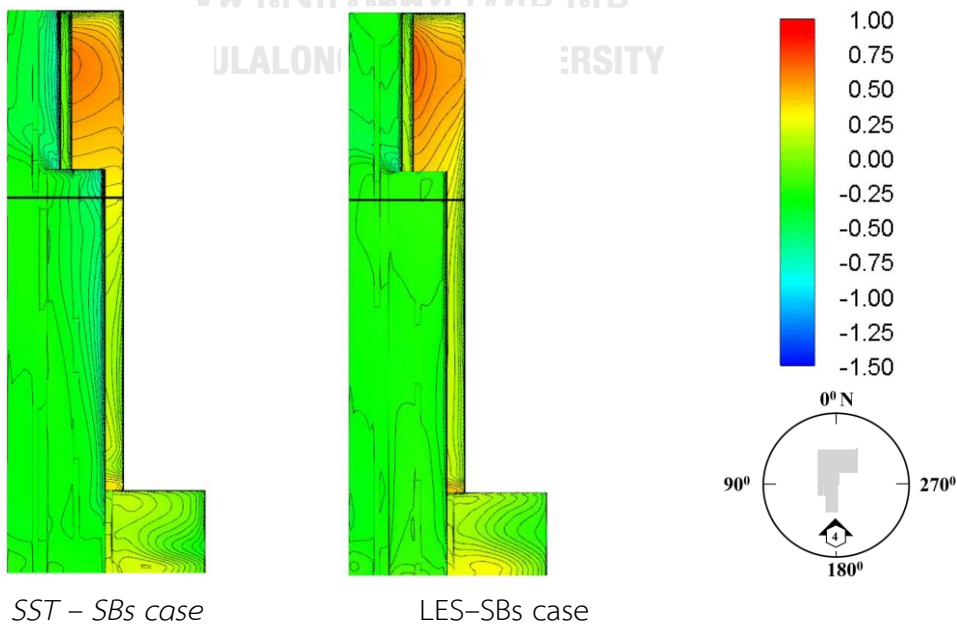
SST – SBs case　　　　　　LES–SBs case

Figure 6-6 Mean pressure coefficient for wind direction 270° (continuous)

| SST – SBs case | LES–SBs case |
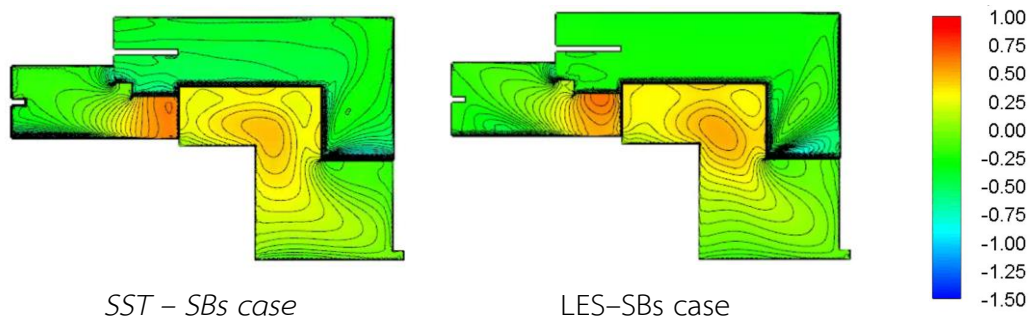
Figure 6-7 Mean pressure coefficient for wind direction 270° (continuous)

To measure how accurate the CFD simulation in the wind load evaluation, the CFD simulation case will be compared to the experimental test (WTT) in terms of dimensionless parameter - mean pressure coefficient.

The first area is the significant positive pressure area, which located near the top of the facade (Figure 6-8a). The mean positive C_p in this area was in the range of 0.51 to 0.82 in the experiments. LES-SBs case had the results in the range of 0.53 to 0.77. In the last, the SST–SBs case showed in range of 0.58 to 0.79. Besides, Figure 6-8a illustrated in this region, the different results at each tracking point were less than 10%, which is an excellent agreement between simulation and experimental tests. Moreover, the plot in Figure 6-8b shows how close the $k-\omega-SST$ turbulence model approach (RANS) to mathematical solution LES in terms of the mean C_p.
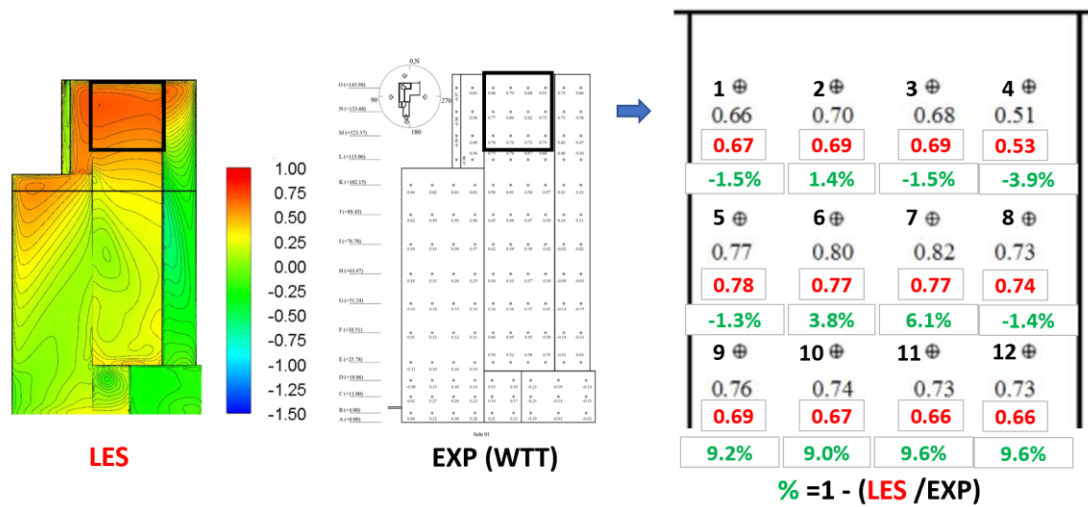
(a) Differences between the experiment (WTT) and CFD simulation by percentage at numbered sensor positions (*)
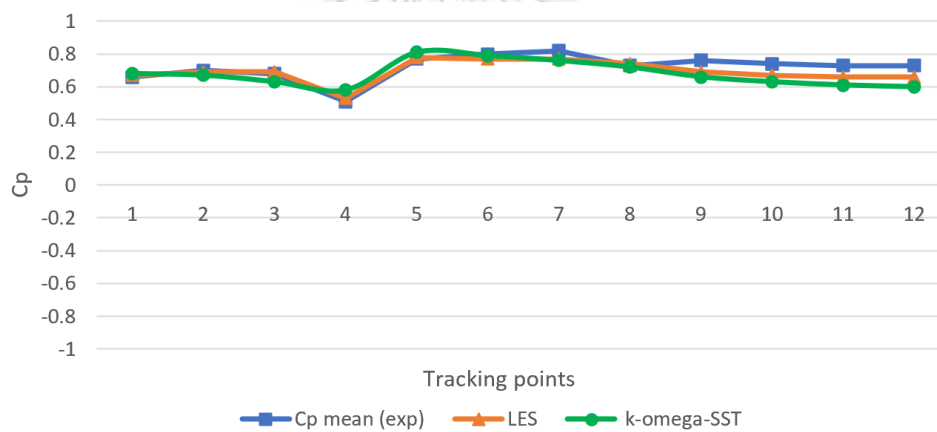
(b)) Mean pressure coefficient plot of the positions in (a)

Figure 6-8 Cp at the largest positive pressure area of the experiment (WTT) and CFD simulation:

(a) Differences between the experiment (WTT) and CFD simulation by percent (*) at numbered sensor positions, and

(b) Mean pressure coefficient plot of the positions in (a).

(*) The error percent (green) equal to one minus the ratio of LES SBs case (red) and experiment result (black). For instance, at censor number 1, the error is -1.5% = 1 – (0.67/0.66).

The following comparison data would be located on all the sensors at elevation +18.06m and elevation +102.15m (from the ground). On each elevation, 28 pressure taps were installed around the building surfaces to receive pressure signals in WTT (Figure 6-9a). The mean C_p is varying in the range of -0.6 to 0.3 at the level +18.06m, and from -0.8 to 0.8 for level +102.15m. In both elevations, the results between CFD simulation and WTT data are almost agreed. LES-SBs case showed an excellent approach when all the values were getting close to the experiment (WTT). The SST-SBs case had a lower accuracy compared to LES-SBs one, but it still provided an acceptable result.

In Figure 6-9b, at the tracking point number 5, 6, 13, 14, 15 & 16 (A1 and A2 regions in Figure 6-9a), a difference occurred between CFD simulation and WTT. In the SBs case simulation, the geometry of surrounding areas was investigated by using Google Maps (locations, building heights) and internet information. Measurements of the SBs building heights based on the estimation with pictures in the WTT reports and internet information (guesswork). Thus, the geometry of SBs perhaps does not identical between WTT and CFD simulations. This assumption can generate the deviation of flow properties such as the locations and magnitude of vortexes.

(a) Censor positions at elevation 18.06m & 102.15m

(b) Mean pressure coefficients at elevation +102.15m

(c) Mean pressure coefficients at elevation +18.06m
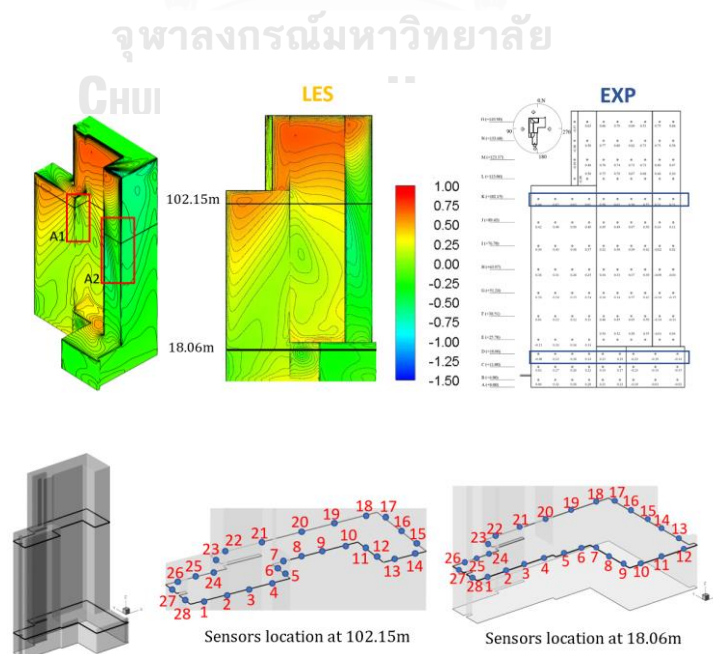
Figure 6-9 Pressure coefficient in comparisons:

(a) Censor positions at elevation 18.06m & 102.15m,

(b) Mean pressure coefficients at elevation +102.15m, and

(c) Mean pressure coefficients at elevation +18.06m.

0,N

O (+143.98)

90   270

N (+133.68)

180

M (+123.37)

L (+113.06)

K (+102.15)

J (+89.43)

I (+76.70)

H (+63.97)

G (+51.24)

F (+38.51)

E (+25.78)

D (+18.06)

C (+11.00)

B (+4.00)

A (+0.00)

-0.37	0.63	0.66	0.70	0.68	0.51	0.75	0.66		
-0.38	0.58	0.77	0.80	0.82	0.73	0.73	0.58		
-0.39	0.48	0.76	0.74	0.73	0.73	0.60	0.47		
-0.38	0.56	0.75	0.70	0.67	0.68	0.46	0.30		
0.46	0.62	0.63	0.61	0.58	0.61	0.56	0.57	0.31	0.21
0.42	0.49	0.50	0.40	0.45	0.49	0.47	0.50	0.14	0.11
0.30	0.43	0.38	0.37	0.32	0.39	0.39	0.42	-0.02	0.02
0.18	0.31	0.26	0.25	0.34	0.33	0.37	0.39	-0.09	-0.01
0.10	0.19	0.15	0.24	0.34	0.34	0.37	0.42	-0.14	-0.15
0.01	0.13	0.12	0.11	0.46	0.45	0.45	0.50	-0.14	-0.11
				0.54	0.52	0.58	0.55	-0.01	0.04
-0.11	0.10	0.16	0.14						
-0.08	0.13	0.18	0.14	0.13	0.19	-0.23	-0.19	-0.14	
0.02	0.27	0.26	0.22	0.14	0.17	-0.23	-0.14	-0.15	
0.06	0.32	0.38	0.28	0.21	0.23	-0.19	-0.03	-0.02	

(a) Mean Cp in the wind tunnel test

105

(b) Mean Cp in SST–SBs case   (c) Mean Cp LES-SBs case

Figure 6-10 The mean Cp at the windward face of the primary building:

(a) Mean Cp in the wind tunnel test,

(b) Mean Cp in SST–SBs case, and

(c) Mean Cp LES-SBs case.

		-0.25	1.19	1.02	0.98	1.01	1.03	0.98	0.87
		-0.25	1.19	1.02	0.96	0.92	1.03	0.88	0.6
		-0.33	1.45	0.92	0.91	0.9	0.9	0.44	0.23
		-0.53	1.19	0.81	0.81	0.8	0.8	-0.06	-0.19
1.05	1.05	0.94	0.97	0.95	0.96	0.98	0.98	-0.1	-0.74
1.15	1.11	0.85	0.87	0.6	0.76	0.84	0.83	-3.35	-2.1
1.57	0.96	0.93	0.46	0.44	0.61	0.84	0.86	24.94	-14.3
2.08	0.93	0.81	0.54	0.5	0.53	0.75	0.84	4.79	33.21
2.77	1	0.86	0.65	0.8	0.76	0.76	0.82	2.29	2.05
19.21	0.93	0.95	1.71	0.56	0.64	0.73	0.81	1.48	2.04
-1.11	0.8	0.83	1.46	0.73	0.69	0.65	0.71	10.4	-1.7
1.01	0.81	0.88	1.18	0.91	1	0.99	1.19	1.18	
0.31	0.32	0.64	1.02	0.41	0.48	1.05	1.62	1.2	
0.14	0.37	0.59	1	1.04	1.18	1.13	5.72	4.77	

(a) The ratios of mean Cp in **LES–SBs** case to mean Cp in **WTT**

(b) Contour map of ratios in (a)
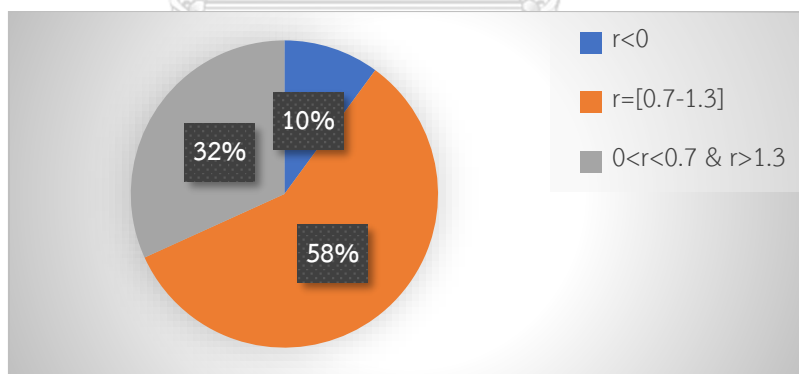
(c) Statistical percentage of values in (a)

Figure 6-11 The comparison of mean Cp of LES-SBs case and the wind tunnel test at the windward face of the primary building:

(a) The ratios of mean Cp in LES-SBs case (Figure 6-10c) to mean Cp in wind tunnel test (Figure 6-10a),

(b) Contour map of ratios in Figure 6-11a, and

(c) Statistical percentage of values in Figure 6-11a.
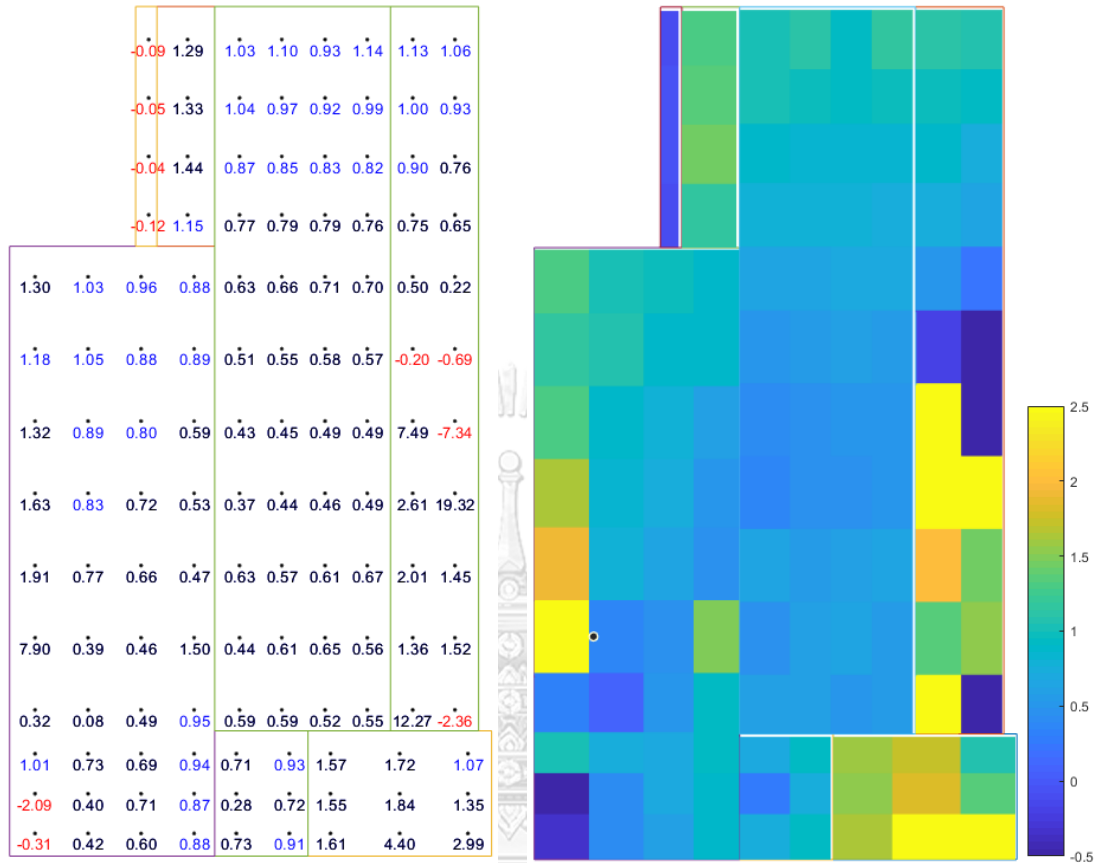
(a) The ratios of mean Cp in **SST–SBs** case to mean Cp in **WTT**

(b) Contour map of ratios in (a)
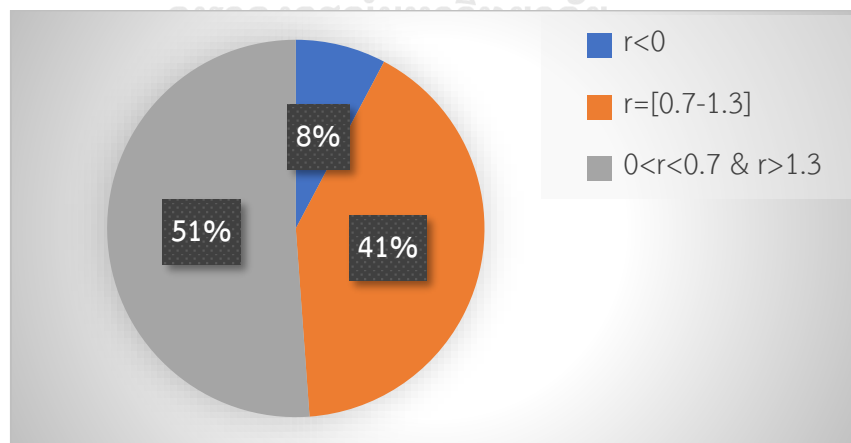
(c) Statistical percentage of values in (a)

Figure 6-12 The comparison of mean Cp of SST-SBs case and the wind tunnel test at the windward face of the primary building:

(a) The ratios of mean Cp in SST–SBs case (Figure 6-10b) to mean Cp in wind tunnel

test (Figure 6-10a),

(b) Contour map of ratios in Figure 6-12a, and

(c) Statistical percentage of values in Figure 6-12a.

Now, let us take an observation on over the windward faces:

+ For the LES simulation, on the primary building's windward surface, the ratio in the range of 0.7-1.3 was 75/129 locations (58%). In other words, the difference below 30% accounts for 58%. The negative ratio, which shows the opposite prediction between LES with WTT, is less than 10% (13/129 locations) (Figure 6-11c).

+ While, the SST simulation accounts for 41% of under 30% difference (53/129 locations), and 8% for opposite prediction with WTT (Figure 6-12c).

Both LES and SST simulations took a good prediction for the pressure on the windward surface. However, in some specific areas, which are the left edges and the right of the building, there is a lack of accuracy. As the discussion above, the SBs building heights measurements were based on the estimation with pictures in the WTT reports and internet information (guesswork). Thus, the geometry of SBs perhaps does not identical between WTT and CFD simulations. This assumption can generate the deviation of flow properties such as the l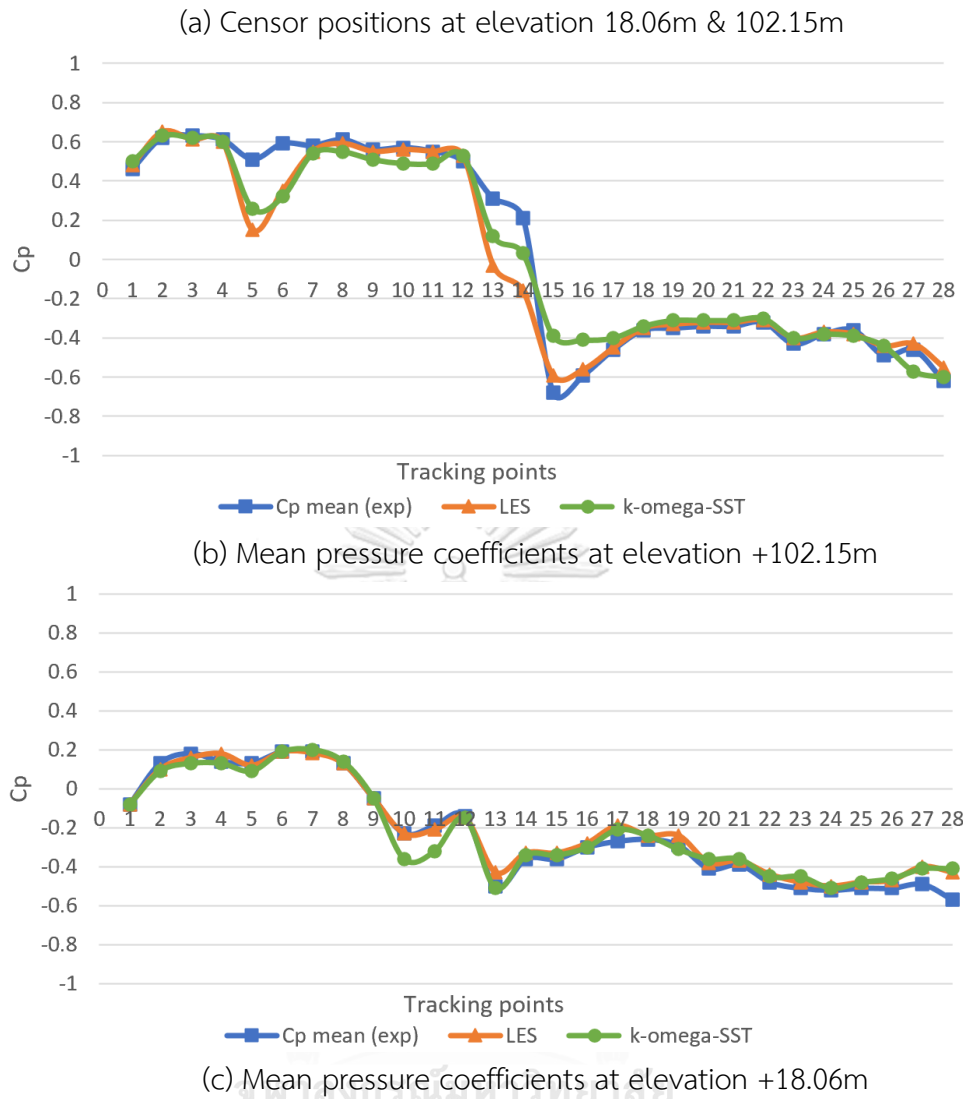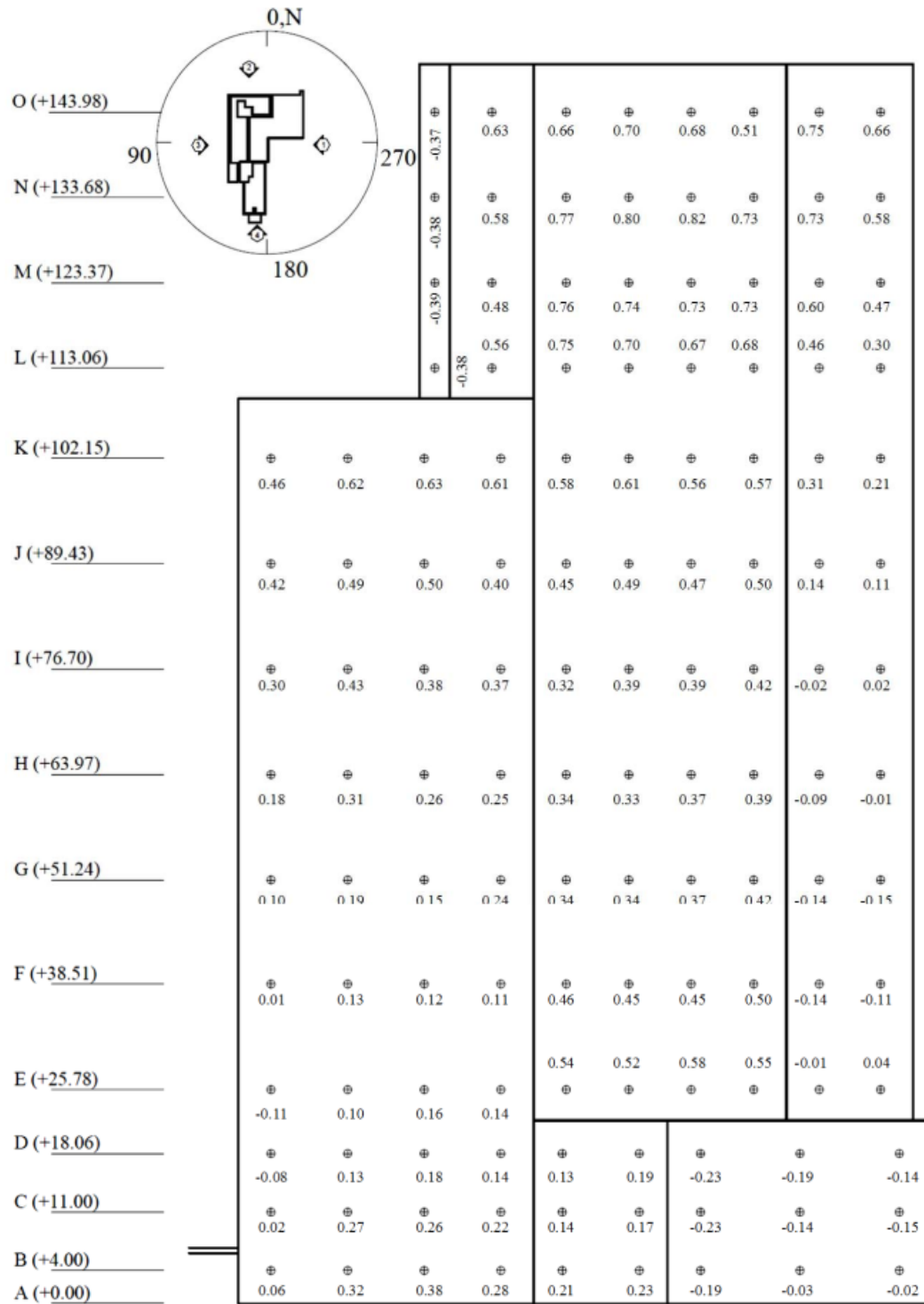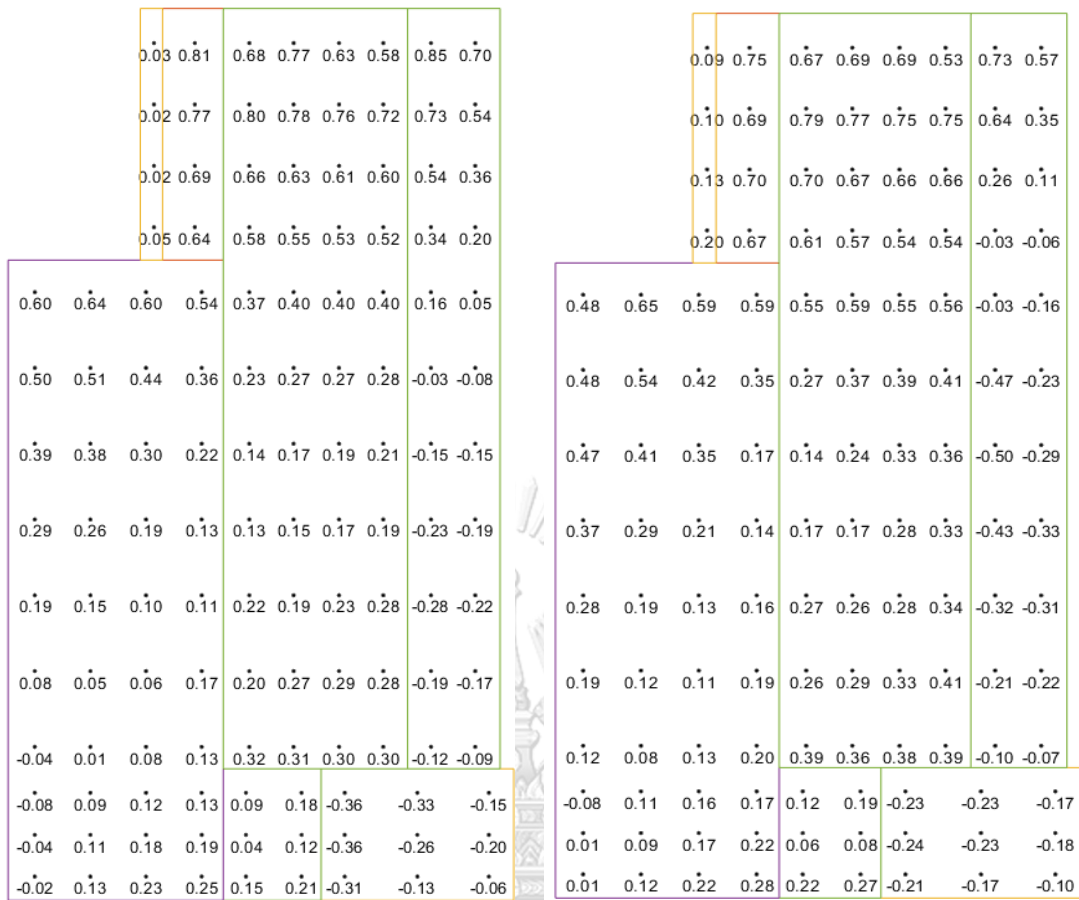ocations and magnitude of vortexes. From that, there was an influence on the pressure distribution, which showed the difference compared to WTT. Finally, the result also indicates that, LES is slightly more accurate than SST in mean Cp prediction.
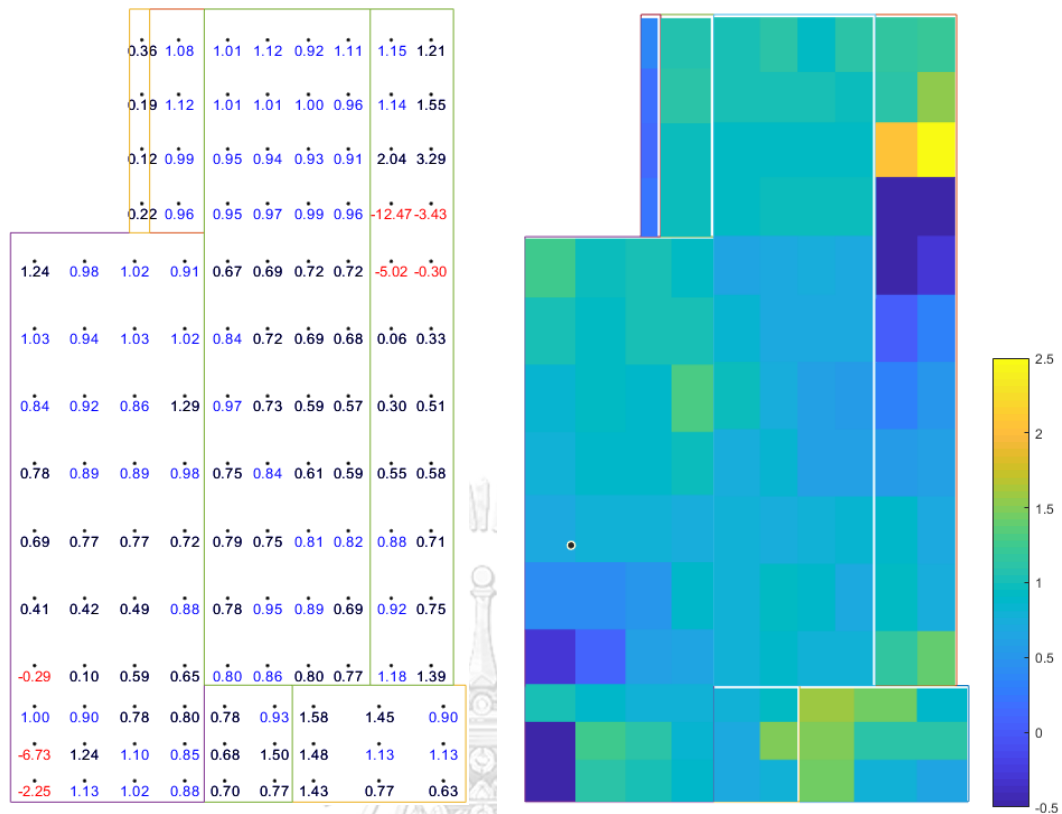
(a) The ratios of mean Cp in **SST-SBs** case to mean Cp in **LES–SBs** case.

(b) Contour map of ratios in (a)
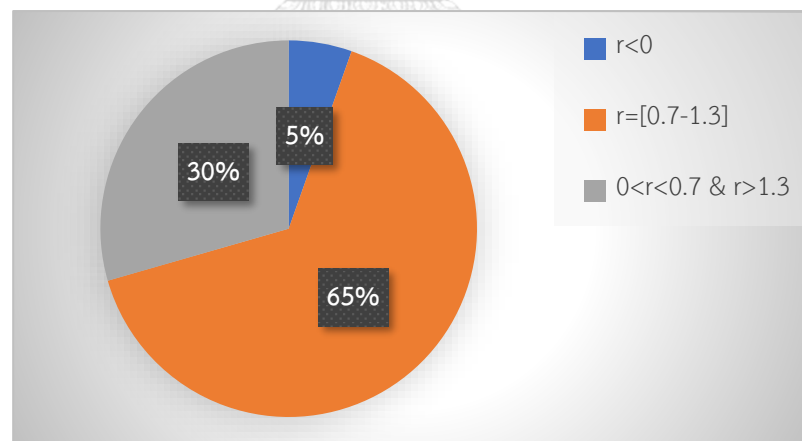
(c) Statistical percentage of values in (a)

Figure 6-13 The comparison of mean Cp of LES-SBs case and SST-SBs case at the windward face of the primary building:

(a) The ratios of mean Cp in SST–SBs case (Figure 6-10b) to mean Cp in LES-SBs case (Figure 6-10c),

(b) Contour map of ratios in Figure 6-13a, and

(c) Statistical percentage of values in Figure 6-13a.

The $k-\omega-SST$ turbulence model approach (RANS) cannot provide the transient flow's characteristics like the LES approach. However, in the averaged term like pressure coefficients, this method proves a good result compared to LES. Figure 6-13 presented that the difference between the two cases is small and acceptable in most of the areas. The ratio in the range of 0.7-1.3 was 84/129 locations (65%). The negative ratio, which shows the opposite prediction of two cases, is less than 5% (7/129 locations) (Figure 6-13c).

Most of the regions having the difference located on the right side of the windward face, in which the large vortexes occur under the influence of the SBs area. LES shows its advantages to simulating them precisely for those regions with occurring of vortexes or high turbulent areas. While with the low turbulent area, both LES and RANS are almost identical in the results.

Though the above comparisons in terms of mean pressure coefficient distribution on the main building, CFD simulation proved its accuracy and practical in wind load estimation. Besides, the results between two approaches of simulation (LES and the $k-\omega-SST$ turbulence model) are almost identical, with small errors. The use of RANS in simulations would be beneficial for saving computational resources.

CHAPTER 7

COMPUTATION TIME

7.1 The computation time

Thirty years ago, the LES approach was never a go-to method for engineers who worked in the CFD simulation field. LES took a giant resource for a simple simulation with that day's computer power. The only solution was simulating on High-Performance Computers (HPC) or supper computers, which opens belongs to governments, big universities/institutions, and specialized research centers. Hence, the simulation at that time purposed to individual researches and essential studies. For practical, it was still an unreachable solution. Instead, a wind tunnel test or a water tunnel test had many advantages compared to CFD simulation in terms of cost and time-consuming.

Wind load analysis is a standard topic that was experienced with CFD a long time ago. However, the disadvantages have existed and partly effect it becomes a useful and practical tool. The geometry is complicated because of the high urban density and various building shapes. That dragged the large-element mesh with the high resolution required and adaptive with the sudden change of shapes. A massive number of elements directly affect computational cost and solution time.

An accurate CFD simulation requires a proper mesh for the following reasons. They relate to the high-turbulent flow, large eddies generation, and geometry complication in the building area. They need a fine mesh with high resolution to catch all the physic phenomena correspondingly. For instance, the LES solves the vortexes from a large scale with high energy to the smallest one. The smaller eddy is, the more it depends on grid resolution. LES ignores those vortexes having a size that is smaller than the smallest grid size. The coarse mesh cannot provide accuracy solving for full of vortexes, leading to non-physical characteristics or stops the full development of flow in the computational domain.

Time changes, the computer now is hugely more powerful and cheaper. Nowadays, the evolution of the computer chip is a nonstop race. Additionally, CFD algorithms have been improved to solve problems fast and faster. At this moment, CFD simulation is no longer performing exclusively on HPCs or supercomputers, and it merely runs with a home desktop, even a netbook with a basic configuration. Of course, a powerful computer reduces solving time significantly. Besides, the cloud computing platform has put a leg in this race, and the ability to reach CFD simulation without hardware limitations has never experienced before. These achievements had never happened three decades ago, but science and technology's magical evolution has proved nothing impossible.

All cases in this study were simulated in our laboratory at Chulalongkorn University on a computer desktop. At the time of writing this thesis, the year 2020, our computer configuration is not a high-end one with a CPU chip in 2019 (9th generation). Moreover, just a year has gone (only one year); it is slower than its late generation (10th generation) from 1.5 to 2 times depends on computational tasks. There was a little regret in our investment because of slippage, but an excellent signal for the semiconductor industry development.

Table 7-1 Computation time of SBs cases simulation

Approach Method	K-ꞷ-SST TB (RANS)	LES
Time (type)	Steady	Transient
Residual levels	1E-05	
Algorithms	SIMPLEC (skewness correction = 1, second order for	
Mesh size	5.8 milions cells - primary stucture and surrounding area	
Flow time/ Interations	3000 iterations	~ 8.0 seconds from steady state; time step size = 0.002s
Sampling data	last 1000 iterations	~ 7.0 seconds (1 second after running)
Computer configurations	CPU: I7 - 9700k (base clock speed at 3.6Ghz, OC upto 5.0Ghs), 48Gbz RAM 2133 MHz	
Simulation time	~10 hours (1 night)	~150 hours (6,25 days)

Simulation time (hour)
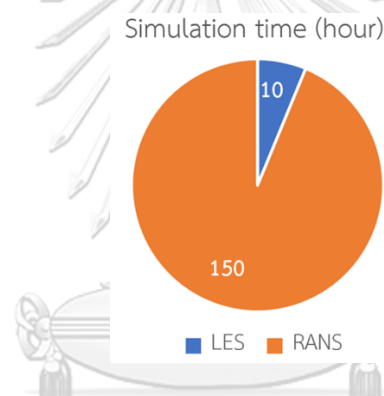
In Table 7-1, a short comparison illustrated the time simulation of the two approach methods in the simulation with SBs (with the same boundary condition, meshing, computer configuration, and other settings). There is no doubt about how aggressive LES was comparing with the SST case (RANS). RANS approach finished the solving in a night with 10 hours running straight on 5.8 million cells, while it took almost a week (150 hours) continuous solving using LES on the same gird resolution. Fifteen times longer is a remarkable number to prevent engineers go with the LES approach. Additionally, because LES is a transient simulation, every 50 iterations (0.01s flow time), its data need to be stored a file for transient phenomena study. For instance, the LES SBs case took 800 GBs of storage in this study, which means massive storage needed in LES simulation.

The LES simulation time will be dropped massively in the same way it was from 30 years ago until now. Note that LES is a mathematic simulation and a transient state when every element within the domain will be solved. Thus, most vortexes at several ranges will be solved in every time step. The rest, which has a smaller size than the "cut-off" width (discussed in 2.4.2), will be modeled as the sub-grid scale (SGS) eddies. The smaller eddy is the more computational cost because of high mesh resolution. So, a fine mesh will take longer to solve than a course mesh but more accurate.

7.2 Recommendation for selection of method

The accuracy and the advantage of the two-approach (LES and RANS) were discussed in the above sections. Nevertheless, the selection of a CFD simulation approach is till questionable through the time. There is no such clear choice for this hesitation because of the following explanations.

LES approach provides high detail flow properties that are the time-dependent flow characteristics. In other words, LES can provide a state of flow on its travel path with time-dependent, monitors how the flow changes, fluctuates, or transforms. Transient flow features include flow separation, flow circulation, formation & disappearance of an eddy and its transform. All the above details from LES give us the nearest natural wind flow as the virtual flow, where conservation laws dominate the flow properties. That is hard to reach by the standard RANS approach method.

LES solves the whole fluid domain through the time so that the data is a big set and occupies an ample storage space (that cannot avoid). Thanks to commercial software like ANSYS Fluent, this data set is now easy to perform to users as a visual look (such as contour map, streamlines, and 3D view flow). Besides, LES's codes recently have been more practical, useful, and improved. For example, streamline patterns can capture all wind flow scenarios with an easy way to observe than experiments could

do. The change of color range on a pressure contour map illustrates the concentration of pressure on the cladding surface. From all the advantages LES provides, it can use in many fields with high efficiency.

For instance, A new town/city plan project needs to have a wind flow information to arrange the positions of buildings or functional structures; this task needs to be invested at the first steps of the project, to guarantee the urban beauty and avoid local climate changing. A structural designer needs to analyze the building's wind effect to choose suitable materials for cladding design. With the aid of CFD simulation, the pedestrian comforts and safety under the effect of wind flow can now be visualized; because the speed exaggeration could happen in the complex urban area (this will be mentioned in the next chapter).

Murakami (1990) suggested that "Time-dependent flow fields given by LES and the techniques of visual animation based on them are very useful tools in turbulent flow analysis concerned with wind engineering and provide information hardly given by experimental techniques." The significant disadvantages of LES are always high-cost taking and time-consuming, users need to consider when choosing this approach.

Back to our historical approach – RANS. It is undoubted about how fast RANS could give us in simulation. RANS's accuracy in the averaged terms is outstanding and promising. With the simple simulation process, the less time-consuming, direct result using without a sampling process, and require an entry-level budget, RANS is suitable in the early design state (correct design) of a building. In this state, RANS could support the designers in shape design optimization, correcting the concept. For example, the use of CFD in natural ventilation (passive cooling system) is so effective and straightforward, such as visual the flow moving can help designers decide the open holes (windows and door) to exploit the wind flow. In conclusion, RANS help to leads the designer to approach an excellent final solution with high efficiency and

low cost without a massive investment in the beginning. At the moment, the concept is no longer changed; LES can be used to get a better and accurate solution.

LES is at least potentially more accurate and reliable than RANS because it solves more of the flow. As we mentioned, the high grid-sensitive characteristic of LES can make the computational cost increase massively. In contrast, it can be handled efficiently by RANS, even with a lower resolution mesh. That confirms RANS models still beneficial in experience for a long time. Perhaps, it will be last long until the computational cost is affordable for LES. Again, until this moment, the chosen still depends on the purpose of simulation and budget investment.
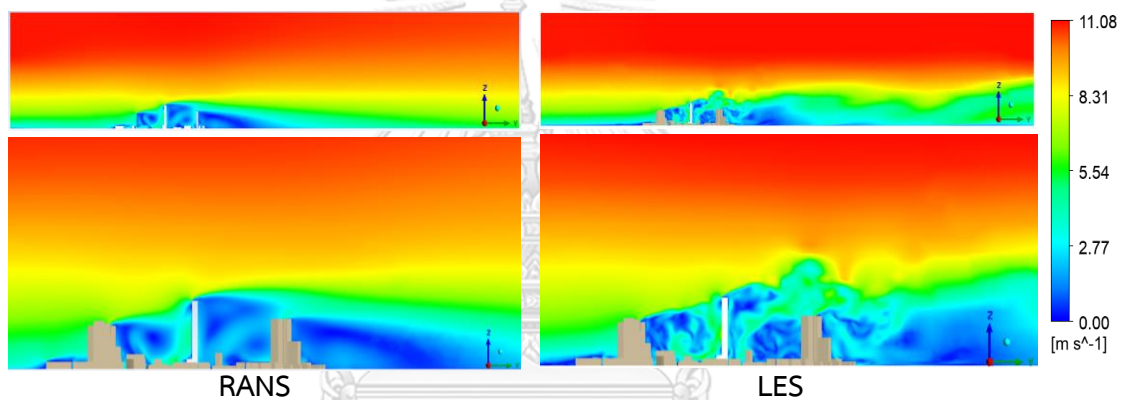
Figure 7-1 LES simulation provides more information on flow properties

CHAPTER 8

CONNECTION TO BUILDING CODES

Firstly, the brief review of two wind load codes/standards would be brought out below, to illustrate their application scope in wind load evaluation on the buildings or other structures. The first standard would be ASCE 7, the famous, widely used, and mostly adopted by several standards/codes worldwide. Secondly, the primary standard was used in this study's building and the country's legal tool where it located, Thailand Wind load code - DPT Standard 1311-50.

8.1 Wind load calculation in ASCE 7

ASCE 7 is the famous building code that has been developed by the American Society of Civil Engineers since 1972. ASCE 7 provides the minimum requirements for a building's structural elements, from the design to installing and operating phases. The purpose of ASCE 7, as same as these other codes, is bringing to engineers a standard, which can help design the structural components safely and reliably with the minimum loads. ASCE 7 covers widely from the principal elements (such as beams, slabs, walls, and columns) to secondary members (such as cladding design). For reference in this study, the wind load parts from Chapter 26 to Chapter 31 in ASCE/SEI 7-16 (2017) would be mentioned. ASCE 7 gives the designers three options to evaluate the wind load for buildings and other structures:

1. Analytical procedure,

2. Simplified procedure, and

3. Wind tunnel procedure.

There are different features of the three approaches. The analytical procedure can be applied for all building's appurtenances, whereas the simplified procedure is limited to certain types of structures with followed requirements.

A "simplified method" for which the designer can select wind

pressures directly from a table without any calculation, where the

building meets all the requirements for application of the method,

is provided for designing buildings using the Directional ..." (P.731,

ASCE/SEI 7-16 (2017))

Commonly, engineers are recommended to use the simple procedure in case of the building had common characteristics. Those are low-rise buildings, or one has the roof height less than 160 ft ~ 48.8 m, regular-shape design, and mostly enclosed and rigid (lowest vibration frequency greater than 1 Hz or having a height smaller than four times the least horizontal dimension). Notably, the building is not located in a region where significant turbulence may occur (such as the wake region of other tall buildings).

ASCE/SEI 7-16 (2017) provides a set of tabular forms for the Main Wind Force Resisting System (MWFRS) and for Components and Cladding (C&C) to use directly. However, there are limitations in the calculation provided in the standard (Coulbourne and Stafford, 2020).

When a building or structure meets out of all the above characteristics; however, it remains in regular shape and not staying in a complicated wind flow region, the analytical procedure is encouraged to apply. There are two analytical procedures for MWFRS design: directional procedure and envelope procedure.

- Directional procedure

    As the name of this procedure, it mainly relates to the wind flow direction. Based on the experiments - wind tunnel tests for wind flow associated with the specific wind direction, ASCE/SEI 7-16 (2017) provide users the referenced pressure coefficients to apply in the wind load formulas directly. However, it remained in regular shape structures and attached the list of the requirements.

- Envelope procedure

This provision mainly uses for MWFRS of a low-rise building where the wind loads are obtained by envelope procedure. Low-rise buildings are defined as those that have mean roof height less than or equal to 60 ft ~ 18.29 m, and that height does not exceed the least horizontal dimension.

The wind tunnel procedure is similar to the analytical procedure about what type of structure could be used. This method requires a WTT on a scaled-down model of the real structure in the wind tunnel. However, because of its high cost and extra time-consuming, this procedure's scope is limited in unusual/irregular shape buildings and the critical wind load scenarios.

8.2 Wind load calculation in DPT Standard 1311-50

Referenced on the National Building Code of Canada (1995), the Engineering Institute of Thailand published the wind loading standard for building design - EIT Standard 1018-46, (2003). In 2007, the Department of Public Works and Town & Country Planning (2007) published a revised and updated the version in 2003, which was named DPT Standard 1311-50. Until now, DPT Standard 1311-50 has been a useful and legal tool in wind load evaluation in Thailand.

The DPT Standard 1311-50 provides three methods to determine design wind loads on buildings and other structures:

(1) Simple procedure

Structure and cladding design of low and medium-rise buildings & cladding design of high-rise buildings are two main types of this procedure heading to. However, this procedure required a building with a slight effect from dynamic actions. The buildings or structures are relatively rigid, and equivalent static loads can use for dynamics actions.

(2) Detailed procedure

The application scope of detailed procedure is beyond the above simple procedure when it supports the building with higher dynamic actions. Those buildings under its scope should have heights exceeding three times the least efficient width, lightweight, greater than 80m, or have a reason to believe their frequencies are less than 1 Hz (natural period greater than 1 sec). Those kinds of buildings are easily susceptible to vibration; thus, the simple procedure can not cover efficiently.

Even having a wide range of support, but for the case has irregular-shaped design and hard to simplify into those typical shaped building, the detailed procedure will show its weaknesses. Thus, there is a high recommendation to use the wind tunnel test procedure to investigate wind loads properly.

(3) Wind tunnel test procedure

The experiments would help to determine the correct dynamic response and provide exterior pressure coefficients for cladding design with great detail of wind flow information. It is appropriated for irregular-shaped buildings or structures which are out of the standard application scope.

8.3 Role of CFD in wind load evaluation

There are not any standards/codes that have adopted the CFD tool as a legal tool (yet). As mentioned in 1.1, the contribution to the validity of the CFD has never stopped for years.

> *"...Some countries have already built working groups to research the CFD's practical applicability and have developed recommendations (or guidelines) for practical building design. The Architectural Institute of Japan (AIJ) developed a CFD application guideline on high-rise buildings (Tamura et al., 2008). Then, they published the first CFD guideline for structural purposes in 2015. They adopted CFD simulations for wind load investigation,*

provided that knowledgeable handling the software and critical examination to be performed by an experienced wind engineer (AIJ, 2017). This publication's language was Japanese, but luckily some researchers have presented it in a few articles by English.

Meanwhile, European Cooperation in Science and Technology (COST) published a practice guideline for CFD simulation of flows in an urban environment using steady-state RANS models (Jorg Franke et al., 2011). American Society of Civil Engineering (ASCE) contributed a task committee that aims to provide civil and environmental engineers guidance on using computational fluid dynamics in handling fluid-related problems. However, it was still restricted in water and wastewater treatment fields...(discussed in 1.1)"

Even not include in any wind load codes or building standards, the CFD simulation referred to them' requirements. Back to section 4.5.1, the vertical velocity profile and turbulent intensity of an urban area given by "power law" in ASCE Manual of Practice No. 67 (1999) and ASCE (2005) were adopted to generate the wind speed gradient in ABL. Then this information about wind profile was used as the inlet boundary condition in CFD simulations.

We were searching the keyword "CFD for wind load analysis" on Google Scholar (*), it provides 75000 results for any time, and 2300 results since 2020 (statistics to June 2020). This is a good signal indicating that many researchers have intensely studied this field. Hence, more and more validation cases will be obtained, come after with more and more CFD guidelines for practical application will be released. We have confidence in this promising method in wind load evaluation.

(*) Google Scholar is a freely accessible web search engine that indexes the full text or metadata of scholarly literature across an array of publishing formats and disciplines. Wikipedia
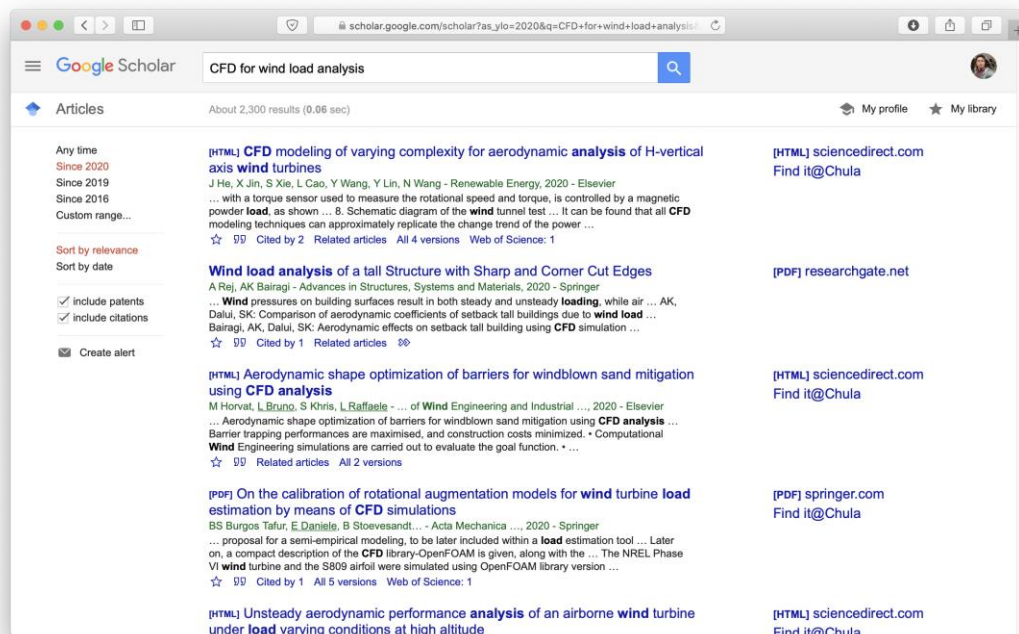
Figure 8-1 The results for "CFD for wind load analysis" on Google Scholar website

Now, let us discover a few scenarios, which CFD simulations can join and show their advantages. There are four applications will be covered, includes:

- The CFD simulations support building design
- CFD simulation helps to investigate the wind environment
- Application of CFD in the wind tunnel test process
- CFD simulations in investigating the pedestrian comfort

8.3.1 CFD simulations to support building design

Even providing a wide range of applications, building codes still need the aid of WTT in the case of unusual shapes, complex wind flow conditions, and sensitive dynamic action structures. There will be a long period to the day CFD simulation could replace the role of WTT or being a virtual wind tunnel test because of its classic drawback. However, at the early stage of building construction, CFD simulation is promising.

Suppose a building's estimation falls in a few conditions such as high wind loads or turbulence (resonance can occur and enlarge the building movement). Besides, the building shape is not a case covered by codes, hard to apply building codes directly or require an expensive experimental test. CFD can offer beneficial and insightful suggestions to help adjust/modify the design.

In practice, the number of building use WTT is limited as a small number. Mostly, the codes/standards are the solitary tools that engineers can reach. That will be a place for CFD's application being a validation solution for the code/standard application.

Here is an example of the building shape optimization from Asghari Mooneghi and Kargarmoakhar (2016). The minor modification, such as using "Recessed Corners" or "Double Chamfered," will get the smaller separation zones and narrower wakes than a simple square shape (Figure 8-2).
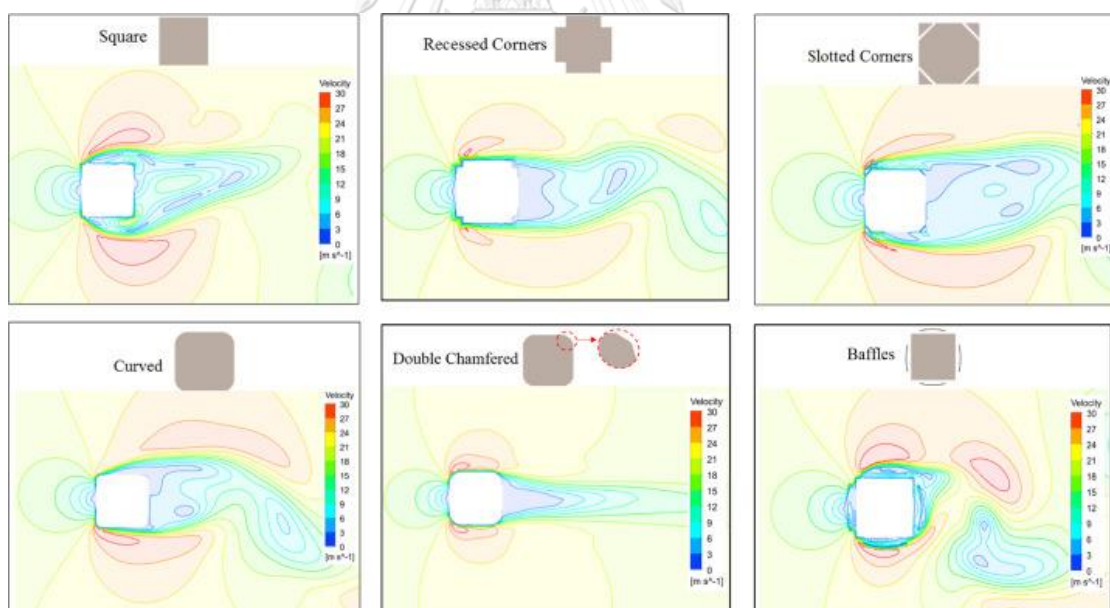
Figure 8-2 Wind flow field around different cross-sections.

(Asghari Mooneghi and Kargarmoakhar, 2016)

8.3.2 CFD simulation to investigate windy environment

ASCE 7 takes care of the topographic effects such as hills, ridges, and escarpments by providing a topographic factor (K_{zt}) in wind pressure formula (section 26.8 in ASCE/SEI 7-16). The minimum of this factor is 1.0, which means under actions of the above effect, the wind pressure will be enlarged.

Besides, the *DPT Standard 1311-50* provides the exposure factor (C_e) to present the changes in wind speed and height. Moreover, this factor also mentioned the effects of variations in the surrounding terrain and topography.

In CHAPTER 5, we concluded the importance of the *wind environment* (surround buildings around the primary building) in wind load analysis and CFD simulations. So, the standards/codes perhaps apply for most cases of buildings but cannot provide extensive information like CFD. The prediction and measurement of *wind environment* effects such as wake characteristics, flow separations, reattachments, and vortex shedding by using CFD could be beneficial for engineers.

CFD simulation gives the real conditions and turbulent instabilities in the flow development. The wind flow patterns in the interesting area such as vortex location and maximum wind speed of a *venturi effect*. In other words, designers can access wind threats and predict such phenomena, then optimize the safety or performance of their products.

Figure 8-3 Wind environment around the primary building (white building) in LES–SBs case

Figure 8-4 Wind flow streamline in LES–SBs case

8.3.3 Application of CFD in wind tunnel test process

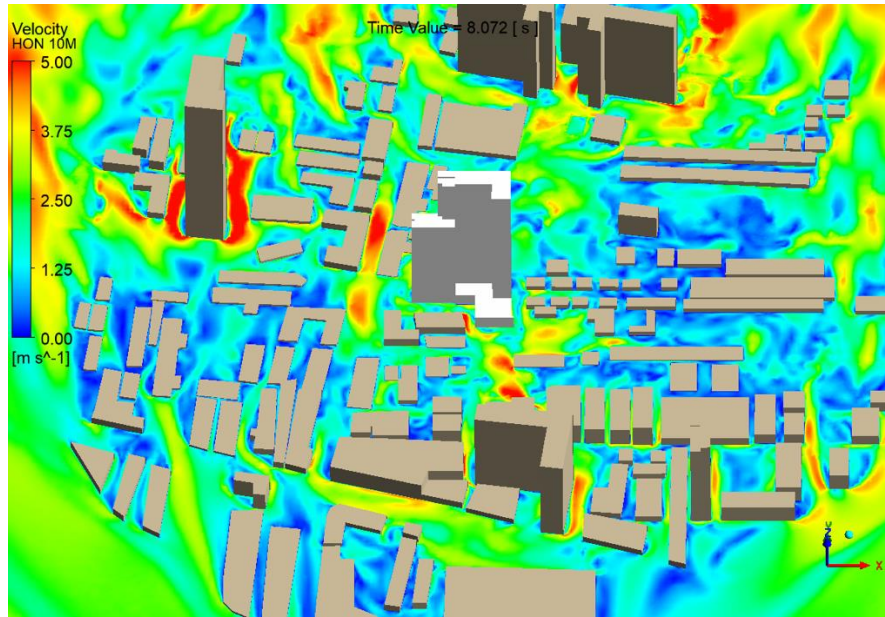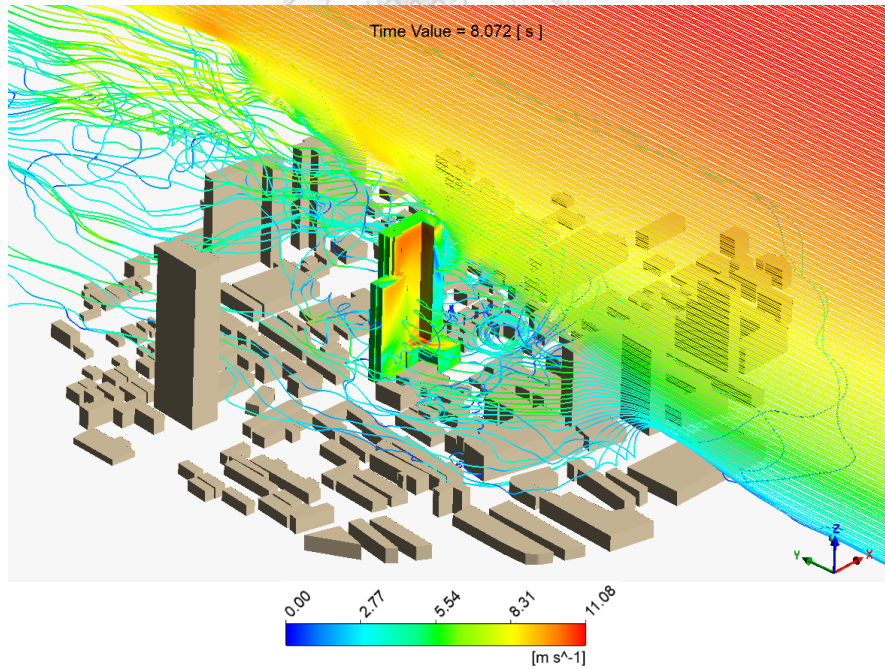The cost of conducting WTT is expensive because of its complicated process and installation. In the early design stage, designers can use the CFD simulation to optimize their design concepts (such as using a rounded edge to reduce wind load pressure and arrange the location of open hold on the building to apply natural ventilation). The final design will be tested in a WTT to confirm the evaluation and get the valid design permission.

The interesting area of the building (such a high negative pressure region on the cladding) will be easily observed by CFD simulation. Hence, engineers can set up the sensor locations in WTT to get expected results instead of spreading out on overall cladding surfaces. Besides, there are no limitations about the size of the model in simulation; CFD can apply to a 1:1 scaled-model simulation or any scaled-down ones. Hence, the correlation and extrapolation accuracy can be improved for the physical test measurements (WTT).

8.3.4 CFD simulations in investigating pedestrian comfort

The process of urbanization is one of the reasons for changing the property of natural flow and influence the urban citizen lifestyle. Under the complicated topography in the dense city, the flow can impact directly and could be risky for pedestrians. As mentioned in 5.1.2, the wind speed can be enlarger cause of the topography effects such as corner effect and venturi effect. Furthermore, with a level of wind speed is listed in the Lawson-based Criterion (Figure 8-6), the impact to pedestrians could be from being uncomfortable to dangerous (wind speed over 14.6 m/s in Land Beaufort Scale (Figure 8-7) can flow the walkers).

Because the CFD can export the results anywhere within the computational domain, the study about pedestrian comfort will be more suitable with CFD than wind tunnel

tests. Besides, with the digital-3D wind flow pattern animation such as streamline (Figure 8-4), the wind flow impact can be observed in detail.

For example, a restaurant with a beautiful outer lobby will be a prominent spot for breakfast services. A vortex or gust could make everything messy with unsatisfied customer feelings. CFD can help the designer to identify the unexpected troubles and locate the windshield or tree pots to prevent those phenomena.

Figure 8-5 Men braced themselves from the rain and the wind

while walking in Copley Square

(on December 30, 2019, ERIN CLARK FOR THE BOSTON GLOBE/FILE)

SITTING LONG	SITTING SHORT	WALKING LEISURELY	WALKING FAST	UNCOMFORTABLE
0.0 - 2.5 m/s	2.5 - 4.0 m/s	4.0 - 6.0 m/s	6.0 - 8.0 m/s	> 10 m/s
5%	5%	5%	5%	5%
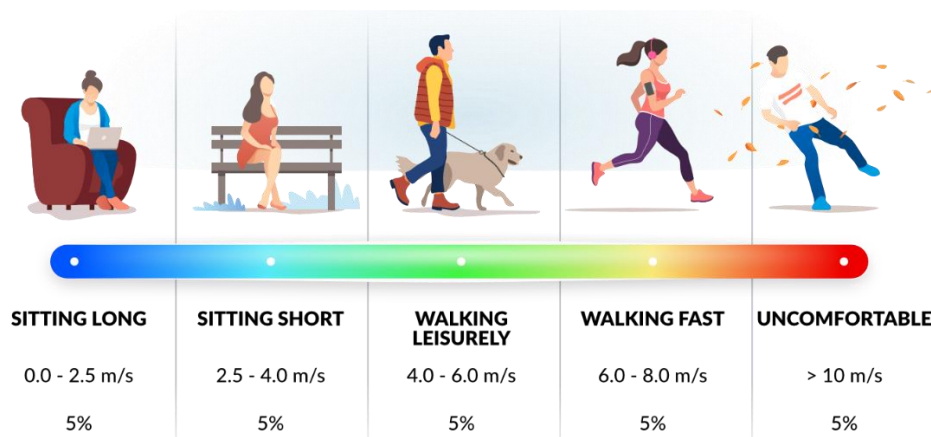
Figure 8-6 Lawson-based Criterion

Table 1. Extended Land Beaufort Scale showing wind effects on people [76].

Beaufort Number	Description	Wind Speed at 1.75 m height (m/s)	Effect
0	Calm	0.0–0.1	
1	Light air	0.2–1.0	No noticeable wind
2	Light breeze	1.1–2.3	Wind felt on face
3	Gentle breeze	2.4–3.8	Hair disturbed, clothing flaps, newspaper difficult to read
4	Moderate breeze	3.9–5.5	Raises dust and loose paper, hair disarranged
5	Fresh breeze	5.6–7.5	Force of wind felt on body, danger of stumbling when entering a windy zone
6	Strong breeze	7.6–9.7	Umbrellas used with difficulty, hair blown straight, difficult to walk steadily, sideways wind force about equal to forwards walking force, wind noise on ears unpleasant
7	Near gale	9.8–12.0	Inconvenience felt when walking
8	Gale	12.1–14.5	Generally impedes progress, great difficulty with balance in gusts
9	Strong gale	14.6–17.1	People blown over

Figure 8-7 Land Beaufort Scale for the pedestrian wind comfort

(Blocken et al., 2004)

The above four applications draw a good picture of the CFD's role in breaking the limitation of building codes/standards and WTTs. The capability of CFD in the civil engineering field is endless. The computer industry's development, the improvement in CFD algorithm solving from researchers, and commercial companies nowadays have brought a bright future for CFD solutions.

CHAPTER 9

CONCLUSIONS

9.1 Influences of surrounding buildings on wind loads of the target structure

This research aims to identify the influence of surrounding buildings areas in the formation and development of wind pressure on the primary structure. Based on CFD analysis results for cases without and with SBs, it can be concluded that the wind load analysis without the appearance of the SBs area is inappropriate. The results indicate that lack of SBs in the CFD simulation brings the differences in the wind flow properties, which was derived by the CFD simulation with SBs or WTT, and finally and resulting in an inaccurate pressure formation on the primary building.

In this study, on the target building's windward surface, there were 21 out of 129 locations having mean C_p from isolated case different from SBs case by no more than 20%. Additionally, the isolated case overestimates mean C_p compared to the SBs case with the average ratio of mean C_p from isolated and SBs cases on the windward surface about 1.8. Besides, up to 50.1% of locations on the windward surface in the isolated case have the mean C_p greater than two times of the mean C_p from the SBs case.

Based on these conclusions, practitioners should consider including the detail of the neighboring area's topography in wind flow simulation of the interesting structure. This necessary task helps avoid underestimating or overestimating wind loads on a building without the wind environment consideration.

This research clearly illustrates the importance of SBs in wind load analysis. However, it also raises a question of the neighboring area's size that researchers need to include in the simulation to optimize the accuracy and computational cost. The larger SBs are considered, the higher number of cells in the mesh, which increases the computational resource. For this study's limitation, our SBs' size is similar to the WTT, but further investigation is highly recommended.

9.2 Accuracy of CFD

This study purposed to attest to the accuracy and reliability of CFD in the wind load analysis. Based on comparisons between CFD simulation and the WTT about wind velocity in the air domain and the C_p distribution on the primary building, it can be concluded that CFD was successful in the recreate the wind flow and perform the wind pressure on the primary structure with a slight difference. The results specify that two-approach simulations considered in this study (LES & $k-\omega-SST$ TB) are almost identical in time-averaged solutions.

In this study, the comparison between LES and SST cases showed that 65% of tracking locations on the windward surface have similar mean C_p where difference between two method is no more than 30%. Furthermore, the comparison of mean C_p to those from the WTT on the windward surface indicated that LES is more accurate than SST as it predicts mean Cp with less than 30% error for 58% of all tracking locations, while it is 41% for SST simulation.

This study provided one more validation case of CFD simulation on a specific building. However, CFD's accuracy needs to be further studied to prove its accuracy with other structures in various heights and shapes. Additionally, for an accurate CFD simulation, the geometries measurement needs to be carefully measured.

9.3 CFD computation time

For a detailed observation of CFD in wind load analysis, this research included the simulation time of different approaches in CFD simulations, then recommending an efficient method in use. By conducting the CFD simulations with the same computer configuration, grid resolution, and setting conditions, it can be concluded that the LES approach was taking a massive computational time compared to the $k-\omega-SST$ TB (RANS) approach. In this study, with our computer configuration, LES

took over 15 times in solving time compared to $k-\omega-SST$ TB simulation. Besides, LES need to have extensive memory storage to store their time-dependent solution.

The results also indicate that RANS is more affordable than the LES but cannot provide the transient flow's characteristics (time-dependent phenomena), while LES shows its advantages about time-dependent phenomena. So, the selection of sufficient CFD simulations approach will base on the analysis purpose, design stage, and budget investment.

Based on these conclusions, practitioners should define the purpose and design stage when simulating. The combination of RANS and LES is highly recommended to reduce the computational cost. The early stage of a building needs a change in shape design, which RANS could bring the strengths of time and cost. When the architect design comes over, LES could be used to perform an accurate for structure design.

9.4 Connection to building codes and the role of CFD

Finding the role of CFD in wind load analysis, this research took a review of wind load analysis in ASCE 7 (USA) and DPT Standard 1311-50 (Thailand). The results show that the wind load formulas in code/standard are limited when analyzing the wind load for irregular-shaped buildings, buildings located in critical wind load scenarios, or high dynamic response. These cases' wind loads need to investigate by expensive wind tunnel tests. This study also illustrated that the use of CFD had not been mentioned in any codes/standards until the present time, although the wind profile is mainly based on its provision.

With high accuracy, CFD simulations can perfectly fulfill the shortage of building codes/standards about the wind load analysis for irregular-shaped building/structure. Based on the advantage of data visualization, until this moment, CFD tools have used in:

- The CFD simulations support building design

- CFD simulation helps to investigate the wind environment

- Application of CFD in the wind tunnel test process

- CFD simulations in investigating the pedestrian comfort

However, the role of CFD in dynamic response is limited in the research's scope. To better understand the building dynamic, future studies could address the Fluid-Structure Interaction (FSI).

APPENDIX A

ANSYS FLUENT VALIDATION CASES

A.1 Drag coefficient of a 45° angled square (2D)

The drag coefficient is a dimensionless quantity and known for qualifying the resistance or drag of an object in the fluid environment, such as water or air. This quantity relates to the shape (geometry), inclination, and flow characteristics. The *drag coefficient* (denoted by C_d) is rearranged from the drag equation as

$$C_d = \frac{F_D}{\frac{1}{2}\rho V^2 A} \tag{A-1}$$

where ρ is the fluid density, A is the reference are (the projected area on the plane being normal to the flow direction), V is the fluid velocity, and F_D is the drag force.

Notice that, one half the density multiplies the velocity squared is often called the *dynamic pressure* (q). In other words, the drag coefficient is the proportion of drag forces (F_D) and the product of dynamic pressure (q) and reference area (A).

$$C_d = \frac{F_D}{qA} \tag{A-2}$$

In the controlled environment like in Wind Tunnel, we can set for the *density*, *velocity* and determined the *affected area* as well as measuring the *drag forces* by sensors to calculate the drag coefficient. In many textbooks, the *drag coefficient* was measured by experiments (such as wind tunnel test) and published for different shapes of both two- and three-dimensions space (Figure A-1).

Figure 32 (near). Drag coefficients of various 3-dimensional bodies (40) at R'numbers between 10^4 and 10^6. Note: (•) tested on wind-tunnel floor.

Figure 33 (right). Drag coefficients (41) of 2-dimensional shapes (between walls) at R between 10^4 and 10^6. Note: (+) in subcritical flow.

¶ (37) Information on <u>rear-side pressure of plates</u>:
a) On disks and small-aspect-ratio plates see: NACA (36, a); AVA Ergebnisse IV; reference (40,f).
b) On plates between walls see: (12), (35,a) and (40,f).
¶ (40) Experimental results on <u>three-dimensional bodies</u>:
a) Doetsch, Parachute Models, Lufo 1938 p.577.
b) NACA, Cup Anemometer, Tech Rpt 513 (1935).
c) AVA, Hemispherical Bodies, Ergebnisse IV (1932).
d) Eiffel, Recherches a Tour Eiffel, Paris 1907.
e) Hemispherical Cup at $R_d = 2 \cdot 10^5$, ARC RM 712 (1919).
f) Irminger and Nokkentved, Elementary Bodies and Buildings, Kopenhagen 1930 and 1936; Transl'n by Jarvis.
¶ (41) Sections (tested <u>between plates or walls</u>):
a) Lindsey, Simple Shapes, NACA T. Rpt 619 (1940).
b) Junkers Wind-Tunnel, Report Ströte V.9609 (1940).
c) Interference Between Struts, NACA T. Rpt 468 (1933).
d) Delany-Sorensen, Various Shapes, NACA T.Note 3038.
e) AVA Göttingen, Ergebnisse II (1923) and III (1926).
f) Junkers Wind-Tunnel Result on Angle Profile.
g) Reported by Barth, Zt.Flugwissen 1954 p.309.
¶ (42) <u>Free-streamline</u> (cavitation) theory:
a) Kirchhoff, Free Jet Theory, Crelle 1869 (see Lamb).
b) Bobyleff, Russian Phys.-Chem. Society 1881 (see Lamb).
c) Riabouchinsky-Plesset-Schafer, Journal Appl.Physics 1948 p.934, and Review Modern Physics 1948 p.228.
d) Reichardt, Laws of Cavities, German ZWB UM 6628.
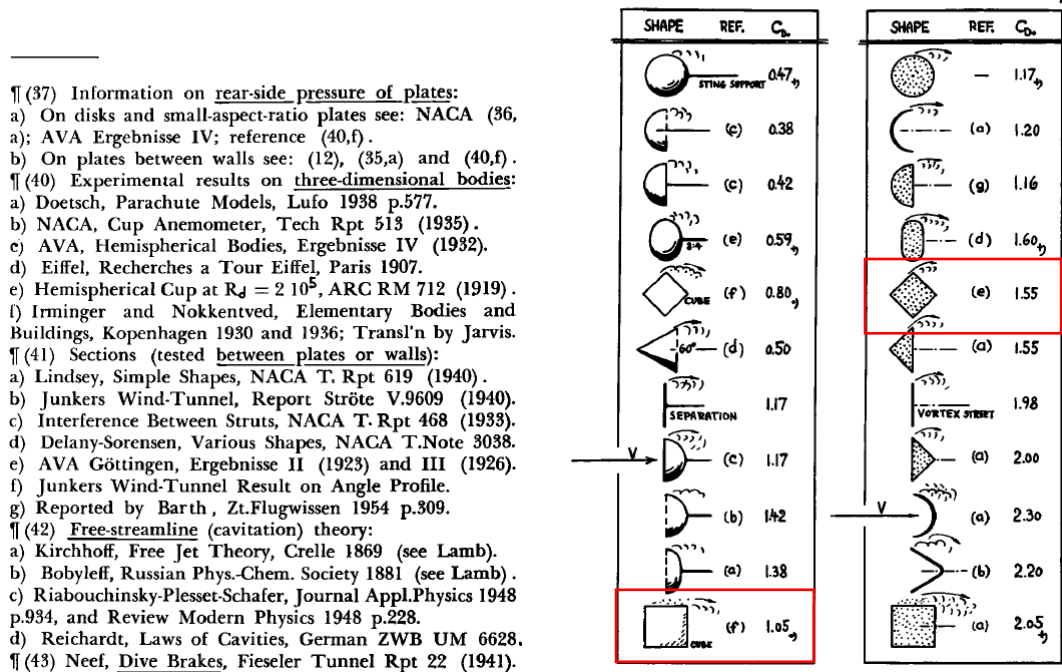¶ (43) Neef, <u>Dive Brakes</u>, Fieseler Tunnel Rpt 22 (1941).

Figure A-1 Drag coefficient of for different shapes (Hoerner, 1951)

In this study, we re-do a 2D case "wind flows over a 45° angled square" by ANSYS Fluent to verify the drag coefficient with the experiment. With the problem description in Figure A-2, the Reynold number is

$$\text{Re} = \frac{\rho V L}{\mu} = 8.13 \times 10^{-5}$$

(A-3)

where $L = 3\sqrt{2}\,m$ is the length scale equaling to the diagonal length of the square. In this case, the Reynold number is between 10^{-6} and 10^{-4}, which hopefully produces the coefficient around **1.55**
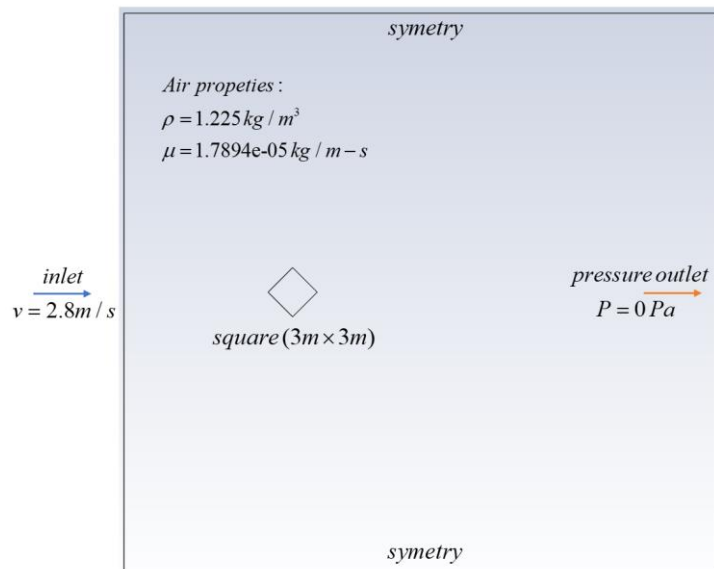
Figure A-2 Wind flows over a 45° angled square problem description

The 2D computational domain contains a velocity inlet with constant velocity $V = 2.8 m/s$, the pressure outlet with zero gauss pressure (to balance the pressure in and out of domain), two boundaries as symmetry, and square's sides treated as walls. The air in the domain is considered as incompressible flow by constant air density and viscosity. The high resolution hexahedral 2D mesh will apply to divide the whole domain into 64061 cells. Additionally, the near square-side is refined by prism layers to capture the sensitive characteristics here.
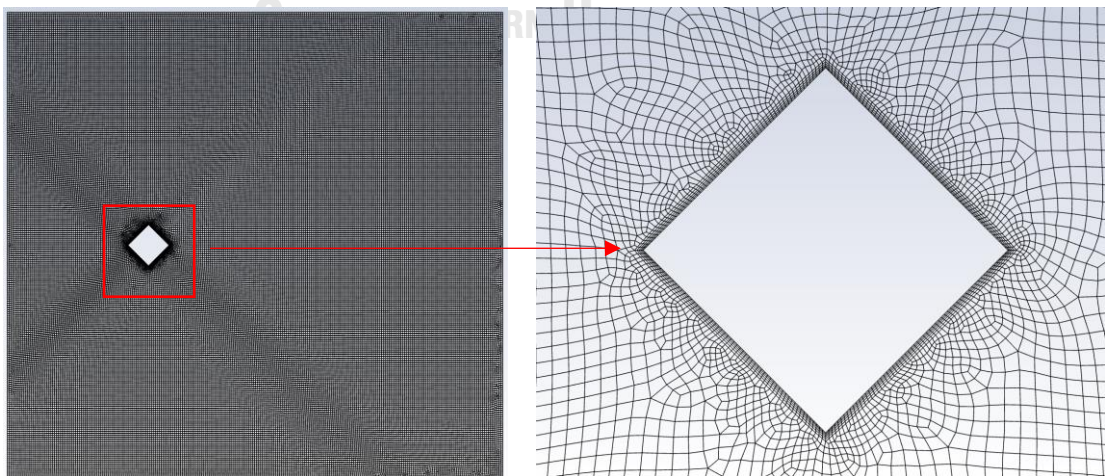
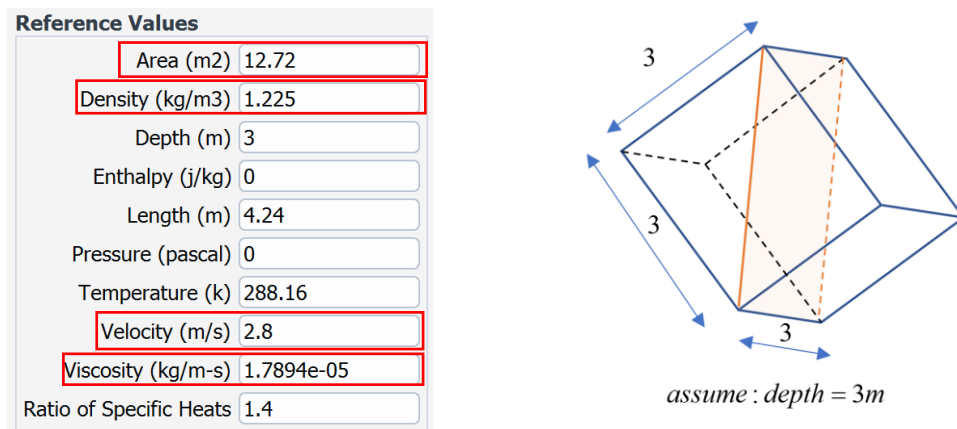

Figure A-3 2D mesh contains 64061 cells

Figure A-4 Reference values in ANSYS Fluent

In ANSYS Fluent, the drag coefficient is calculated in the same way with the equation (A-1). The CFD code would discretize the Naiver-Stokes equations and solves them over the computational air domain with the aid of the boundary conditions. In other words, ANSYS Fluent will calculate the drag force automatically. The rest components used in equation (A-1) need to be inputted in ANSYS Fluent called reference values (Figure A-4). Notice that the reference area comes from the assumption of square depth (equals 3m). So, the reference area (light orange area) is the product of diagonal length and depth ($A = 3\sqrt{2} \times 3 = 12.72 m^2$).

The turbulent model in use is **Spalart–Allmaras,** discussed in 2.3.1. All the variable residuals are set at **10^{-6}**. The solution method used default as the recommendation of ANSYS, which are **Coupled Scheme** with **second-order (upwind)** accuracy level for *pressure* and *momentum,* **Least Squares Cell-Based** for *gradient,* and the last, **first-order upwind** for *Modified turbulent viscosity.*

The result of CFD

After 1400 iterations solving, the solution converged with an unchanging drag coefficient (the monitor plot was unchangeable significantly). The result of the drag coefficient was **1.55015** and got an excellent agreement with the experiment value in the textbook (Figure A-1).
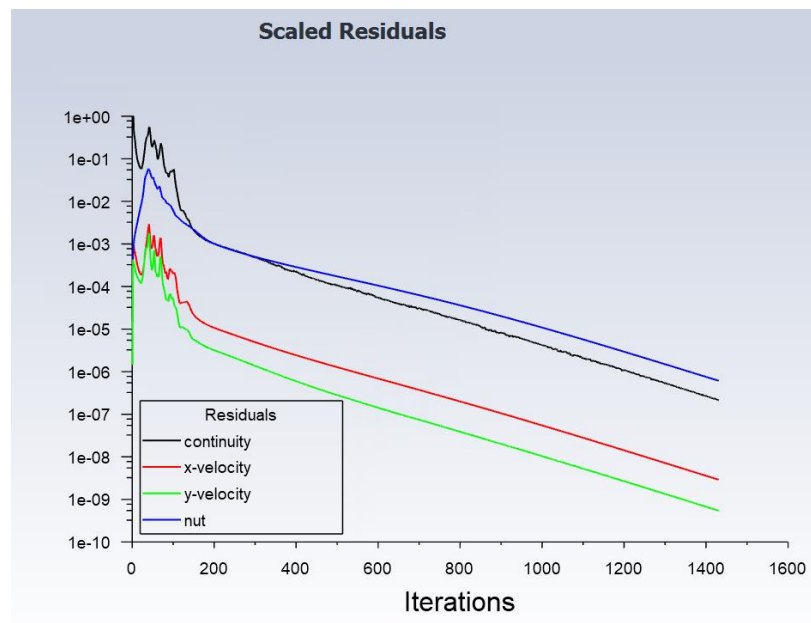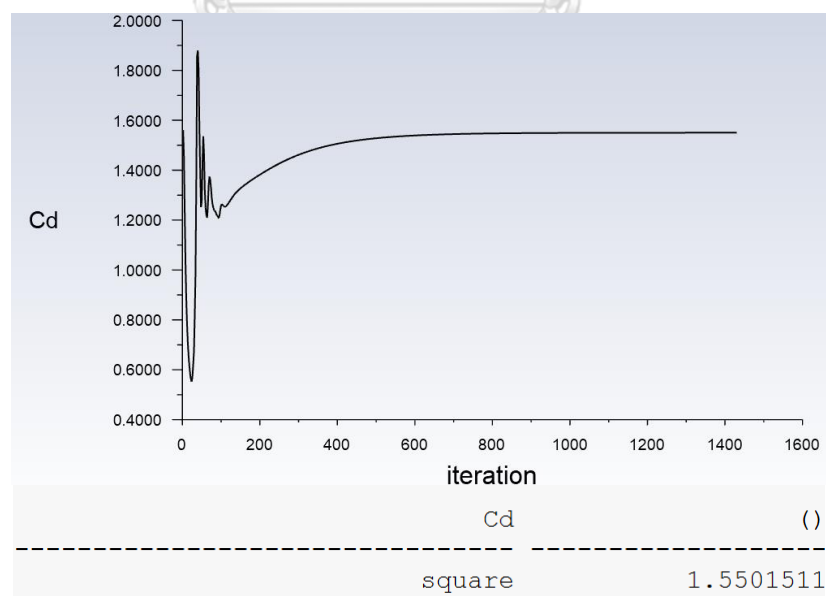

Figure A-5 Residuals plot

Figure A-6 Drag coefficient plot in ANSYS Fluent

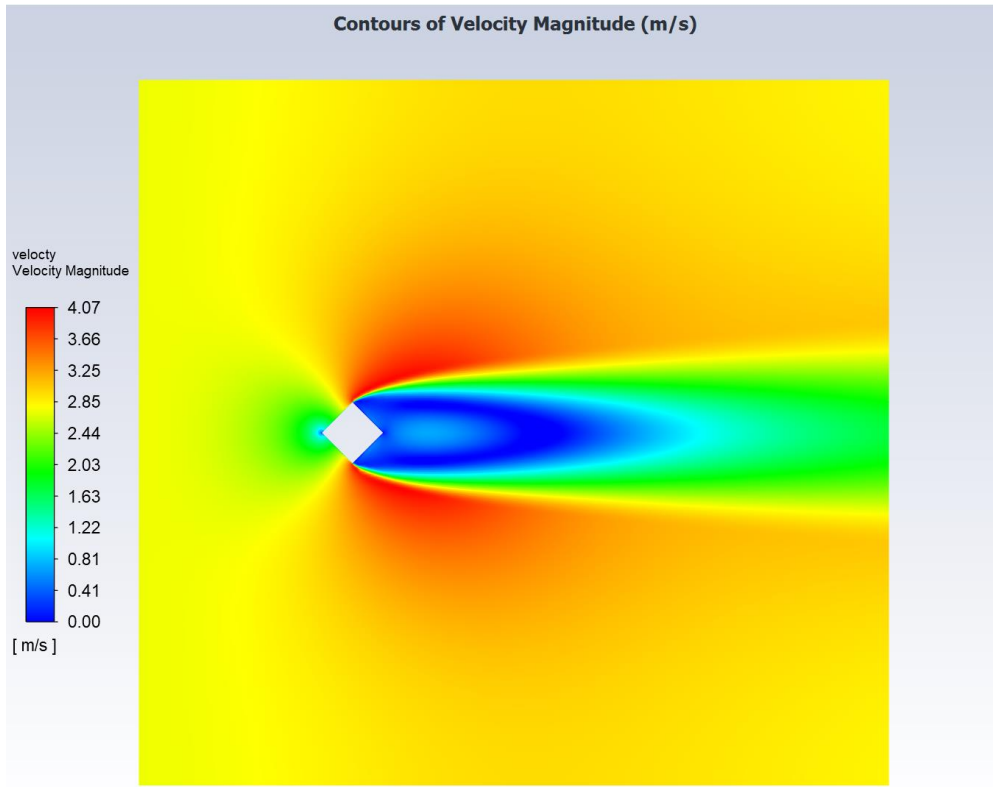Here are some details about the flow characteristic.
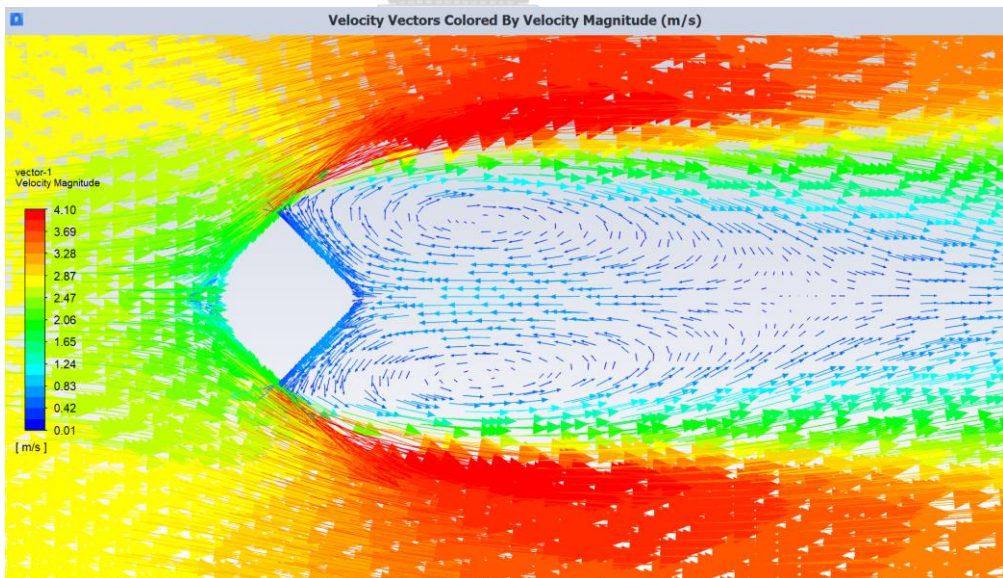
Figure A-7 Velocity contour

Figure A-8 Velocity vector

A.2 Drag coefficient of a cube (3D)

In this example, we used the same flow condition and simulation property, in example 0, and applied on the 3D air domain with a cube inside. The 2x2x2 (m^3) cube was floating in a 50x50x64 (m^3) computational domain. The distance from cube to inlet and four symmetry surfaces is 25m, while it is 40m to outlet. The mesh has 1673508 cells shown in Figure A-10.
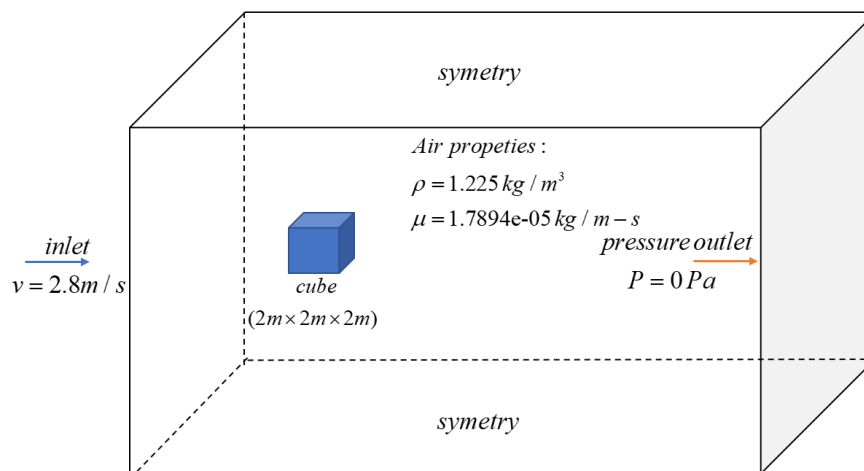

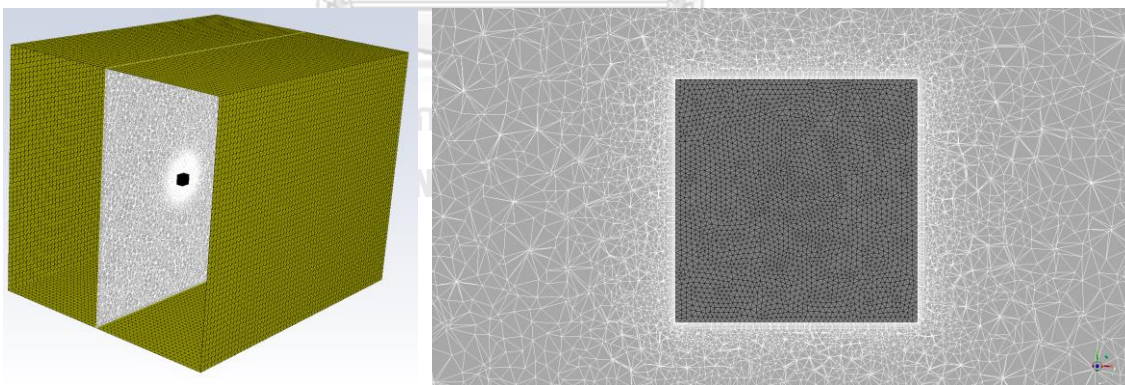Figure A-9 Wind flows over a cube (3D) description

Figure A-10 Mesh

The result of CFD

The solution took a convergence after around 500 iterations. This was proved by the constant of the cube's drag coefficient plot. All the residuals were getting a drop,

accept the continuity residual. The continuity error could not go down more and performed a periodic trend, which is a sign of convergence.
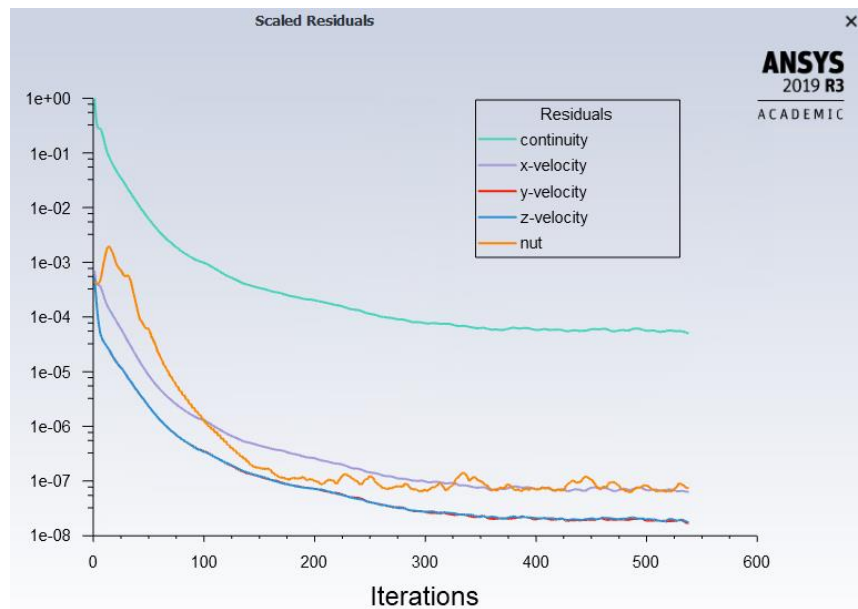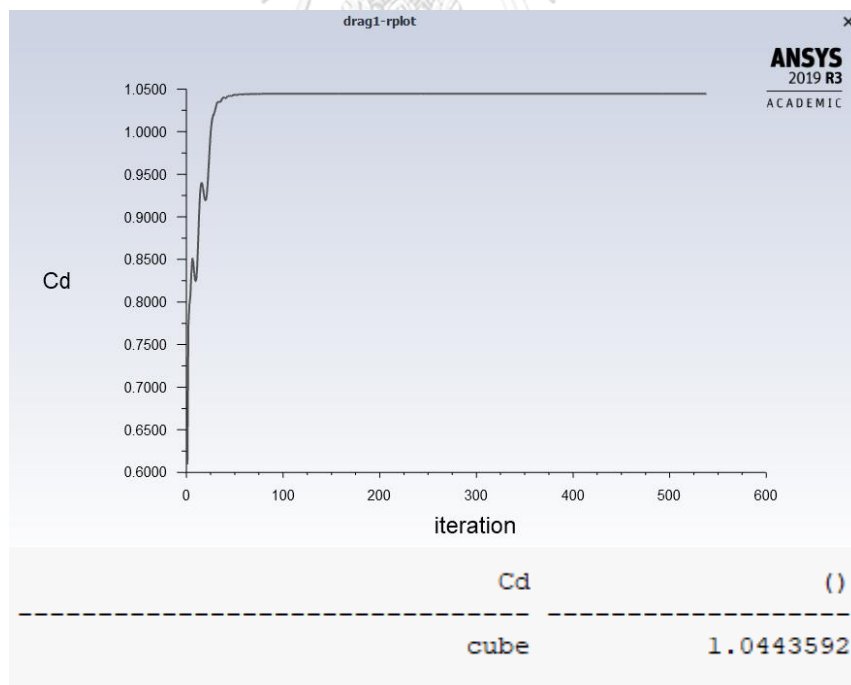

Figure A-11 Residuals plot

Figure A-12 Drag coefficient plot in ANSYS Fluent

The simulation brought a drag coefficient at **1.0444**, which takes incredibly close with the textbook's value (**1.05**) in Figure A-1. Here are some details about the flow characteristic.
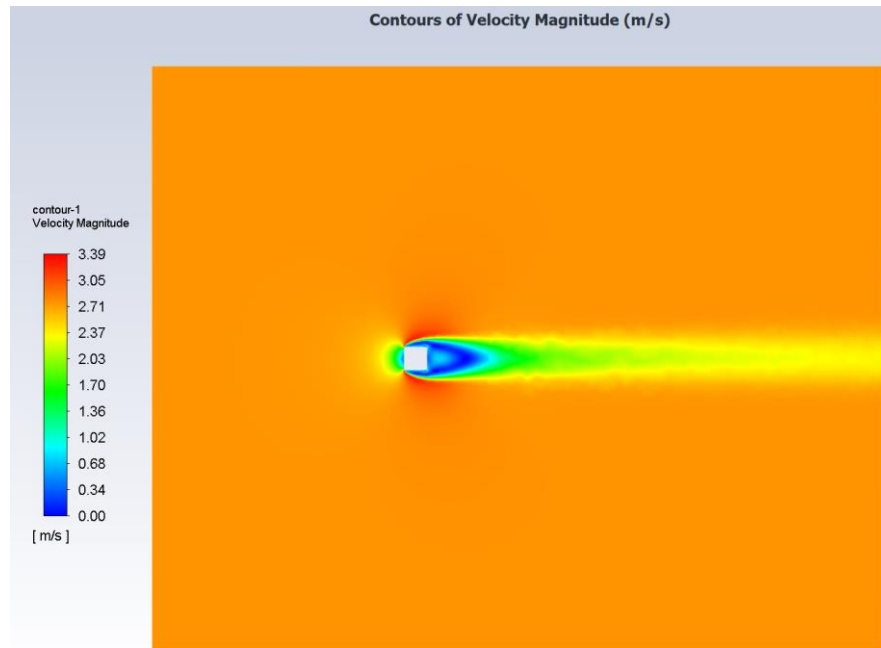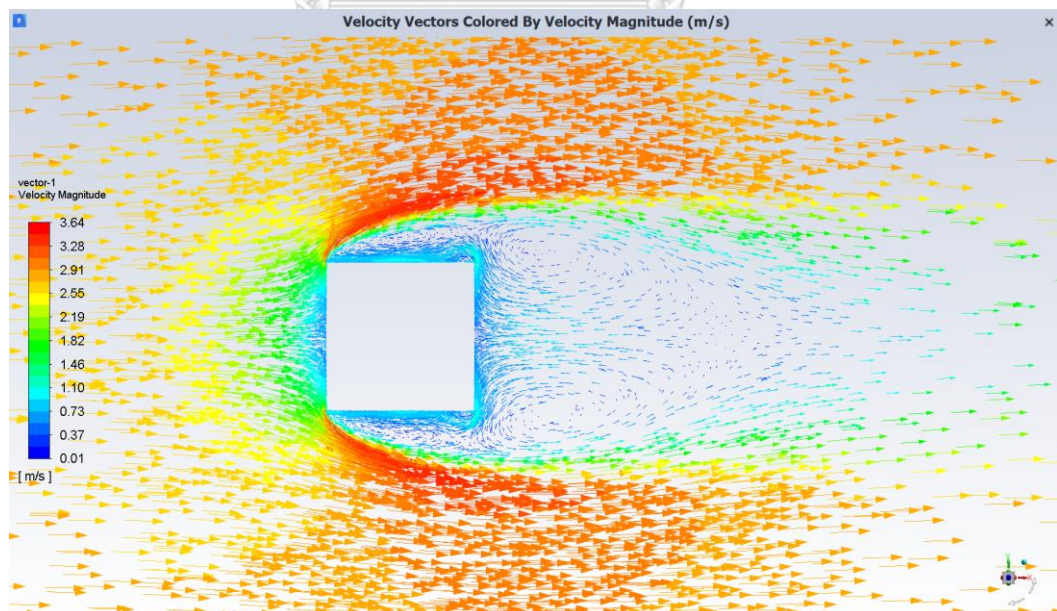

Figure A-13 Velocity contour

Figure A-14 Velocity vector

REFERENCES

AIJ. (2017). Guidebook of Recommendations for Wind Loads on Buildings 2 - Wind-Induced Response and Load Estimation/Practical Guide of CFD for Wind Resistant Design (In Japanese). Architectural Institute of Japan, Tokyo, Japan (2017).

American Society of Civil Engineers. (2017). Minimum design loads and associated criteria for buildings and other structures : ASCE/SEI 7-16. In *ASCE standard*. Reston, Virginia: Published by American Society of Civil Engineers.

Anderson, J. D., and Wendt, J. (1995). *Computational fluid dynamics* (Vol. 206): Springer.

ANSYS. (2016). ANSYS FLUENT 17 User's Guide.

ASCE. (1999). Wind Tunnel Studies of Buildings and Structures. *ASCE MANUAL OF PRACTICE NO. 67*.

ASCE. (2005). *Minimum Design Loads for Buildings and Other Structures (7-05)*.

Asghari Mooneghi, M., and Kargarmoakhar, R. (2016). Aerodynamic Mitigation and Shape Optimization of Buildings: Review. *Journal of Building Engineering, 6*, 225-235. doi:https://doi.org/10.1016/j.jobe.2016.01.009

Beranek, W. (1980). General rules for the determination of wind environment. In *Wind Engineering* (pp. 225-234): Elsevier.

Blocken, B., Carmeliet, J. J. J. o. w. e., and aerodynamics, i. (2004). A review of wind-driven rain research in building science. *92*(13), 1079-1130.

Boonyapinyo, V., Magteppong, N., Bhadrakom, N., and Wongkansirikul, P. (2016). Wind load study for a building project by wind tunnel test: Overall wind load and pressure measurement. Thammasat University, Pathumthani, Thailand.

Camarri, S., Salvetti, M. V., Koobus, B., and Dervieux, A. (2005). Hybrid RANS/LES simulations of a bluff-body flow. *Wind and Structures, 8*(6), 407-426.

Coulbourne, W. L., and Stafford, T. E. (2020). *Wind Loads: Guide to the Wind Load Provisions of Asce 7-16*: American Society of Civil Engineers.

Dacles-Mariani, J., Zilliac, G. G., Chow, J. S., and Bradshaw, P. (1995). Numerical/experimental study of a wingtip vortex in the near field. *AIAA journal, 33*(9), 1561-1568.

Daemei, A. B. (2019). Wind Tunnel Simulation on the Pedestrian Level and Investigation of Flow Characteristics Around Buildings. *J. Energy Manag. Technol., 3*(1), 58-68.

Dagnew, A. K., Bitsuamalk, G. T., and Merrick, R. (2009). *Computational evaluation of wind pressures on tall buildings.* Paper presented at the 11th American conference on Wind Engineering. San Juan, Puerto Rico.

Dagnew, A. K., and Bitsuamlak, G. T. (2013). Computational evaluation of wind loads on buildings: a review. *Wind Struct, 16*(6), 629-660.

Department of Public Works and Town & Country Planning. (2007). Wind Loading Calculation and Response of Buildings: DPT 1311-50. In. Published by Department of Public Works and Town & Country Planning.

DPT. (2007). DPT 1311-50: Wind Loading Calculation and Response of Buildings. *Department of Public Works and Town & Country Planning*.

El-Okda, Y., Ragab, S., and Hajj, M. (2008). Large-eddy simulation of flow over a surface-mounted prism using a high-order finite-difference scheme. *Journal of Wind Engineering and Industrial Aerodynamics, 96*(6-7), 900-912.

Engineering Institute of Thailand. (2003). Wind Loading Code for Building Design: E.I.T. Standard 1018-46. In: Published by Engineering Institute of Thailand.

Fluent, A. (2013). ANSYS fluent theory guide 15.0. *ANSYS, Canonsburg, PA*.

Franke, J., Hellsten, A., Schlunzen, K. H., and Carissimo, B. (2011). The COST 732 Best Practice Guideline for CFD simulation of flows in the urban environment: a summary. *International Journal of Environment and Pollution, 44*(1-4), 419-427.

Franke, J., Hirsch, C., Jensen, A., Krüs, H., Schatzmann, M., Westbury, P., . . . Wright, N. (2004). *Recommendations on the use of CFD in wind engineering.* Paper presented at the Cost action C.

Hoerner, S. F. (1951). *Aerodynamic Drag: Practical Data on Aerodynamic Drag Evaluated and Presented*: Otterbein Press.

Launder, B. E., and Spalding, D. B. (1972). *Mathematical models of turbulence*: Academic press.

Luo, Y., Liu, H., Xue, H., and Lin, K. (2019). Large-eddy simulation evaluation of wind loads on a high-rise building based on the multiscale synthetic eddy method. *Advances in Structural Engineering, 22*(4), 997-1006. doi:10.1177/1369433218794258

Menter, F. R. (1994). Two-equation eddy-viscosity turbulence models for engineering applications. *AIAA journal, 32*(8), 1598-1605.

Murakami, S. (1990). Computational wind engineering. *Journal of Wind Engineering and Industrial Aerodynamics, 36*, 517-538.

Murakami, S. (1998). Overview of turbulence models applied in CWE-1997. *Journal of Wind Engineering and Industrial Aerodynamics, 74-76*, 1-24. doi:10.1016/S0167-6105(98)00004-X

Murakami, S., and Mochida, A. (1988). 3-D numerical simulation of airflow around a cubic model by means of the k-ϵ model. *Journal of Wind Engineering and Industrial Aerodynamics, 31*(2-3), 283-303.

Murakami, S., Ooka, R., Mochida, A., Yoshida, S., and Sangjin, K. (1999). CFD analysis of wind climate from human scale to urban scale. *Journal of Wind Engineering and Industrial Aerodynamics, 81*(1), 57-81.

National Research Council of Canada. Canadian Commission on, B., and Fire, C. (1995). National Building Code of Canada: 1995. In *National Building Code of Canada; no. Eleventh edition* (Fourth printing. Includes the revisions and errata published in July 1998, November 1999, June 2001, April 2002 and June 2003 ed.): National Research Council of Canada.

Orszag, S. A. (1993). Renormalisation group modelling and turbulence simulations. *Near-wall turbulent flows*.

Porté-Agel, F., Meneveau, C., and Parlange, M. B. (2000). A scale-dependent dynamic model for large-eddy simulation: application to a neutral atmospheric boundary layer. *Journal of Fluid Mechanics, 415*, 261-284.

Sayma, A. (2009). *Computational fluid dynamics*: Bookboon.

Selvam, R. P. (1997). Computation of pressures on Texas Tech University building using large eddy simulation. *Journal of Wind Engineering and Industrial Aerodynamics, 67*, 647-657.

Shih, T.-H., Liou, W. W., Shabbir, A., Yang, Z., and Zhu, J. (1995). A new k-ϵ eddy viscosity model for high reynolds number turbulent flows. *Computers & Fluids, 24*(3), 227-238.

Smagorinsky, J. (1963). General circulation experiments with the primitive equations: I. The basic experiment. *Monthly weather review, 91*(3), 99-164.

Spalart, P., and Allmaras, S. (1992). *A one-equation turbulence model for aerodynamic flows.* Paper presented at the 30th aerospace sciences meeting and exhibit.

Tamura, T. (2006). Towards practical use of LES in wind engineering. *Journal of Japan Wind Engineering*(108), 1-8.

Tamura, T., Nozawa, K., and Kondo, K. (2008). AIJ guide for numerical prediction of wind loads on buildings. *Journal of Wind Engineering and Industrial Aerodynamics, 96*(10-11), 1974-1984.

Thordal, M. S., Bennetsen, J. C., and Koss, H. H. H. (2019). Review for practical application of CFD for the determination of wind load on high-rise buildings. *Journal of Wind Engineering and Industrial Aerodynamics, 186*, 155-168.

Tominaga, Y., Mochida, A., Murakami, S., and Sawaki, S. (2008). Comparison of various revised k–ϵ models and LES applied to flow around a high-rise building model with 1: 1: 2 shape placed within the surface boundary layer. *Journal of Wind Engineering and Industrial Aerodynamics, 96*(4), 389-411.

Versteeg, H. K., and Malalasekera, W. (2007). *An introduction to computational fluid dynamics: the finite volume method*: Pearson education.

Wilcox, D. C. (1998). *Turbulence modeling for CFD* (Vol. 2): DCW industries La Canada, CA.

Wright, N. G., and Easom, G. (2003). Non-linear k–ϵ turbulence model results for flow over a building at full-scale. *Applied Mathematical Modelling, 27*(12), 1013-1033.

VITA

NAME	PHUNG THIET CANH
DATE OF BIRTH	29 August 1995
PLACE OF BIRTH	Binh Dinh province, Viet Nam
INSTITUTIONS ATTENDED	Ho Chi Minh City University of Technology (HCMUT)
	Chulalongkorn University (CU)
HOME ADDRESS	Ho Chi Minh City, Viet Nam